Universitat
de les Illes Balears

DOCTORAL THESIS
2022

ELECTRONIC AND TOPOLOGICAL PROPERTIES OF BILAYER GRAPHENE NANOSTRUCTURES

Nassima Benchtaber

Universitat
de les Illes Balears

DOCTORAL THESIS
2022

Doctoral Programme in Physics

ELECTRONIC AND TOPOLOGICAL PROPERTIES OF BILAYER GRAPHENE NANOSTRUCTURES

Nassima Benchtaber

Thesis Supervisor: Llorenç Serra Crespí
Thesis Supervisor: David Sánchez Martín
Thesis tutor: María Rosa López Gonzalo

Doctor by the Universitat de les Illes Balears

List of Publications

1. Nassima Benchtaber, David Sánchez, Llorenç Serra. Scattering of topological kink-antikink states in bilayer graphene, Physical Review B, vol 104, 155303 (1-9) (2021).
2. Nassima Benchtaber, David Sánchez, Llorenç Serra. Geometry effects in topologically confined bilayer graphene loops, New Journal of Physics, vol 24, 013001 (1-11) (2021).
3. Nassima Benchtaber, David Sánchez, Llorenç Serra. Trivial and topological bound states in bilayer graphene quantum dots and rings, Physica Status Solidi B, vol 259, 2200023 (1-6) (2022) (Special issue back cover).

List of contributions to conferences and workshops

1. NanoSpain conference "NanoSpain 2022", from 17 to 20 May 2022, Madrid, Spain. Talk participation.
2. The 11th edition of Graphene Conference series, the largest European Event in Graphene and 2D Materials, "Graphene 2021", from 26 to 29 October 2021, Grenoble, France. Talk participation.
3. Lake Como school "Thermodynamics of quantum systems and processes", from 22-26 March 2021, Italy. Talk participation.
4. The 3rd International Conference of Computer Science and Renewable Energies (ICCSRE'2020), from 22 to 24 December 2020, Agadir, Morocco. Talk participation.
5. IFISC Talk, 18 December 2022, IFISC Institute, Palma, Spain. Talk participation.
6. IFISC poster Party 2022, from 21 to 25 March 2022, IFISC Institute, Palma de Mallorca Spain. Poster participation.
7. Topological Matter School 2021, organized by Donostia international centre Spain, held online, from 16 to 27 August 2021. Poster participation.
8. IFISC poster Party 2021, from 22 to 26 March 2021, IFISC Institute, Palma de Mallorca Spain. Poster participation.
9. IFISC poster Party 2020, 20 February 2020, IFISC Institute, Palma, Spain. Poster participation.
10. Topological Materials: From Weak to Strong Correlations Workshop, Online attendance, organized by the Max Planck Institute for the Physics of Complex Systems, from 11 to 13 April 2022, Dresde, Germany.

Abstract

This thesis is devoted to studying the electronic properties of bilayer graphene (BLG) by focusing on the confined states, especially the topological states and the study of the transport in this material, addressing charge transport for electrons with and without magnetic field.

Electrostatic confinement in BLG is achieved by applying top and bottom micro-electrodes acting with reversed signs on the two graphene sheets. We discuss in this thesis two types of electrostatic confinement: trivial and topological.

Trivial electrostatic confinement in BLG is characterized by all micro-electrodes on the top side having the same potential sign, which is opposed to the sign of all micro-electrodes on the bottom side of the graphene sheets.

Topological electrostatic confinement in BLG is characterized by different micro-electrodes of the top side having sign inversion of the potential. This creates boundaries separating regions of opposite directions of the inter-layer electric field. The boundary with a straight line shape is known as a kink, and the low energy electronic states propagate along the kink.

Chapter 1 is a general introduction, discussing the fundamental aspects and theoretical background of monolayer and bilayer graphene, quantum transport, and its paradigmatic systems (quantum dots and quantum points contacts). In Chapter 2, we discuss the trivial and topological confinement in bilayer graphene wires, comparing the two types of confinement depending on the potential applied to the bilayer graphene sheets. We discuss the behavior of the confined states in both cases. We found that for the trivial confinement the spectrum opens a gap, and the states are confined in a region with a low energy gap. Otherwise, in the topological confinement, in the middle of the gap, we found states propagating in opposite directions for each valley. This phenomenon is known as momentum-valley locking in bilayer graphene.

To investigate and know more about these states and their behavior, Chapter 3 describes a system where we can study and control the back-scattering of those topological states under kink-antikink potentials. We demonstrate that a kink-antikink constriction can modulate the transmission electrostatically.

If we change the geometry of bilayer graphene what will happen to the topological states? The fourth Chapter answers this question when discussing the geometry dependence on the bilayer graphene. We take four shapes from higher to lower symmetry (circle, square, rectangle, and polygon). Our study shows that for small sizes the spectrum depends on the loop shape. Magnetic field induces a valley splitting and asymmetry in the spectrum.

We have also done a comparative study between the trivial and topological confinement in the case of circular geometry (ring and dot), as discussed in Chapter 5. The study discusses the trivial confinement where it shows bunching of levels into degenerate Landau bands, with an energy asymmetric gap, while topological confinement shows no field-

induced gap and a sequence of state branches always crossing zero energy.

Finally, a summary of our results is included in Chapter 6. In this Chapter we also give a perspective and future works that would either treat systems not considered in this work or extend the applicability range of our theoretical formalism.

Resumen

Esta tesis está dedicada al estudio de las propiedades electrónicas del grafeno bicapa (BLG) centrándose en los estados confinados, especialmente en los estados topológicos y en el estudio del transporte en este material, abordando el transporte de carga electrónica con y sin campo magnético.

El confinamiento electrostático en el BLG se consigue aplicando microelectrodos superiores e inferiores que actúan con signos invertidos en las regiones opuestas de las dos hojas de grafeno. En esta tesis discutimos dos tipos de confinamiento electrostático: trivial y topológico.

El confinamiento electrostático trivial en el BLG se caracteriza porque todos los microelectrodos de una determinada cara superior tienen el mismo signo de potencial, que es opuesto al signo de todos los microelectrodos de la cara inferior de las hojas de grafeno.

El confinamiento electrostático topológico en el BLG se caracteriza por que diferentes microelectrodos de una determinada cara superior tienen la inversión del signo del potencial. Esto crea fronteras que separan regiones de direcciones opuestas del campo eléctrico entre capas. La frontera con forma de línea recta se conoce como kink, y los estados electrónicos de baja energía se propagan a lo largo del kink.

El capítulo 1 es una introducción general, en la que se discuten los aspectos fundamentales y los antecedentes teóricos del grafeno monocapa y bicapa, el transporte cuántico y sus sistemas paradigmáticos (puntos cuánticos y contactos de puntos cuánticos). En el capítulo 2, discutimos el confinamiento trivial y topológico en hilos de grafeno bicapa, comparando los dos tipos en función del potencial aplicado a las hojas de grafeno bicapa. Discutimos el comportamiento de los estados confinados en ambos casos. Encontramos que para el confinamiento trivial el espectro abre una brecha, y los estados quedan confinados en una región con una baja brecha energética. En cambio, en el confinamiento topológico, en medio de la brecha, encontramos estados que se propagan en direcciones opuestas para cada valle. Este fenómeno se conoce como bloqueo valle-momento en el grafeno bicapa.

Para investigar y conocer mejor estos estados y su comportamiento, el capítulo 3 describe un sistema en el que podemos estudiar y controlar la retrodispersión de estos estados topológicos bajo potenciales kink-antikink. Demostramos que una constricción kink-antikink puede modular la transmisión electrostática.

Si cambiamos la geometría del grafeno bicapa, ¿qué ocurrirá con los estados topológicos? El cuarto capítulo responde a esta pregunta al analizar la dependencia de la geometría del grafeno bicapa. Tomamos cuatro formas de mayor a menor simetría (círculo, cuadrado, rectángulo y polígono). Nuestro estudio muestra que para tamaños pequeños el espectro depende de la forma del bucle. El campo magnético induce un desdoblamiento del valle y una asimetría en el espectro.

También hemos realizado un estudio comparativo entre el confinamiento trivial y el

topológico en el caso de la geometría del círculo (anillo y punto), como se discute en el capítulo 5. El estudio discute el confinamiento trivial donde se muestra el agrupamiento de los niveles en bandas de Landau degeneradas, con un gap energético asimétrico, mientras que el confinamiento topológico no muestra ningún gap inducido por el campo y una secuencia de ramas de estado que siempre cruzan la energía cero.

Finalmente, un resumen de nuestros resultados se incluye en el Capítulo 6. En este capítulo damos además una perspectiva y trabajos futuros que tratarían sistemas no considerados en este trabajo o ampliarían el rango de aplicabilidad de nuestro formalismo teórico.

Resum

Aquesta tesi està dedicada a l'estudi de les propietats electròniques del grafè bicapa (BLG) centrant-se en els estats confinats, especialment en els estats topològics i en l'estudi del transport en aquest material, abordant el transport de càrrega Electrónica amb camp magnètic i sense.

El confinament electrostàtic al BLG s'aconsegueix aplicant microelèctrodes superiors i inferiors que actuen amb signes invertits a les regions oposades de les dues fulles de grafè. En aquesta tesi discutim dos tipus de confinament electrostàtic: trivial i topològic.

El confinament electrostàtic trivial al BLG es caracteritza perquè tots els microelèctrodes d'una determinada cara (superior) tenen el mateix signe de potencial, que és oposat al signe de tots els microelèctrodes de la cara inferior de les fulles de grafè.

El confinament electrostàtic topològic al BLG es caracteritza perquè diferents microelèctrodes d'una determinada cara superior tenen la inversió del signe del potencial. Això crea fronteres que separen regions de direcció oposades del camp elèctric entre capes. La frontera amb forma de línia recta es coneix com a kink, i els estats electrònics de baixa energia es propaguen al llarg del kink.

El capítol 1 és una introducció general, en què es discuteixen els aspectes fonamentals i els antecedents teòrics del grafè monocapa i bicapa, el transport quàntic i els seus sistemes paradigmàtics (punts quàntics i contactes de punts quàntics). Al capítol 2, discutim el confinament trivial i topològic en fils de grafè bicapa, comparant els dos tipus en funció del potencial aplicat a les fulles de grafè bicapa. Discutim el comportament dels estats confinats en tots dos casos. Trobem que per al confinament trivial l'espectre obre una bretxa, i els estats queden confinats a una regió amb una baixa bretxa energètica. En canvi, al confinament topològic, enmig de la bretxa, trobem estats que es propaguen en direccions oposades per a cada vall. Aquest fenomen es coneix com a bloqueig momentum-valley al grafè bicapa.

Per investigar i conèixer millor aquests estats i el seu comportament, el capítol 3 descriu un sistema on podem estudiar i controlar la retrodispersió d'aquests estats topològics sota potencials kink-antikink. Demostrem que una constricció kink-antikink pot modular la transmissió electrostàtica.

Si canviem la geometria del grafè bicapa, què passarà amb els estats topològics? El quart capítol respon aquesta pregunta en analitzar la dependència de la geometria del grafè bicapa. Prenem quatre formes de major a menor simetria (cercle, quadrat, rectangle i polígon). El nostre estudi mostra que per a petites mides l'espectre depèn de la forma del bucle. El camp magnètic indueix un desdoblament de la vall i una asimetria a l'espectre.

També hem realitzat un estudi comparatiu entre el confinament trivial i el topològic en el cas de la geometria del cercle (anell i punt), com es discuteix al capítol 5. L'estudi discuteix el confinament trivial on es mostra l'agrupament dels nivells en bandes de Landau degenerades, amb un buit energètic asimètric, mentre que el confinament topològic no

mostra cap buit induït pel camp i una seqüència de branques d'estat que sempre creuen la energia zero.

Finalment, un resum dels nostres resultats s'inclou al Capítol 6. En aquest capítol donem també una perspectiva i feines futures que tractarien sistemes no considerats en aquest treball o ampliarien el rang d'aplicabilitat del nostre formalisme teòric.

Acknowledgments

This thesis work was carried out under the direction of my dear professors, Prof. Dr. David Sánchez and Prof. Dr. Llorenç Serra. I would like to sincerely thank my directors for accepting me into this thesis program, for the time they have devoted to me, for the permanent support and the confidence they have granted me as well as for their help, their precious advice, and explanations.

When I come the first time to the university I meet some trouble, my computer was not working well and the covid-19 situation also makes me feel stressed, you helped me a lot to adapt to the new environment in the university and with the method of work. When I feel blocked and slow with work, I found you both professors helping me and encouraging me, I appreciate that. Your important advice gives me a powerful impetus to do better.

I would like to thank also all members of the FISNANO group, my tutor Prof. Dr. Rosa Lopez and Dr. Sunggen Ryu. It was a pleasure to meet and know them. Additionally, I want to thank the research institute IFISC, the perfect environment of work where I spent the three years of my Ph.D. Many thanks also to all friendly members of the institute.

Finally, I'm so thankful to my husband Brahim for his love support, and encouragement even the distance and the covid situation where I could not see him for a while he always supports me and encourages me to develop my career and doing good work. I'm also thankful to my family my mother and my father for their love and support and encouragement.

Last but not least, I would like to acknowledge the financial support from MINECO (Spain) Grant No. MAT2017-82639, and the MINECO/AEI/FEDER Maria de Maeztu Program for Units of Excellence MDM2017-0711.

Agradecimientos

Este trabajo de tesis fue realizado bajo la dirección de mis queridos profesores, Prof. Dr. David Sánchez y el Prof. Dr. Llorenç Serra. Quisiera agradecer sinceramente a mis directores por aceptarme en este programa de tesis, por el tiempo que me han dedicado, por el apoyo permanente y la confianza que me han brindado, así como por su ayuda, sus valiosos consejos y explicaciones.

Cuando llego por primera vez a la universidad me encuentro con un problema, mi computadora no funcionaba bien y la situación del covid-19 también me estresa, me ayudasteis mucho a adaptarme al nuevo ambiente en la universidad y con el método de trabajo. Cuando me siento bloqueada y lenta con el trabajo, los encontré a ambos profesores ayudándome y animándome, lo agradezco. Su importante consejo me da un poderoso impulso para hacerlo mejor.

Me gustaría agradecer también a todos los miembros del grupo FISNANO, a mi tutora Prof. Dr. Rosa López y al Dr. Sunggen Ryu. Fue un placer conocerlos. Adicionalmente, quiero agradecer al instituto de investigación IFISC, el perfecto ambiente de trabajo donde pasé los tres años de mi Ph.D. Muchas gracias también a todos los miembros amigos del instituto.

Finalmente, estoy muy agradecida con mi esposo Brahim por su amor, apoyo y aliento, incluso en la distancia y la situación de covid en la que no pude verlo por un tiempo, siempre me apoya y me anima a desarrollar mi carrera y hacer un buen trabajo. También estoy agradecido con mi familia, mi madre y mi padre por su amor, apoyo y aliento.

Por último, pero no menos importante, me gustaría agradecer el apoyo financiero de MINECO (España) Beca No. MAT2017-82639, y el MINECO/AEI/FEDER Programa María de Maeztu para Unidades de Excelencia MDM2017-0711. .

Agraïments

Aquest treball de tesi s'ha realitzat sota la direcció dels meus estimats professors, el Prof. Dr. David Sánchez i Prof. Dr. Llorenç Serra. Vull agrair sincerament als meus directors per acceptar-me en aquest programa de tesi, pel temps que m'han dedicat, pel suport permanent i la confiança que m'han atorgat, així com per la seva ajuda, els seus valuosos consells i explicacions.

Quan arribo per primera vegada a la universitat em trobo amb algun problema, el meu ordinador no funcionava bé i la situació del covid-19 també em fa sentir estressada, em vareu ajudar molt a adaptar-me al nou entorn de la universitat i amb el mètode de treball. Quan em sento bloquejada i lenta amb la feina, vaig trobar que tots dos professors m'ajudeu i m'encoratjo, ho agraeixo. El vostre important consell em dóna un poderós impuls per fer-ho millor.

També m'agradaria donar les gràcies a tots els membres del grup FISNANO, a la meva tutora Prof. Dr. Rosa Lopez i al Dr. Sunggen Ryu. Va ser un plaer conèixer-los. A més, vull donar les gràcies a l'institut de recerca IFISC, l'entorn perfecte de treball on vaig passar els tres anys del meu doctorat. Moltes gràcies també a tots els amics de l'institut.

Finalment, estic molt agraïda al meu marit Brahim pel seu suport amorós, i ànims fins i tot en la distància i la situació de covid en què no el vaig poder veure durant un temps, sempre m'acompanya i m'anima a desenvolupar la meva carrera professional i a fer una bona feina. També estic agraïda a la meva família, la meva mare i el meu pare pel seu amor, suport i ànims.

Finalment, però no menys important, m'agradaria agrair el suport financer del MINECO (Espanya) Beca núm. MAT2017-82639, Programa MINECO/AEI/FEDER Maria de Maeztu per a Unitats d'Excel·lència MDM2017-0711.

Contents

List of publications and communications . . . iii
Abstract . . . v
Acknowledgments . . . xi

1 Introduction 1
- 1.1 Motivation . . . 1
- 1.2 Graphene . . . 5
  - 1.2.1 Monolayer graphene . . . 5
    - 1.2.1.1 Atomic properties . . . 5
    - 1.2.1.2 Electronic properties . . . 6
  - 1.2.2 Bilayer graphene . . . 9
  - 1.2.3 Magnetic field dependence . . . 12
- 1.3 Quantum Transport . . . 15
  - 1.3.1 Landauer-Büttiker model . . . 15
    - 1.3.1.1 Current for nonzero temperature and bias . . . 17
  - 1.3.2 Transport through a quantum dot . . . 18
  - 1.3.3 Quantum point contact . . . 21
  - 1.3.4 Transport in graphene . . . 22
    - 1.3.4.1 Chirality in graphene . . . 22
    - 1.3.4.2 Transmission coefficient and conductance . . . 23
- 1.4 Berry Phase in graphene . . . 25
- 1.5 Experimental overview . . . 27
  - 1.5.1 Monolayer graphene quantum dot . . . 27
  - 1.5.2 Bilayer graphene quantum dots . . . 28
  - 1.5.3 Experimental realization of a valleytronic device . . . 29
- 1.6 Conclusion . . . 32

2 Confinement in BLG wires 35
- 2.1 Trivial confinement . . . 35
  - 2.1.1 Effective Hamiltonian . . . 37
    - 2.1.1.1 Model . . . 37
  - 2.1.2 Band structure . . . 38
  - 2.1.3 Magnetic field dependence . . . 39
  - 2.1.4 Width effect on the energy spectrum . . . 40
- 2.2 Topological confinement . . . 41
  - 2.2.1 Single kink potential profile . . . 42

- 2.2.1.1 Single kink numerical results 49
- 2.2.1.2 Magnetic field dependence 50
- 2.2.2 Double kink potential profile 50
  - 2.2.2.1 Dependence of the kink separation of the energy spectrum 52
  - 2.2.2.2 Magnetic field dependence 52
- 2.3 Symmetries of the Hamiltonian 53
- 2.4 Conclusion 55

3 Scattering of topological kink-antikink states in bilayer graphene structures 57
- 3.1 Back-scattering-control proposal device 57
- 3.2 Model 60
- 3.3 Results 63
  - 3.3.1 Quantum point contacts 63
  - 3.3.2 Side loops 67
- 3.4 Discussion 72
  - 3.4.1 Kink-antikink gap 72
  - 3.4.2 Scattering with complex band structure 73
- 3.5 Conclusions 76

4 Geometry effects in topologically confined bilayer graphene loops 79
- 4.1 Introduction 79
- 4.2 Theory 81
  - 4.2.1 A quantum perimeter model (QPM) 81
  - 4.2.2 A quantum 2D model (Q2DM) 83
- 4.3 Results 84
- 4.4 Discussions 90
  - 4.4.1 Modeling 90
  - 4.4.2 Valley reversal 92
- 4.5 Conclusions 93

5 Trivial and topological bound states in bilayer graphene quantum dots and rings 95
- 5.1 Introduction 95
- 5.2 Model 98
- 5.3 Results 101
- 5.4 Discussion and conclusions 104

6 Conclusion and perspective 107

7 Appendices 111
- 7.1 Appendix A Fermion doubling problem in Dirac-like Hamiltonians 111
- 7.2 Appendix B Current calculation 114

Chapter 1

Introduction

1.1 Motivation

Many devices in our daily life can operate using the electron's charge. This property allows us to transmit and store information. Typically, in classical electronics information is encoded in digital bits (either 0 or 1). In the context of quantum mechanics, it is possible to encode information by means of "quantum bits" or qubits, which represent superpositions of 0 and 1. These can be implemented in certain materials by employing an additional electronic degree of freedom, namely, its spin (see Fig 1.1) [1, 2]. Generation of spin-polarized electron currents can be achieved in semiconductors, leading to sophisticated schemes that manipulate single electron spins in quantum dots [3]. In the field called spintronics, thus, the electron spin is the main tool for electronic (classical or quantum) applications.

Additionally, in a different class of materials, the electronic energy spectrum presents two special points called valleys that play the role of an effective spin. Therefore, the name valleytronics is coined for this new approach of making use of the valley degree of freedom to encode bits of quantum information [5]. One of the candidate materials for valleytronic applications is graphene [6]. Graphene is a system made up of a single layer of carbon atoms that arrange themselves in a honeycomb structure with sp^2 hybridized bonds. Charge carriers in graphene at low energy are massless Dirac fermions that exhibit

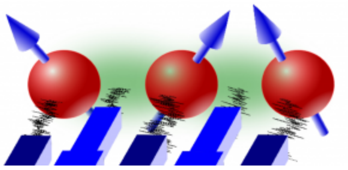

Figure 1.1: Sketch representing three spin qubits under application of three gate voltages. Image taken from Ref. [4].

minimal conductivity near the Dirac points where those points describe the two valleys.

On the other hand, topology is the study of the characteristics of space that remain constant during repeated transformations. A topological current can be produced in crystalline solids by the electronic wavefunction's Berry phase. The spin Hall current that results from spin-orbit coupling is one example, as is the quantum Hall current in a magnetic field. Such topological transport is resilient against material imperfections and flaws, which is a property much desired in prospective electronic applications. Switching and continuously tuning the topological transport is essential in these applications [7]. The massless Dirac equation that governs the behavior of electrons makes graphene's quantum Hall effect quite distinct from that seen in conventional semiconductors like silicon which makes graphene topologically different.

This thesis aim is to study the electronic and topological properties of graphene nanostructures near the Dirac points. We will focus on bilayer graphene (BLG), which comprises two sheets of graphene. Remarkably, in BLG it is possible to open a gap by breaking the inversion symmetry with the aid of an externally applied electric field. This unique property opens the door for researchers to investigate the effect of different perturbations on BLG such as magnetic fields or to configure voltage gates applied to the sample. We consider in this thesis the case of BLG Bernal stacked structures. This system shows important characteristics and properties. For example, BLG hosts electronic topological states when the spatially inhomogeneous potential is applied to each layer with opposite signs. These topological states are chiral and fourfold degenerate.

In our thesis, we want to further analyze the fundamental properties of electronic states in BLG when topology plays a major role. This goal is achieved by confining electrons to one-dimensional (1D) and zero-dimensional (0D) structures like quantum point contacts and dots, respectively. The gap generated under the application of an electric field across the two sheets of graphene can be used to design tunnel barriers, which are a prerequisite for engineering point contacts and dots.

The application of an electric field changing its sign along the graphene sheets creates a domain wall for the chiral states, which then propagate along the wall. This type of motion corresponds to a so-called kink state [8]. Its topological character is hence induced by both band inversion and confinement. Noticeably, the kink states propagate in opposite directions for each valley, thereby displaying valley-momentum locking.

We study in our thesis the scattering phenomena of those states by presenting a system hosting kink states. We consider two types of systems, namely, constrictions and side loops. We show that both work as a means of controlling the backscattering of those kink states and consequently affecting the transport properties of the junction. We examine the conductance and energy spectrum for each case. Furthermore, we discuss another type of system that emphasizes geometrical effects in BLG quantum dots. Our discussion is based on an analysis of the energy spectrum, considering loops of higher to lower symmetry. We find that for small-size loops the topological spectrum is affected by the loop shape. Importantly, our proposals discuss in detail the role of the electronic valley and therefore can be interesting for valleytronics research.

This Ph.D. book is organized into six chapters: A first general chapter will serve as a theoretical background for monolayer and bilayer graphene systems. We will additionally consider fundamental ideas of quantum transport and its paradigmatic systems (quantum dots and quantum point contacts). We continue with a second chapter where we describe the trivial and topological confinement in bilayer graphene wires. The last three chapters include our published works on BLG structures.

Our first paper [9] investigates the scattering of topological kink-antikink states in BLG systems with lateral confinement. We propose a nanodevice for topological quantum valley transport determined by kink-antikink potentials. Since motion is interlocked with the valley degree of freedom, the injection of electrons can be valley polarized. If we now take into account the robustness of topological states, our device is then attractive for possible applications within topological valleytronics. We calculate the conductance in this system attached to the source and drain electrodes. We find that due to a central region of scattering the conductance shows an anomalous behavior for the first proposal (constriction) and resonance peaks for the second proposal (side loops). Interestingly, in both cases, a study of the conductance reveals the system energy spectrum. We also find that the systems can be valley polarized and present valley accumulation. This finding makes our nanodevice interesting because it can work as a valley filter.

The second paper [10] discusses geometrical effects in topologically confined BLG loops. Motivated by the previous results on side loops, we now explore how the geometry or the perimeter of the loops affects the energy spectrum. We consider loops of higher to lower symmetry (circle, square, rectangle, and irregular polygon) and find that for short perimeters the spectrum depends on the loop shape. We also obtain that zero-energy states exhibit a characteristic pattern that strongly depends on spatial symmetry. When we apply a magnetic field of 500 mT we notice that the spectrum undergoes a valley splitting and asymmetry. Consequently, these results are interesting as well for valleytronic applications.

Finally, our third paper [11] discusses and compares the two different types of confinement (i.e., trivial and topological) in BLG gated with top and bottom symmetrical microelectrodes. Trivial confinement corresponds to applying the same polarity to all top gates, which is opposed to that of all the bottom ones. Topological confinement requires the polarity of part of the top-bottom pairs of gates to be reversed. Our study shows that the main qualitative difference between trivial and topological bound states manifests itself in the magnetic field dependence. We illustrate this finding with an explicit calculation of the energy spectrum for quantum dots and rings. Trivial confinement shows bunching of levels into degenerate Landau bands, with an energy asymmetric gap, while topological confinement shows no field-induced gap and a sequence of state branches always crossing zero-energy.

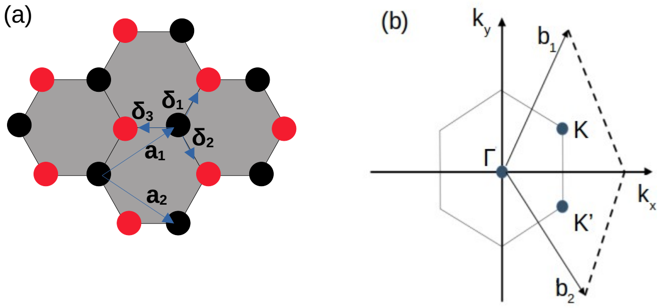

Figure 1.2: (a) Graphene lattice in the real space defined by the base vectors a_1 and a_2 and the sublattices A(black) and B(red). (b) Reciprocal lattice with Γ the center of the first Brillouin zone and b_1 and b_2 the corresponding base vectors.

1.2 Graphene

1.2.1 Monolayer graphene

1.2.1.1 Atomic properties

Graphene is a two-dimensional (2D) material composed of carbon atoms onto a hexagonal lattice. In modern terms, graphene forms the building block for additional materials such as graphite (stacked graphene layers), nanotubes (rolled-up graphene layers), etc. [12,13]. The electronic orbitals in graphene are sp^2 hybridized. These wave functions that are located in the plane form the covalent bonds which ensure the stability of the crystal lattice and are at the origin of the mechanical properties of graphene. For the electronic properties, the interesting aspect is that there is an orbital left, the p_z orbital, hosting one electron. This p_z orbital is perpendicular to the plane formed by the carbon atoms and forms π bonds. Since the p_z orbital contributes with one electron, graphene is a system with one electron per lattice site. The π orbitals are precisely the states responsible for the unusual electronic properties of graphene [14].

The primitive cell of graphene is made up of two carbon atoms, which we hereafter label A and B (see Fig. 1.2. (a)). We can then speak about two corresponding sublattices, namely, A and B. The first Brillouin zone is also hexagonal (see Fig. 1.2. (b)). Therefore, the lattice is defined by the following two base vectors with $a = 1.42$ Å the lattice spacing:

$$\vec{a}_1 = \frac{a}{2}(3, \sqrt{3}), \quad \vec{a}_2 = \frac{a}{2}(3, -\sqrt{3}), \tag{1.1}$$

while the vectors connecting neighboring atoms are:

$$\vec{\delta}_1 = \frac{a}{2}(1, \sqrt{3}), \quad \vec{\delta}_2 = \frac{a}{2}(1, -\sqrt{3}), \quad \vec{\delta}_3 = -a(1, 0). \tag{1.2}$$

1.2.1.2 Electronic properties

The starting point for a careful investigation of the electronic structure of graphene is a tight-binding model [15]. This model yields the electronic bands around the two points K and K' defined as: $K = \frac{2\pi}{3a}$ $(1,\frac{1}{\sqrt{3}})$ and $K' = \frac{2\pi}{3a}$ $(1,-\frac{1}{\sqrt{3}})$. As we show below, close to these points, the electronic states are described at low energy by a relativistic Dirac equation [16], which is crucially not like the non-relativistic Schrödinger equation valid for the low-energy states of 2D electron gases in III-V semiconductors (GaAs, InAs, etc.).

Let $(a_k^+,\ b_k^+\ ,\ a_k,\ b_k)$ be the operators of creation and annihilation for electrons in reciprocal space for sites A and B with k the momentum characterizing the two Bloch functions. γ_0 is the overlap between the orbitals of the closest neighbors in the plane with a value between 2.7 and 3 eV. Then, the tight-binding Hamiltonian reads:

$$H = \sum_k (a_k^+ b_k^+) \begin{bmatrix} 0 & -\gamma_0 f(k) \\ -\gamma_0 f(k)^* & 0 \end{bmatrix} \begin{bmatrix} a_k \\ b_k \end{bmatrix}, \tag{1.3}$$

where

$$f(\vec{k}) = e^{i\vec{k}\vec{\delta}_1} + e^{i\vec{k}\vec{\delta}_2} + e^{i\vec{k}\vec{\delta}_3}. \tag{1.4}$$

The eigenvalues of Eq. (1.3) are:

$$E = \pm\gamma_0 \sqrt{f(k) f(k)^*}, \tag{1.5}$$

or

$$E = \pm\gamma_0 \sqrt{1 + 4\cos\left(\frac{3}{2}k_x a\right)\cos\left(\frac{\sqrt{3}}{2}k_y a\right) + 4\cos^2\left(\frac{\sqrt{3}}{2}k_y a\right)}. \tag{1.6}$$

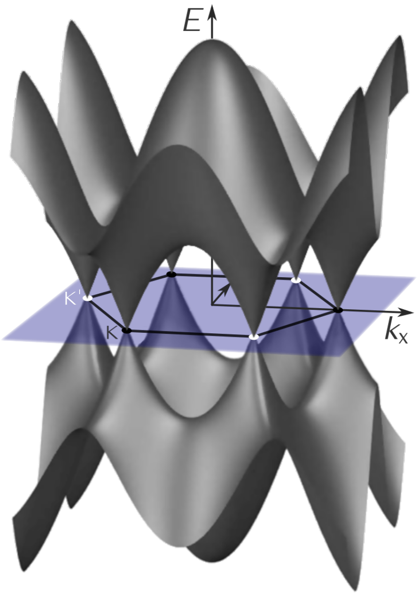

Figure 1.3: Graphene band structure where the valence band and the conductance band touch each other at the two points K and K' with $\gamma_0 = 2.74$ eV and $a = 1.42$ Å. Image taken from Ref. [17].

Figure 1.3 shows the result from Eq. (1.6) as a function of momentum. In the electrically neutral case, the Fermi level separates all filled bands from the empty ones at zero temperature and lies right at the tips of the cones. Therefore, undoped graphene is a semimetal.

The first band (the minus sign in Eq. (1.6)) below the Fermi level is the valence band whereas the first band (the plus sign in Eq. (1.6)) is located above this is the conduction band. For all possible values of k there is a gap between both bands except at six points (two are inequivalent–the valleys), where the gap is zero. At these points the dispersion relationship is linear in the momentum (see below), which is a peculiarity of graphene. Consequently, the regions around those points of the electron band structure of graphene are called the "Dirac cones". Inside the Dirac cone, the density of states is zero at its vertex and increases linearly further away from it.

To describe the low energy electronic states in the Dirac cone (see Fig. 1.4), we must consider wave vectors k close to the Dirac points. Thus, we obtain two electron Hamiltonians, one per valley. Let us then write the function $f(\vec{k})$ in terms of the small perturbation

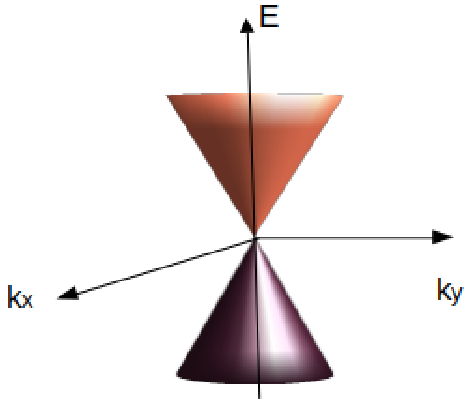

Figure 1.4: The bands near a Dirac point K or K', known as a Dirac cone, show a linear dispersion.

$\vec{q} = \vec{k} - \vec{K}$ as

$$f(\vec{K}+\vec{q}) = e^{-iK_x a} e^{-iq_x a} \left[1 + 2e^{i3(K_x+q_x)a/2} \cos\left(\frac{\sqrt{3}(K_y+q_y)a}{2} \right) \right]. \tag{1.7}$$

Therefore, in a Taylor expansion up to the first order in q we find:

$$f(\vec{K}+\vec{q}) = -\frac{3a}{2}(q_x + iq_y). \tag{1.8}$$

The Hamiltonian near the K valley becomes

$$H = \sum (a_k^+ b_k^+) \begin{bmatrix} 0 & -\gamma_0 f(\vec{K}+\vec{q}) \\ -\gamma_0 f(\vec{K}+\vec{q})^* & 0 \end{bmatrix} \begin{bmatrix} a_k \\ b_k \end{bmatrix}. \tag{1.9}$$

We define the constant $v_F = 3a\gamma_0/2\hbar$, termed the Fermi velocity, whereas $q_{x,y} \rightarrow -i\partial/\partial x, y$ is the momentum operator. Then, the Hamiltonian can be further simplified as

$$H(\vec{q}) = \hbar v_F \begin{bmatrix} 0 & q_x - iq_y \\ q_x + iq_y & 0 \end{bmatrix}. \tag{1.10}$$

Near K' we can make a similar calculation, with now $K_x' = K_x$ and $K_y' = -K_y$.

The results presented above highlight the necessity of including both sublattices A and B as well as both crossing points K and K' in our wave functions, which are denoted as $\varphi^{\pm}_{A,B}$ where ± is the valley index. The total Hamiltonian for the system including the two valleys can then be represented in the following way:

$$H = \hbar v_F \begin{bmatrix} 0 & q_x - iq_y & 0 & 0 \\ q_x + iqy & 0 & 0 & 0 \\ 0 & 0 & 0 & -q_x + iq_y \\ 0 & 0 & -q_x - iq_y & 0 \end{bmatrix} \begin{bmatrix} \varphi_A + \\ \varphi_B + \\ \varphi_A - \\ \varphi_B - \end{bmatrix}. \tag{1.11}$$

An even more convenient representation utilizes the Pauli matrices [18–20] since the two lattice sites are mathematically equivalent to a two-level system, i.e., a pseudospin:

$$H = \hbar v_F \begin{bmatrix} \sigma.q & 0 \\ 0 & -\sigma.q \end{bmatrix}. \tag{1.12}$$

or

$$H = \hbar v_F \ \vec{\alpha}.\vec{q}, \tag{1.13}$$

where $\alpha = \begin{bmatrix} \sigma & 0 \\ 0 & -\sigma \end{bmatrix}$. For reference purposes, we recall the three Pauli matrices:

$$\sigma_x = \begin{bmatrix} 0 & 1 \\ 1 & 0 \end{bmatrix}, \ \sigma_y = \begin{bmatrix} 0 & -i \\ i & 0 \end{bmatrix}, \ \sigma_z = \begin{bmatrix} 1 & 0 \\ 0 & -1 \end{bmatrix}. \tag{1.14}$$

Therefore, the sublattice pseudospin represents in the wave function the weight amplitude on the A and B sublattices.

Equation (1.13) is a linear equation in the momentum, and the Fermi velocity v_F plays the role of fixed electronic velocity or effective speed of light. At small energies, the Dirac fermions have therefore zero mass. This is the relativistic limit that we mentioned before, However, caution is here in order since at higher energies this approximation is no longer valid and Eq. (1.13) breaks down.

1.2.2 Bilayer graphene

When two sheets of graphene are coupled together, the hexagonal lattice of each layer consists of two Bravais sublattices of sites A_1 B_1 for layer 1 and A_2 B_2 for layer 2.

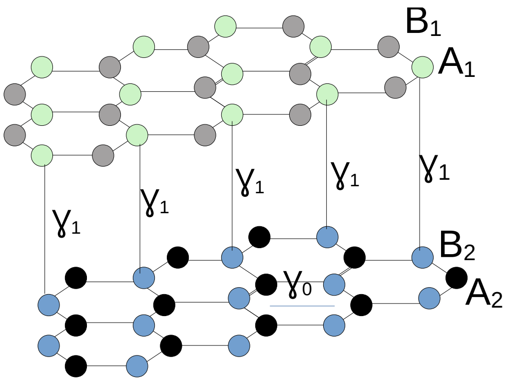

Figure 1.5: Bilayer graphene structure with sublattice atoms for layers 1 and 2 being A_1, B_1, A_2 and B_2 respectively, and γ_1 is the interlayer coupling.

Therefore, in the plane the hopping is parametrized by the coupling parameter $\gamma_{A_1B_1} = \gamma_{A_2B_2} = \gamma_0$ as in Eq. (1.13). In the case of Bernal stacking (AB stack) considered in this book, the interlayer coupling between the planes is given by $\gamma_{A_1B_2} = \gamma_1$, which takes the value of 0.3 eV. Because of this strong coupling, dimers produced from pairs of $A_1 - B_2$ orbitals form a high energy band.

To calculate the band structure and study the electronic properties of bilayer graphene (BLG), we apply the tight-binding model similar to the monolayer case (see Sec. 1.2.1), the difference being that for bilayers we have two layers with two atoms for each sublattice. We are interested in low energy properties, which are dominated by the band structure near the valleys K and K' .

Near the center of the valleys, the Hamiltonian is a 4×4 matrix as opposed to the two 2×2 matrices of the monolayer (see Eq. (1.10)). The Hamiltonian can be divided into 4 subblocks that connect graphene layers between 1 and 2 and between themselves. In the basis $(A_1\ B_2\ A_2\ B_1)$ the Hamiltonian reads :

$$H = \begin{bmatrix} \frac{1}{2}\Delta & v_F\pi & 0 & 0 \\ v_F\pi^+ & \frac{1}{2}\Delta & \gamma_1 & 0 \\ 0 & \gamma_1 & -\frac{1}{2}\Delta & v_F\pi \\ 0 & 0 & v_F\pi^+ & -\frac{1}{2}\Delta \end{bmatrix}. \tag{1.15}$$

The resulting four bands are four times degenerate in spin and valley. As discussed earlier,

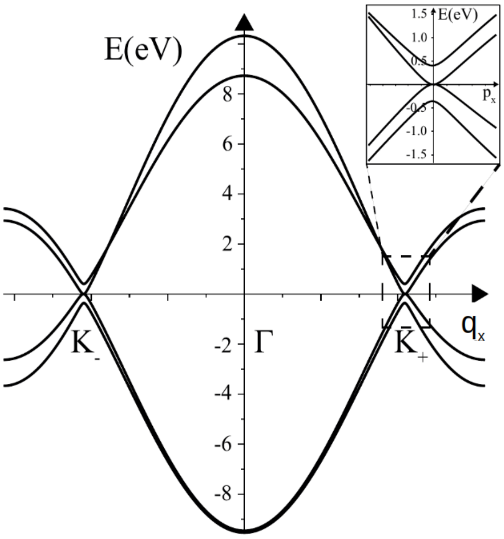

Figure 1.6: Bilayer graphene band structure as a function of momentum near the center of the first Brillouin zone and in the presence of an externally applied electric field $\Delta \neq 0$. K and K' are the two valleys. The inset represents the gapless bands when $\Delta = 0$. Image taken from Ref. [21].

they arise from a linear combination of the p_z orbitals of each site A and B of the two layers of graphene. In Eq. (1.15) we define $\pi = \hbar(\tau_z q_x + iq_y)$, $\pi^+ = \hbar(\tau_z q_x - iq_y)$. The index $\tau_z \to \pm$ describes K and K' valleys, respectively. Finally, Δ is the asymmetry between onsite energies in the two layers. When $\Delta = 0$, the two bands (valence and conduction bands) touch at the neutrality point whereas two other bands are higher in energy due to the aforementioned interlayer coupling. The electronic transport properties are determined by the electronic states of bands closest to the Fermi level, which in the undoped case is taken as the origin of energies ($E = 0$).

Similary to Eq. (1.12) the Hamiltonian can be written as :

$$H = v_F\ \tau_z\ p_x\ \sigma_x + v_F\ p_y\ \sigma_y + \gamma_1(\lambda_+\sigma_- + \lambda_-\sigma_+) + \frac{1}{2}\Delta\ \lambda_z, \tag{1.16}$$

with $p_{x,y} = \hbar q_{x,y}$ the momentum operators. The sublattice σ_{xyz} , valley τ_{xyz} and layer λ_{xyz} operators are Pauli matrices for these three discrete degrees of freedom. At zero magnetic field, the diagonalization of Eq. (1.16) gives the following eigenergies:

$$E^e \pm = \frac{1}{2}\sqrt{\gamma_1 \pm \sqrt{\gamma_1^2 + 4\epsilon^2 + 4\epsilon^2 \mathit{\Delta}^2/\gamma_1^2} + \mathit{\Delta}^2(1-\epsilon^2/\gamma_1^2)}, \tag{1.17}$$

and

$$E^h \pm = -\frac{1}{2}\sqrt{\gamma_1 \pm \sqrt{\gamma_1^2 + 4\epsilon^2 + 4\epsilon^2 \mathit{\Delta}^2/\gamma_1^2} + \mathit{\Delta}^2(1-\epsilon^2/\gamma_1^2)}, \tag{1.18}$$

with $\epsilon = \hbar \upsilon_F \sqrt{q_x^2 + q_y^2}$. Inset of Fig. 1.6 shows these eigenergies that determine the band structure of bilayer graphene. For $\mathit{\Delta} = 0$ the spectrum is gapless. More importantly, for $\mathit{\Delta} \neq 0$ a gap opens between the two lowest lying bands. Unlike monolayer graphene, which has a linear spectrum, bilayer graphene shows a parabolic dependence at small energies due to the interlayer coupling. As a consequence, electrons become massive in bilayer graphene although their effective mass is very small ($m^* = \frac{\gamma_1}{2v_F^2} = 0.033\ m_e$) [22].

1.2.3 Magnetic field dependence

We now discuss the magnetic properties. Let us begin with monolayer graphene. The interesting case arises when the magnetic field B is orthogonal to the graphene layer. By using the Peierls substitution in the Hamiltonian obtained from the tight-binding model (Eq. (1.12)), the momentum can be accordingly modified [23]. This substitution amounts to $q \rightarrow q_i' = q_i + eA_i$, where A_i is the i-th component of the vector potential. The vector potential can be chosen in the Landau gauge as $\vec{A} = (-By, 0)$.

Using the linear approximation for monolayer graphene in Eq. (1.13) we replace the momentum at a finite magnetic field in the vicinity of the K point:

$$H = \hbar\upsilon_F(\vec{q} + e\vec{A}).\vec{\sigma} = \hbar\upsilon_F(\sigma_x q_x' + \sigma_y q_y') = \hbar\upsilon_F \begin{bmatrix} 0 & q_x' - iq_y' \\ q_x' + iq_y' & 0 \end{bmatrix}. \tag{1.19}$$

Thus,

$$H = \hbar\upsilon_F \begin{bmatrix} 0 & \sqrt{2eB}a \\ \sqrt{2eB}a^\dagger & 0 \end{bmatrix} = \sqrt{2}\frac{\hbar\upsilon_F}{l_B} \begin{bmatrix} 0 & a \\ a^\dagger & 0 \end{bmatrix}, \tag{1.20}$$

with $\sqrt{2eB}a = q_x' - iq_y'$, $\sqrt{2eB}a^\dagger = (q_x' + iq_y')$ and $l_B = \sqrt{\frac{\hbar}{eB}}$. Here, a and $a^\dagger$ are ladder operators. The eigenenergies can be obtained by diagonalizing Eq. (1.20) considering the

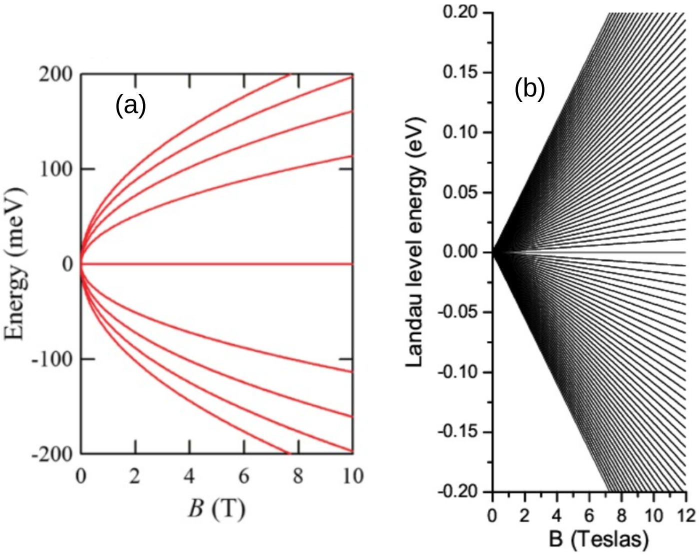

Figure 1.7: (a) Landau levels as a function of the magnetic field B for monolayer graphene, and (b) for bilayer graphene. Image taken from Ref. [24].

square of the Hamiltonian:

$$H^2 = 2\left(\frac{\hbar v_F}{l_B}\right)^2 \begin{bmatrix} a^\dagger a + 1 & 0 \\ 0 & a^\dagger a \end{bmatrix}, \tag{1.21}$$

where we have used the property $[a, a^+] = 1$. As usual, $a^+ a$ is the number operator. For an electron wavefunction ψ_n, $a^+ a \mid \psi_n >= n \mid \psi_n >$. The Hamiltonian can be diagonalized by the eigenstates $\psi_n = (\mid n-1>, \pm \mid n>)$, with $n = 0, \pm 1, \pm 2 \ldots$.

We solve the equation

$$H^2 \mid \psi >= \lambda \mid \psi >, \tag{1.22}$$

and find the eigenergies

$$\epsilon = \mathrm{sgn}(n)\sqrt{2eB}\ \upsilon_F \hbar\sqrt{\mid n \mid}, \tag{1.23}$$

or

$$\epsilon = \mathrm{sgn}(n)\hbar\omega\sqrt{\mid n \mid}, \tag{1.24}$$

with $\omega = \sqrt{2eB}\upsilon_F$ the effective cyclotron frequency. The Landau level index, n, can be positive or negative. Positive values correspond to electrons (conduction band) while negative values correspond to holes (valence band). The spectrum of graphene as a function of magnetic field is plotted in Fig. 1.7(a). Interestingly, there is a Landau level with zero energy. Its eigenstate is $(0, \mid 0 >)$ for the K valley, which implies that only the B sites are occupied. (The A sites are respectively occupied for the K' valley). Moreover, the Landau levels are not equidistant unlike the nonrelativistic Landau levels found in, e.g., GaAs 2D electron gases [25].

For bilayer graphene, we neglect for the moment the effect of the potential difference between layers and use the same Peierls subtitution as in the monolayer (Eq. (1.19)). At low energies ($E < \gamma_1/4$), bilayer graphene can be described with an approximate 2-band model that yields a 2×2 Hamiltonian obtained from the 4-band Hamiltonian given by Eq. (1.15), integrating out the higher energy dimers B1, A2 [21]. Then, for small energies the Hamiltonian becomes

$$H_{BLG} = \hbar\upsilon_F \begin{bmatrix} 0 & q^2 \\ q\dagger & 0 \end{bmatrix} = \hbar\omega_c \begin{bmatrix} 0 & a^2 \\ (a^\dagger)^2 & 0 \end{bmatrix}. \tag{1.25}$$

from which we derive

$$(H_{BLG})^2 = (\hbar\omega_c)^2 \begin{bmatrix} a^2(a^\dagger)^2 & 0 \\ 0 & (a^\dagger)^2 a^2 \end{bmatrix}, \tag{1.26}$$

with $\omega_c = \frac{eB}{m^*}$ the cyclotron frequency and m^* the previously inferred effective mass of bilayer graphene electrons. Since $a^2(a^\dagger)^2 = (n+1)(n+2)$ and $(a^\dagger)^2 a^2 = (n-1)n$, the eigenstate is $\psi = (\mid n-2 >, \pm \mid n >)^T$ and the energy levels are represented by

$$\epsilon_n = \mathrm{sgn}(n)\hbar\omega_c\sqrt{\mid n \mid (\mid n \mid -1)}. \tag{1.27}$$

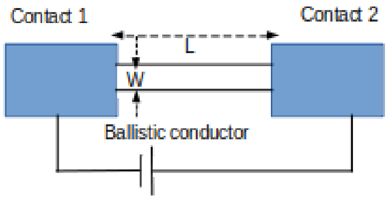

Figure 1.8: A ballistic conductor between two contacts represented with electron reservoirs. Image taken from Ref. [25]

As compared the Eq. (1.23), the Landau spectrum of Eq. (1.27) (see figure Fig. 1.7.b) presents a doubly degenerate zero energy state. Moreover, Eq. (1.27) is equidistant at high values of n similarly to the nonrelativistic behavior found in conventional 2D electron systems.

1.3 Quantum Transport

Electronic transport describes the response of electrons, which interact with the lattice and with themselves, to the application of electric or magnetic fields. In this section, we will discuss the fundamentals of transport in mesoscopic systems, which are conductors that have characteristic dimensions smaller than the mean free path ($L_m = v_F \tau_t$) and the phase-relaxation length ($L_\phi = v_F \tau_\phi$), where τ_t is the transport relaxation time and τ_ϕ is the typical time for phase-breaking collisions. We will also discuss two prototypical mesoscopic systems that are relevant for the purpose of this book, namely, quantum dots and quantum point contacts.

1.3.1 Landauer-Büttiker model

We will summarize the Landauer-Büttiker scattering approach valid for the ballistic regime of transport. Our discussion is based on Ref. [25]. A ballistic 2D conductor, see Fig. 1.8, whose length L and width W satisfies $L_m \gg L, W$, is a system where no diffusion phenomena occur. The Landauer-Büttiker model considers in that case the transport phenomena by taking into account the current in the system in terms of transmission probabilities.

To compute the current in a ballistic conductor one first calculates the current which is carried by each transverse mode. Semiclassically, we can write this current as:

$$I^+ = \frac{e}{L}\sum_k v f^+(E) = \frac{e}{L}\sum_k \frac{1}{\hbar}\frac{\partial E}{\partial k} f^+(E), \tag{1.28}$$

where v is the electron velocity and f is the Fermi distribution function for electrons traveling in the positive direction. Using the continuum limit $\sum_k \to 2(\text{for spin}) \times (L/2\pi) \int dk$ we obtain

$$I^+ = \frac{2e}{h}\int_{-\infty}^{+\infty} f^+(E)M(E)dE, \tag{1.29}$$

with $M(E) = \sum_N \theta(E - \epsilon_N)$ is a function defining the number of modes that are at energy E above the energy of transverse modes ϵ_N.

To find the net current I, we must substract the current contribution of electrons traveling in the negative direction:

$$I = \frac{2e}{h}\int_{-\infty}^{+\infty} dE(f^+(E) - f^-(E))M(E) = \frac{2e}{h}\int_{\mu_R}^{\mu_L} dEM(E). \tag{1.30}$$

where in the last equality we have assumed zero temperature for simplicity. The current that traverses the ballistic channel (and measured at the contacts) is therefore

$$I = \frac{2e}{h}M(\mu_L - \mu_R), \tag{1.31}$$

where M is the total number of open modes. Our simplifications have led to a linear dependence of I for arbitrary applied voltage $\mu_L - \mu_R$. In general, this is true only for very small voltages. We focus on that case because the main results of this thesis are obtained for the linear regime of transport, which is easily accessible in the lab.

If the transmission through the transverse modes is imperfect, namely, $T < 1$, then Eq. (1.31) should be modified as

$$I^+ = \frac{2e}{h}MT(\mu_L - \mu_R), \tag{1.32}$$

Since the linear conductance formula in general is given by

$$G = \frac{I}{(\mu_L - \mu_R)/e}. \tag{1.33}$$

we arrive at the Landauer's formula for the conductance:

$$G = \frac{2e^2}{h} MT. \tag{1.34}$$

This is a remarkable result. It states that the dissipative response of a ballistic channel is given in terms of the quantum-mechanical transmission of the channel. Notably, for transparent channels ($T = 1$) the conductance becomes quantized in units of $2e^2/h = 7.7 \times 10^{-5}$ S.

1.3.1.1 Current for nonzero temperature and bias

Finite temperature effects lead to thermal smearing of the conductance quantization. To see this, let us calculate the influx of electrons per unit energy from the lead left

$$i_L^+(E) = (2e/h)Mf_L(E), \tag{1.35}$$

and substract the influx from right contact,

$$i_R^-(E) = (2e/h)M'f_R(E), \tag{1.36}$$

where M' is the number of modes in the right lead. Since the outflux from the two leads is given by

$$i_L^-(E) = (1-T)i_L^+(E) + T'i_2^-(E), \tag{1.37}$$

for the left lead

$$i_R^+(E) = (T)i_L^+(E) + (1-T')i_2^-(E), \tag{1.38}$$

for the right lead, the net current results in

$$i(E) = i_L^+ - i_L^- = i_R^+ - i_R^- = \frac{2e}{h}[M(E)T(E)f_L(E) - M'(E)T'(E)f_R(E)]. \tag{1.39}$$

We define $\overline{T}(E) = M(E)T(E)$. Hence,

$$i(E) = \frac{2e}{h}[\ \overline{T}(E)f_L(E) - \overline{T'}(E)f_R(E)\ ]. \tag{1.40}$$

The total current is then

$$I = \int i(E)dE, \tag{1.41}$$

where $i(E) = \frac{2e}{h}\overline{T}(E)[f_L(E) - f_R(E)]$ and $\overline{T}(E) = \overline{T'}(E)$. We find

$$I = \frac{2e}{h}\int \left([\overline{T}(E)[f_L(E) - f_R(E)]_{eq} + [f_L(E) - f_R(E)]_{eq}\overline{T}(E)]\right) dE. \tag{1.42}$$

This equation is exact for independent electrons. Out of equilibrium we can use a Taylor expansion up to first order in the applied bias:

$$f_L(E) - f_R(E) \simeq [\mu_L - \mu_R]\left(\frac{\partial f}{\partial \mu}\right)_{eq} = \left(-\frac{\partial f_0}{E}\right)[\mu_L - \mu_R], \tag{1.43}$$

with f_0 is the Fermi function at equilibrium. As a consequence, the linear conductance in this case can be written as

$$G = \frac{2e^2}{h}\int \overline{T}(E)\ (-\frac{\partial f_0}{\partial E})dE. \tag{1.44}$$

At low temperature one has $(-\frac{\partial f_0}{\partial E}) \approx \delta(E_F - E)$ and we recover Eq.(1.34) with $M = 1$. At higher temperatures, the effective transmission is smeared out and the conductance presents deviations from flat steps.

A final remark: despite the fact that our derivation is semiclassical, it can be justified with a fully quantum mechanical calculation, see Ref. [26].

1.3.2 Transport through a quantum dot

The advances in the semiconductor and nanotechnology domains made it possible in the 1980's and 90's to grow 0D nanostructures called quantum dots (QD) [27]. The peculiarity of a quantum dot is that they are around ten nanometers in size, in which carriers (electrons) are confined in all three directions of space. In this part, we will discuss the transport properties of a quantum dot using the Landauer-Büttiker formalism

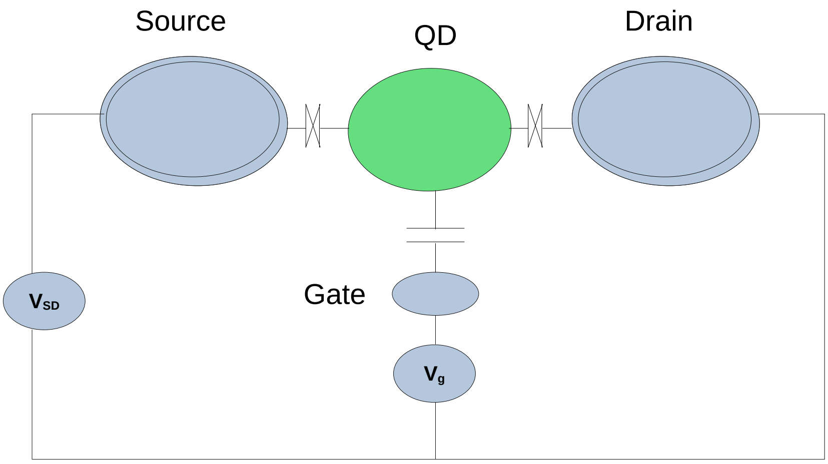

Figure 1.9: Schematic representation of a gated quantum dot connected to source and drain electronic reservoirs. These are are massive terminals (not in scale in the plot) while the dot size is of the order of $\simeq 10-100$ nm

presented earlier. To this end, we need the transmission probability in the system.

If we model the dot as a double barrier system, the transmission of an electron with longitudinal energy E_L is:

$$T_L(E_L) = \frac{T_1 T_2}{1 - 2\sqrt{R_1 R_2}\cos\theta(E_L) + R_1 R_2}, \tag{1.45}$$

where T_1, T_2 are the transmission probabilities through barrier scatterers 1 and 2 and R_1, R_2 are the reflection probabilities. In Eq.1.45, θ is the phase shift acquired in one round-trip between the scatterers. We consider thick barriers ($R_1, R_2 \simeq 1$) to calculate an approximate transmission near resonance,

$$T_L = \frac{T_1 T_2}{\left[\frac{T_1+T_2}{2}\right]^2 + 2(1 - \cos\theta(E_L))}. \tag{1.46}$$

Then, around the resonant energy E_r we can make the approximation $1 - cos\theta(E_L) \simeq \frac{1}{2}(\frac{d\theta}{dE_L})^2(E_L - E_r)^2$. Thus, the transmission becomes

$$T_L(E_L) = \frac{\Gamma_1 \Gamma_2}{(E_L - E_r)^2 + (\frac{\Gamma_1+\Gamma_2}{2})^2} \ , \tag{1.47}$$

where $\Gamma_1 = \frac{dE_L}{d\theta}T_1$ and $\Gamma_2 = \frac{dE_L}{d\theta}T_2$ can be interpreted as the width associated to the coupling between the resonance and the tunnel barriers.

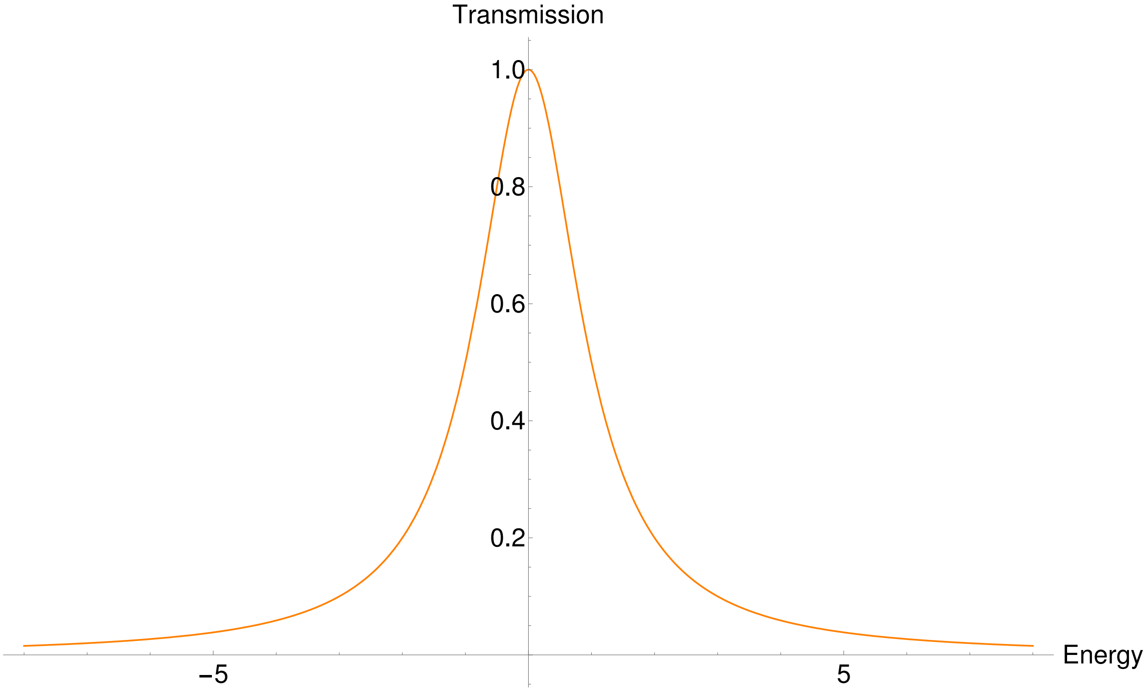

Figure 1.10: Transmission probability of an electron from source to drain ($T = 1$ is perfect transmission) through a quantum dot. Parameters: $\Gamma_1 = 1$, $\Gamma_2 = 1$ and $E_r = 0$.

Figure 1.10 shows the behavior of the transmission coefficient given by Eq. (1.48). Perfect transmission occurs when the electrons energy hits the resonance. Eq. (1.48) is then a Lorentzian function.

Defining

$$A(\varepsilon) = \frac{\Gamma}{\varepsilon^2 + (\Gamma/2)^2} , \tag{1.48}$$

with $\Gamma = \Gamma_1 + \Gamma_2$, the total transmission in the presence of multiple resonances E_m is:

$$T(E) = \frac{\Gamma_1 \Gamma_2}{\Gamma_1 + \Gamma_2} \sum_m A(E - E_m) . \tag{1.49}$$

Using Eq. (1.45) we can give the linear conductance for a quantum dot:

$$G = \frac{2e^2}{h} \frac{\Gamma_1 \Gamma_2}{\Gamma_1 + \Gamma_2} \sum_m A(E - E_m) , \tag{1.50}$$

which consists of a series of resonant peaks as the resonances are scanned with the aid of an external gate electrode.

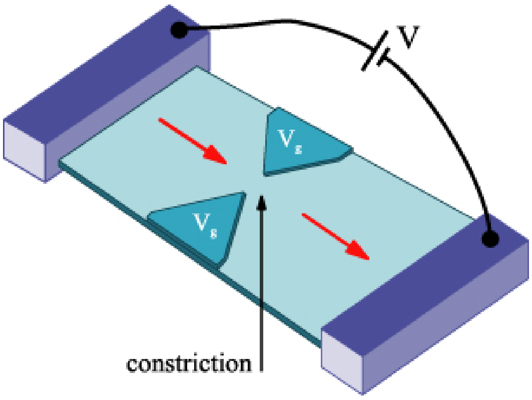

Figure 1.11: Sketch of a quantum point contact system with V the potential bias applied to the attached terminals. Image taken from Ref. [29].

1.3.3 Quantum point contact

A quantum point contact (QPC) is a narrow constriction between two wide, electrically conducting regions. The width of a QPC is of the order of few nanometers [28]. By applying the potential bias V as in Fig. 1.11 electrons are allowed to pass through the constriction. As in the case of QDs, we now sketch the derivation of the QPC transmission in order to derive the conductance for this system.

We consider the Schrodinger's equation for independent electrons in two dimensions (xy plane):

$$\left[\frac{\hbar^2}{2m^*}\frac{\partial^2}{\partial y^2} + V(x,y)\right]\chi(x,y) = E\ \chi(x,y), \tag{1.51}$$

where $V(x,y)$ is the confining potential that defines the QPC. Since confinement is in y direction and is translationally invariant in the x direction, the total wave function can be decomposed as:

$$\Psi(x,y) = \chi(y)e^{ikx}. \tag{1.52}$$

Here, k is the momentum along the propagation direction (x).

The total energy for electrons is then:

$$E_n(k) = \frac{\hbar^2 k^2}{2m^*} + E_n, \tag{1.53}$$

where E_n are the energy subbands due to the transversal confinement potential. Assuming

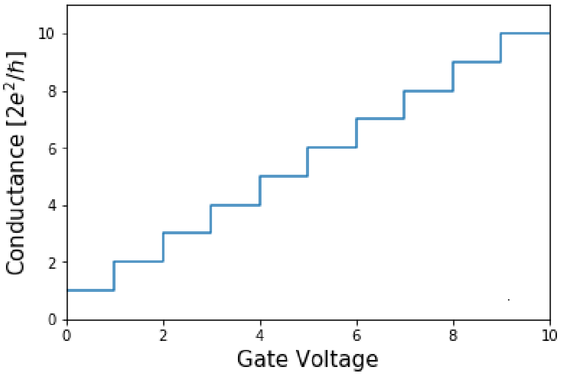

Figure 1.12: Point-contact conductance as a function of gate voltage. Image taken from Ref. [30].

that the confinement is a hard wall potential, $E_n = \frac{\hbar^2 n^2 \pi^2}{2m^* W^2}$ where W is the QPC width and $n = 1, 2, 3 \ldots$. These energies define the onsets above which the mode becomes conductive. We call $T_n(E)$ the transmission of each mode with energy E. Since in linear response the functions are evaluated at the Fermi energy, the conductance for a QPC, like in the case of a quantum dot, can be calculated from Eq. (1.45):

$$G = 2\frac{e^2}{h}\sum_n T_n(E_F) \ . \tag{1.54}$$

If one assumes that each mode turns on when the electron's energy surpasses E_n and the transmission for each mode is 1, then the conductance will jump in steps of $2e^2/h$ (see Fig. 1.12 for a theoretical simulation).

1.3.4 Transport in graphene

Let us now discuss the transport properties of a homogeneous monolayer graphene system of length L and width W.

1.3.4.1 Chirality in graphene

The graphene Hamiltonian near the Dirac points K and K' satisfy $H_{K'} = H_K^T$. Since the two Hamiltonians are proportional to $\vec{\sigma} \cdot \vec{q}$, Eq. (1.13), the resulting dispersion relation for both valleys is linear and isotropic. In this case, we can discuss the helicity or chirality produced from this relation [31]. The helicity is the projection of the pseudospin

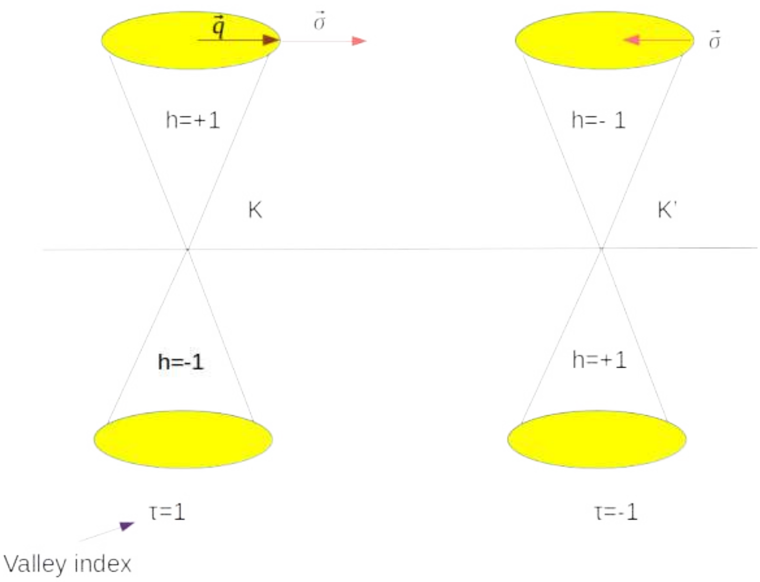

Figure 1.13: Schematic representation of chirality in graphene for two valleys K and K'.

(sublattice) on the wave vector $\vec{q}$. Specifically, the chirality operator is introduced as:

$$h_c = \vec{\sigma} \cdot \frac{\vec{q}}{\mid \vec{q} \mid}. \tag{1.55}$$

The eigenvalues of this operator are $h_c \rightarrow +1$ and $h_c \rightarrow -1$. If $h_c = -1$ the pseudospin and $\vec{q}$ are aligned but in opposite directions. If $h_c \rightarrow +1$ the two will be parallel and aligned along the same direction. Since h_c commutes with the Hamiltonian, in monolayer graphene the electronic states are chiral, as should be for massless Dirac fermions. A consequence is that chirality is reversed when moving from K to K' (see Fig. 1.13). In transport, this nicely implies that backscattering is forbidden if intervalley scattering is absent.

1.3.4.2 Transmission coefficient and conductance

For a common metal, the conductance is zero when the density of carriers becomes zero. However, in the case of Dirac carriers present in graphene the conductance is not zero despite the fact that graphene is a semimetal. We consider a sample of graphene in the xy plane without disorder and connected to two contacts made of doped graphene to which

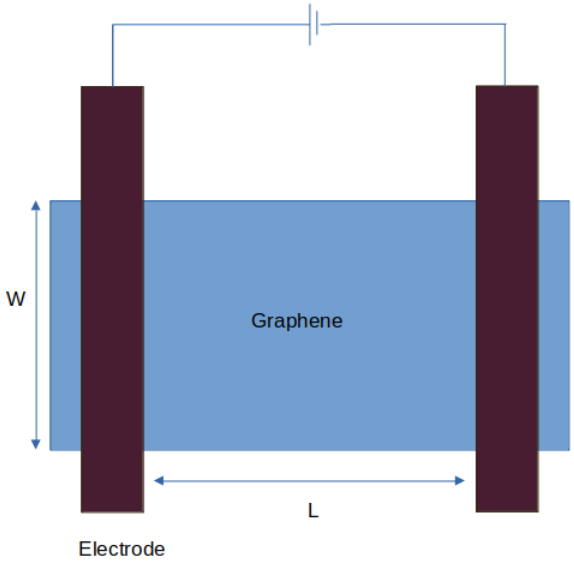

Figure 1.14: Sketch of a graphene strip with L the distance between the two electrodes and W the width of the strip.

we apply a potential bias V (see Fig. 1.14).

According to the Landauer picture (see Sec. 1.3.1), we can consider the transport of electrons in graphene as the transmission of electronic waves. From Eq. (1.41) the electric current carried by electrons is given by

$$I = \frac{2e}{h} \sum_{q} \int_{-\infty}^{+\infty} T(E,q)\ [f_L(E) - f_R(E)]\ dE. \tag{1.56}$$

We assume that the sample is wide and therefore the sum over transverse modes can be transformed into a integral in the continuum limit:

$$\sum_{q} \rightarrow \frac{W}{2\pi} \int_{-\infty}^{+\infty} dq. \tag{1.57}$$

where $q = N(E)\sin(\theta)$ is the transverse momentum, $N(E) = \frac{E}{\hbar v_F}$ is the momentum magnitude and $\tan(\theta) = \frac{q_x}{q_y}$ is the wave vector angle. Therefore, the current in graphene for each valley is

$$I = \frac{2eW}{\pi h} \int_{0}^{\pi/2} \cos\theta\ d\theta \int_{-\infty}^{+\infty} T(E,\theta)\ N(E)\ [f_L(E) - f_R(E)]\ dE. \tag{1.58}$$

Since we have valley degeneracy in graphene, the total current should be multiplied by 2:

$I \to 2I$. To calculate the linear conductance we make a Taylor expansion of Eq. (1.58) up to the first order in V and consider the zero temperature limit. Hence, we find [32]

$$G = G_0 \int_0^{\pi/2} T(E_F, \theta) \cos\theta \, d\theta. \tag{1.59}$$

Here, $G_0 = 2e^2 W N_F / \pi h = 4e^2 W E_F / h^2 v_F$ is the maximum conductance of an ideal graphene layer with a continuous distribution of modes. The transmission is evaluated at the Fermi energy and depends on the wave vector angle. If the tranmission is 1 independently of θ, we trivially obtain $G = G_0$.

1.4 Berry Phase in graphene

In classical and quantum mechanics, the Berry phase is the phase appearing in systems that undergo slow evolution. The phase is defined when the quantum system's Hamiltonian performs a loop in its parameter space. The phenomenon was independently discovered by T. Kato (1950) [33], S. Pancharatnam (1956) [34], and H. C. Longuet-Higgins and later generalized by Sir Michael Berry (1984) [35].

The Berry phase in graphene can be calculated taking the two-band Hamiltonian Eq. (1.10) as a reminder:

$$H = \hbar v_F \begin{bmatrix} 0 & p_x - ip_y \\ p_x + ip_y & 0 \end{bmatrix}.$$

with $\vec{p} = (p_x, p_y) = \hbar \, \vec{q}$ the momentum operator. The obtained eigenstates of the Hamiltonian with (A, B) the two graphene sublattice atoms are:

$$\Psi = \begin{bmatrix} \Psi_A \\ \Psi_B \end{bmatrix} = \frac{1}{\sqrt{2}} \begin{bmatrix} 1 \\ \pm e^{i\phi} \end{bmatrix}, \tag{1.60}$$

where ϕ is the polar angle of the momentum $\vec{q}$ and $q_x = q\cos\phi$ and $q_y = q\sin\phi$.

From Eq. (1.13) we obtain:

$$E(q) = \pm\hbar v_F |q|, \tag{1.61}$$

From Eq. (1.60), the Berry phase is the phase that the obtained eigenstate acquires when the momentum evolves on a complete circle at constant energy around a Dirac point [36]. The Berry phase can then be calculated as [35, 36]:

$$\Phi_{\text{Berry}} = \oint_C A_{(q)}\, dq, \tag{1.62}$$

with $A(q) = -i < \Psi|\partial_q|\Psi >$ is the Berry connection, which is related to the parallel transport of the eigenstates along the parameter space.

In monolayer graphene the pseudospin rotates by 2π and the Berry connection is then [37],

$$A(q) = \frac{-i}{2}\begin{bmatrix} 1 & e^{-i\phi} \end{bmatrix} \cdot \frac{\partial}{\partial q}\begin{bmatrix} 1 \\ e^{i\phi} \end{bmatrix}. \tag{1.63}$$

Thus,

$$A(q) = \frac{-i}{2}\begin{bmatrix} 1 & e^{-i\phi} \end{bmatrix} \cdot \begin{bmatrix} 0 \\ ie^{i\phi}\frac{\partial \phi}{\partial q} \end{bmatrix} = \frac{1}{2}\frac{\partial \phi}{\partial q} \tag{1.64}$$

The obtained Berry phase is then:

$$\Phi_{\text{Berry}} = \int_0^{2\pi} d\phi \frac{1}{2} = \frac{1}{2}\left[\phi\right]_0^{2\pi} = \pi \tag{1.65}$$

As a consequence, the Berry phase of monolayer graphene is π. As we already discussed, bilayer graphene has two sheets of graphene. The pseudospin in that case rotates by 4π. Thus the Berry phase in bilayer graphene is 2π [37].

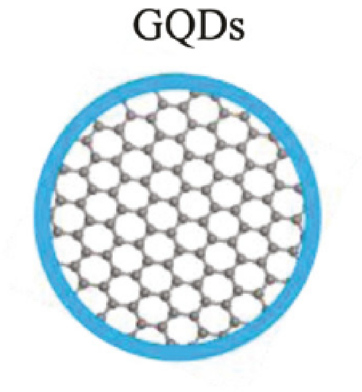

Figure 1.15: Graphene quantum dot realized by etching

1.5 Experimental overview

This thesis examines the confined states in various quantum systems, focusing on the cases of trivial and topological confinement. Wire and circular (rings and dots) structures are used as examples. In this section, we will go over the experimental overview of several recent projects by experimental groups on graphene, bilayer graphene quantum dots, and kink devices (kink states hosts).

1.5.1 Monolayer graphene quantum dot

Due to the distinctive structure-related features of (GQDs), including optical, electrical, and optoelectrical capabilities, these materials have received a lot of attention recently. The intrinsic inert carbon feature of graphene quantum dots makes them a novel type of (QD), as they are chemically and physically stable [38].

It will be impossible to utilize potential gate techniques, widely known for semiconductor quantum dots, to fabricate graphene QDs. Because if we want to apply a potential to the two sublattice atoms in graphene and since the distance between these atoms is very small, methods like lithographic surface alteration are not feasible. Another method discovered for this realization is by etching graphene into tiny flakes which are solids that resemble disks and have a fixed size (see Fig. 1.15). A problem that arises in this device

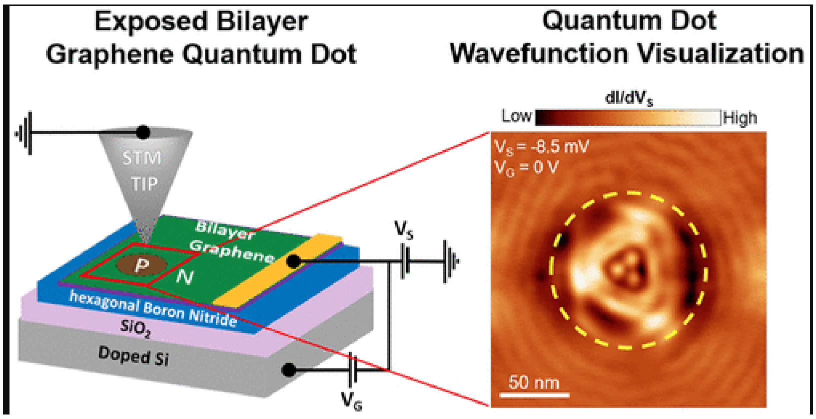

Figure 1.16: Bilayer graphene quantum dot experimental setup from Ref. [39]

is that this type of quantum dot shows edge disorder.

1.5.2 Bilayer graphene quantum dots

Bilayer graphene has a configurable energy gap due to the application of an electric field, which offers a novel method for building nanostructures like quantum dots. This type of dot allows for fine-tuning of the confinement as shown theoretically in this thesis (see Chaps. 4, 5), which eliminates both edge and substrate disorder by adjusting the gate profile potential.

Figure. 1.16 shows the experimental setup of bilayer graphene quantum dot realized by the group of Ref. [39], in which they report direct visualization of BLG QDs states by using a scanning tunneling microscope.

The development of electrostatically defined bilayer graphene (BLG) quantum point contacts, quantum dots, and double quantum dots was made possible by improvements in ultraclean van der Waals heterostructures, particularly the utilization of local graphite gates. Banszerus et al. [40] have presented a device that is made of two hexagonal boron nitride (hBN) crystals and a BLG flake that was mechanically exfoliated and picked up using a dry van der Waals process. As a back gate, the heterostructure is mounted on a graphite flake; for more detail about the fabrication setup see Ref. [40]. By using a finite bias applied to the bilayer graphene quantum dot they confine the electrons and calculate the conductance. Different experimental groups have succesfully fabricated such devices

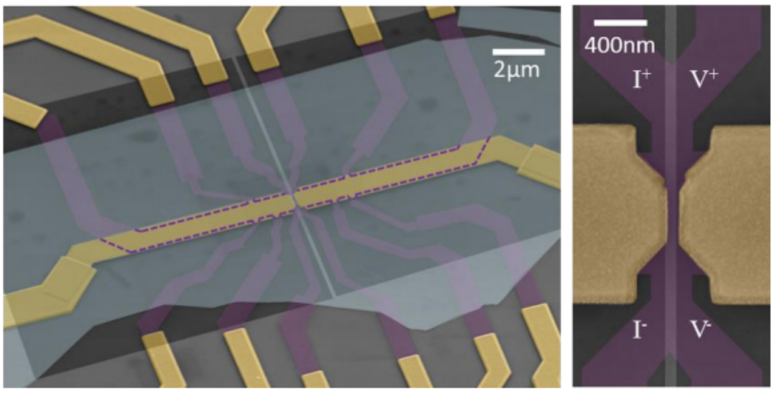

Figure 1.17: Bilayer graphene kink-states experimental device. Figure from Ref. [44]

for bilayer quantum dots such as Refs. [41–43]

1.5.3 Experimental realization of a valleytronic device

The motivation and the aim of this thesis is the study of kink states, the topological states under kink potential for valleytronic application. The first valleytronic experimental device which hosts kink state has been realized by Jing Li et al. [44] in which they describe how to make a dual-split-gate structure in bilayer graphene and provide experimental proof of valley-polarized kink states.

The experiment of [44] was inspired by the theoretical work of Martin et al. [8] which is experimentally challenging, where the four split gates must be perfectly matched and aligned, which is not easy in lithography.

For this purpose, they develop strategies to get through these barriers and provide proof of the kink states' ballistic conduction. They create the device by stacking h-BN, BLG and h-BN atop multi-layer graphene split bottom gates supported on a SiO2/doped Si substrate. They show the experimentally obtained results once the device fabricated and characterized (see Fig.1.17, 1.18). The device's kink states were seen experimentally by measuring the junction conductance as a function of the silicon back-gate voltage, as shown in Fig.1.18. They discovered that when the Fermi energy is outside the bulk bandgap, the conductance is high. The conductance increases in the (+-) configuration

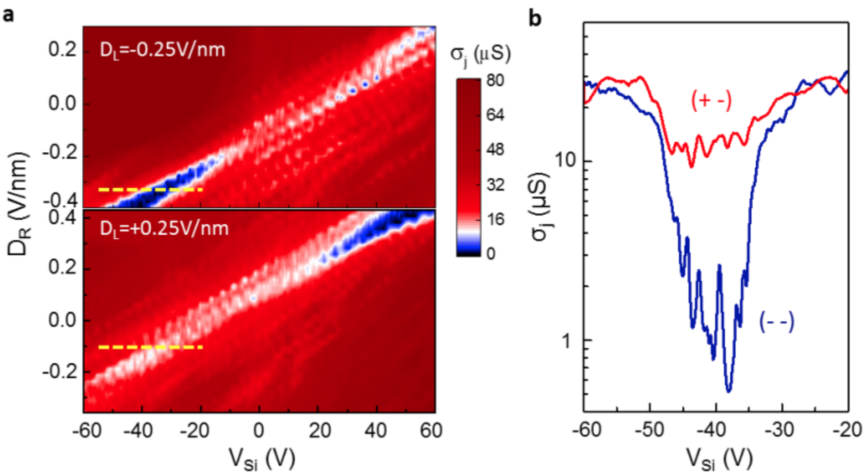

Figure 1.18: (a) The junction conductance as a function of the potential V in the fabricated device at fixed deplacement field. (b) Conductance as a function of the potential along the yellow dashed lines. Figure from Ref. [44]

and falls in the (- -) configuration for Fermi energy inside the band gap, showing the presence of extra conducting channels. The experimental design and findings are consistent with Martin et al. prediction that kink states occurs (see the paper for more details [44]). This serves as a solid starting point for future study in valleytronics.

Another publication by Mania et al Ref. [45] describes an additional experiment and a fabricated device that hosts the kink states at curved boundaries of folded bilayer graphene. They demonstrate long-range ballistic transport at such topological channels with the four terminal resistance being near zero and the two terminal resistance being close to the ballistic resistance at zero magnetic fields.

In order to build the valleytronic device, Mania and colleagues sandwiched folded bilayer graphene between two crystals of boron nitride (hBN). As a consequence of this device and by the application of the gate potential with a potential changing its signs to two sheets of graphene, the inversion symmetry is broken.

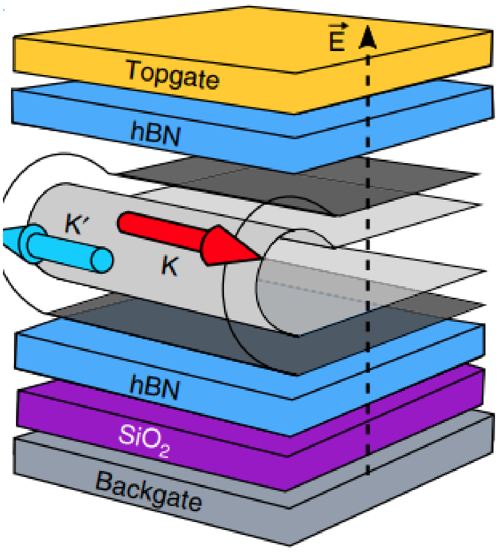

Figure 1.19: Bilayer graphene valleytronic device. Figure from Ref. [45]

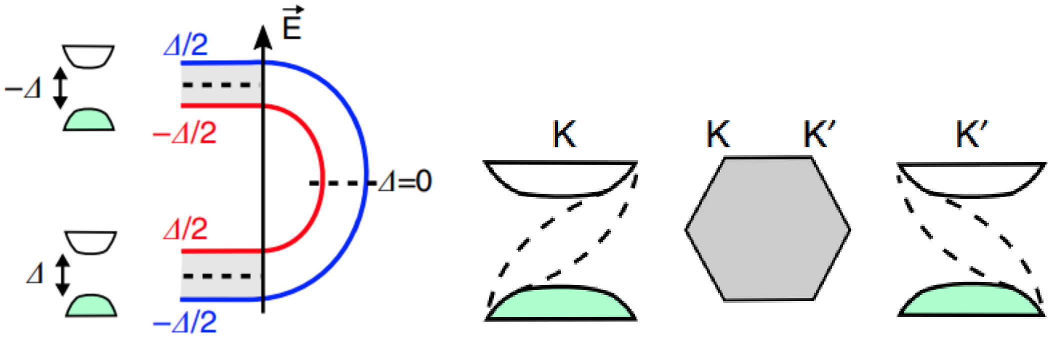

Figure 1.20: Potential applied to the two sheets and the creation of the kink states inside the gap. Figure from Ref. [45]

The curved boundary of the folded bilayer graphene in this case transforms into a domain wall [45] and the kink states created in the middle of the gap (see Fig.1.20) as expected from the theoretical work of Martin et al [8].

Direct imaging of topological edge states at the bilayer graphene domain wall was also presented experimentally by the group of Yin et al [46], where they observe the topological states at the bilayer graphene domain wall using a scanning tunneling microscope. In an ultrahigh vacuum chamber, they set up the sample and perform the scanning tunneling and spectroscopic measurements. Their research shows that one-dimensional topological

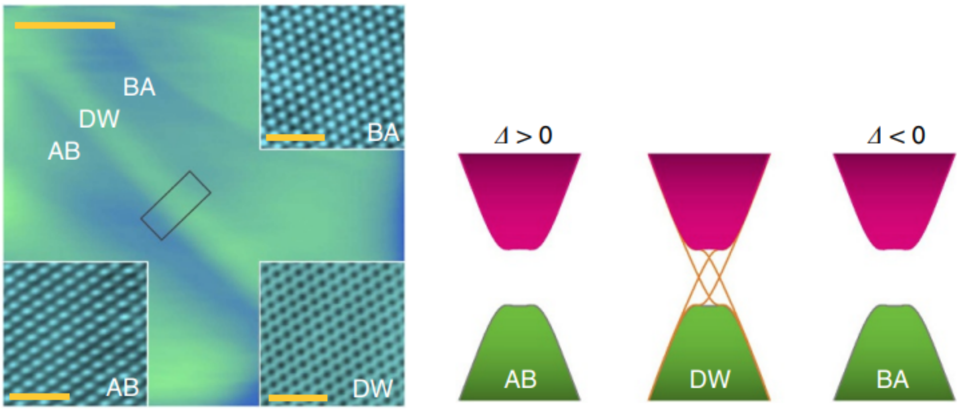

Figure 1.21: Topological states occurs in the middle of the gap in the domain wall. Figure from Ref. [46].

systems can maintain their stability even in the presence of strong magnetic fields.

All those experiments have achieved and explored kink states in the wire case for bilayer graphene. They give hope that in the future, other experimental groups may create a valleytronic device employing bilayer graphene quantum dots or rings as mentioned theoretically in this thesis.

1.6 Conclusion

To summarize, graphene is a two-dimensional material hosting massless Dirac electrons and a linear dispersion at low energies. This dispersion changes if another layer is added as in bilayer graphene, leading to a parabolic spectrum and massive fermions. This is the starting point to studying electronic transport phenomena when graphene is subjected to an external field like a magnetic or electric field.

In this chapter, we have discussed background material about monolayer and bilayer graphene such as their electronic properties as well as the Landau levels in both cases. The applied electric fields are homogeneous. In the next chapters, we will consider inhomogeneous potentials that can even change their sign, leading to electronic confinement as we have discussed here for quantum point contacts and quantum dots.

Additionally, we have briefly discussed the generalities of electronic quantum transport in the ballistic regime. A most suitable framework, in this case, is the Landauer-Büttiker model, which expresses the conductance in terms of transmission probabilities. We will extensively make use of this formalism in the remainder of this thesis when we calculate the current in bilayer graphene constrictions and loops.

Chapter 2

Confinement in bilayer graphene electrostatic wires

This thesis studies the electrostatic confinement of charge carriers in bilayer graphene structures in different geometries and conditions. Particularly, this chapter discusses two possible general cases of such confinement in a translationally invariant wire geometry. The first case corresponds to so-called *trivial confinement*, described in Sec. 2.1, in which the system sprectrum of eigenstates always shows a gap around zero energy. The second case is the nontrivial or, as we call it, *topological confinement*, where in-gap zero-energy states can be present, with two types of potential profiles: single kink and double kink (or kink-antikink). They are described in Secs. 2.1 and 2.2, respectively, where we identify characteristic features in the corresponding spectra.

2.1 Trivial confinement

An easy way of opening a gap for confined charge carriers in the bilayer graphene system is by applying an electric field across the two sheets of graphene [47–49]. This is sketched in Fig. 2.1, where we have the two bilayer graphene (BLG) sheets under conditions representing a wire along x on the xy plane. The colored microelectrodes on top and bottom of the two graphene sheets are creating the mentioned electric field by means

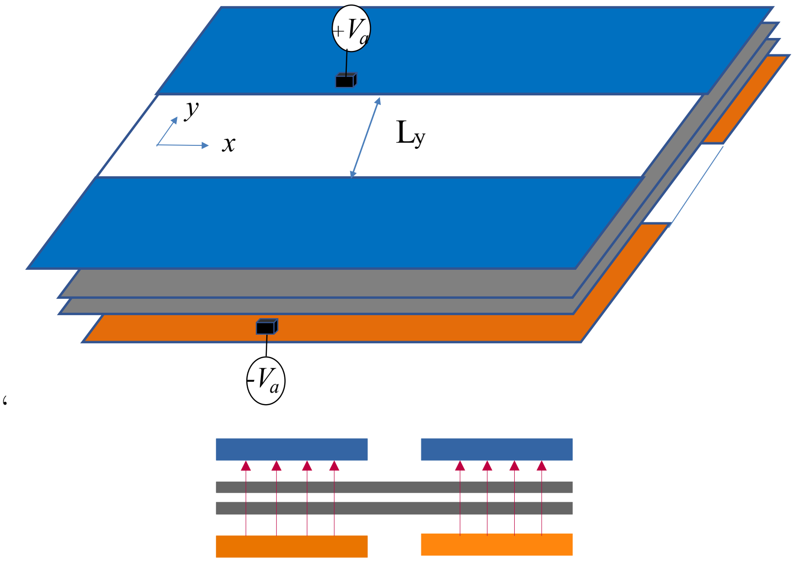

Figure 2.1: Sketch representing an electrostatic BLG wire created by gated top and bottom microelectrodes. Blue and orange are indicate applied potentials of opposite signs. The white region describes the unbiased zone representing the electrostatic wire. The small sketch is a side view showing the electric field which is always in parallel (upwards) direction.

of the applied biases V_a and $-V_a$, indicated by the blue and orange colors, respectively. As shown in the lower inset, the electric field is pointing upwards for $y < -L_y/2$ and $y > L_y/2$, while the field vanishes in the central region of width L_y where $V_a = 0$. When we apply a positive voltage to the top electrodes and a negative voltage to the bottom electrodes, a voltage difference between the layers of bilayer graphene is created. Such potential difference causes an opening of the local gap underneath the electrodes. As a consequence, the electrons are confined to the white region with a vanishing local gap. We refer to this type of confinement as trivial confinement. Its main characteristic is the exclusion of the electrons from the wire sides by the vertical electric field. Notice that the electrostatic confinement is smooth on the atomic scale and the effective wire borders are very far from the physical borders of the graphene sheets. In electrostatic confinement we can disregard any dependence on the type of specific atomic arrangements at the physical edges of the graphene sheets, like armchair edge or zigzag edge.

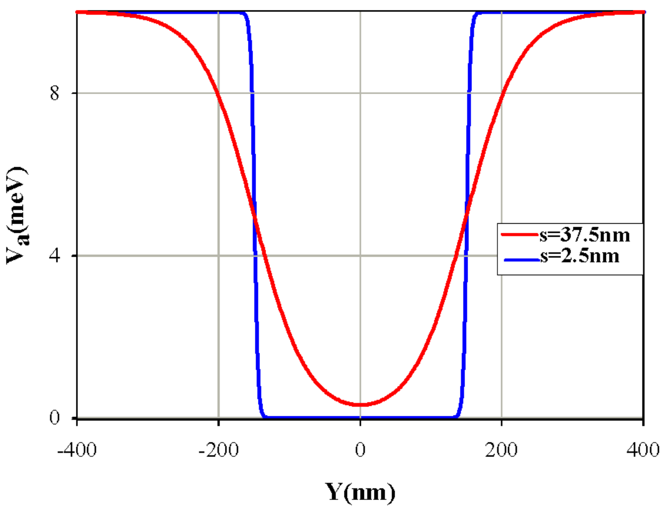

Figure 2.2: Parameterized asymmetric potential profile as a function of y for two values of the diffusivity parameter s.

2.1.1 Effective Hamiltonian

We are interested in the low energy sector near the two Dirac points for the two valleys K and K'. This section presents the details of our low-energy description applied to electrostatic BLG wires in a Dirac-like continuum approach.

2.1.1.1 Model

The effective Hamiltonian extends Eq. (1.16) to the case of magnetic and inhomogenous electric potentials.

$$H = v_F \left(p_x - \frac{y}{l_z^2} \right) \sigma_x \tau_z + v_F p_y \sigma_y + t(\lambda_+ \sigma_- + \lambda_- \sigma_+) + V_s + V_a(y)\lambda_z \, , \tag{2.1}$$

with the three pseudospins characteristic of bilayer graphene are described by Pauli matrices. As explained in Sec. 1.2.2 we use different symbols for valley $\tau_{x,y,z}$, sublattice $\sigma_{x,y,z}$ and layer $\lambda_{x,y,z}$ Pauli matrices, where $\lambda_\pm = (\lambda_x \pm i\lambda_y)/2$ and analogous definitions for $\sigma_\pm$. The parameters in Eq. (2.1) are v_F, t, l_z, while V_s and V_a are the symmetric and asymmetric potentials, respectively. Parameters v_F and t are intrinsic of BLG (see Sec. 1.2.2), and l_z is the magnetic length is defined by $l_z^{-2} = eB/\hbar c$ representing a magnetic field in z

direction. We assume a vanishing symmetric potential $V_s = 0$, and a y-dependent asymmetric potential $V_a(y)$, acting on the two layers as created by the gated microelectrodes (Fig. 2.1).

The continuum model includes the asymmetric potential $V_a(y)$. We assume a parameterized $V_a(y)$ with the shape of a channel, increasing on both sides along y, defining an effective electronic confinement channel. We have to bear in mind, however, that the spectrum of Hamiltonian eigenvalues is not bounded either from below or above. More specifically, the potential reads

$$V_a(y) = V_a^{(0)} \frac{1}{1 + e^{\frac{y-y_1}{s}}} + V_a^{(0)} \left(1 - \frac{1}{1 + e^{\frac{y-y_2}{s}}}\right), \tag{2.2}$$

where $y_1 = -y_2 = -L_y/2$ are the position of the electrostatic wire edges, $V_a^{(0)}$ is the asymmetric potential to the left ($y < y_1$) and right ($y > y_2$) of the wire and s is a diffusivity length modelling the smoothness of the transition from one to zero of the Fermi-like function.

Figure 2.2 shows the $V_a(y)$ potential profile in the cases of a sharp ($s = 2.5$ nm) and a smooth ($s = 37.5$ nm) potential. In the results discussed below we have used the latter value,(the smooth profile), because it seems to be a more realistic value when compared to experiments [50, 51].

2.1.2 Band structure

The energy bands of the system can be numerically obtained by solving for the Hamiltonian eigenvalues assuming a specific potential with a transverse dependence $V_a(y)$. Figure 2.3(a) shows the energy spectrum of a trivial BLG electrostatic wire as a function of the momentum k by applying a potential bias with $V_a^{(0)} = 10$ meV in Eq. (2.2). As could be anticipated for a trivial system, the spectrum shows a gap around zero energy. To see the spatial distribution of the states, we plot in Fig. 2.3(b) the density distribution of the lowest state at a given k as a function of y. We observe that the state is indeed confined and localized around $y = 0$.

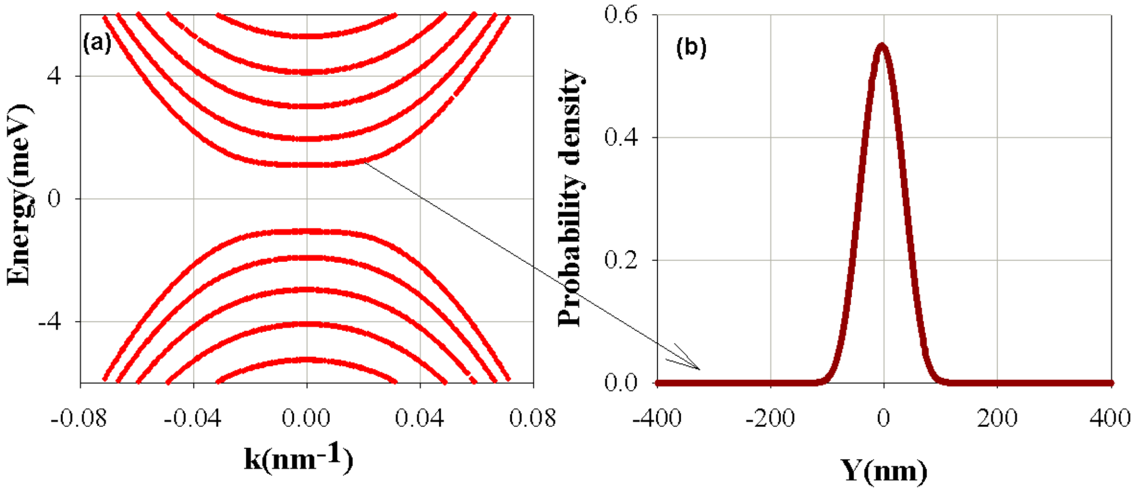

Figure 2.3: a): Band structure of a trivial BLG wire with a value of potential $V_a^{(0)} = 10$ meV and the transverse width $L_y = 150$ nm b) Probability density distribution of a selected k state indicated with an arrow.

2.1.3 Magnetic field dependence

Next, we consider the effect of an external magnetic field perpendicular to the BLG sheets, of constant modulus $B = 78$ mT. We plot the energy spectrum as a function of the momentum in Fig. 2.4a, the spectrum showing a qualitative difference with the preceding zero-field results. We observe that the magnetic field has the ability to break the valley degeneracy, with blue lines referring to valley K and red lines to valley K'.

For a given valley and a given momentum we plot the energy spectrum as a function of magnetic field in Fig. 2.4(b). In agreement with Sec. 1.2.3, where the magnetic field dependence of BLG levels were discussed, we see that the wire spectrum shows bunching of levels as a function of magnetic field. The plot shows that the spectrum is characterized by the emergence of discrete Landau levels. It can be seen in Fig. 2.4(b) the emergence of a two-fold degenerate Landau level close to zero energy, as well as linearly-dispersing Landau levels at higher positive and negative energies. The BLG wire eigenenergies merge

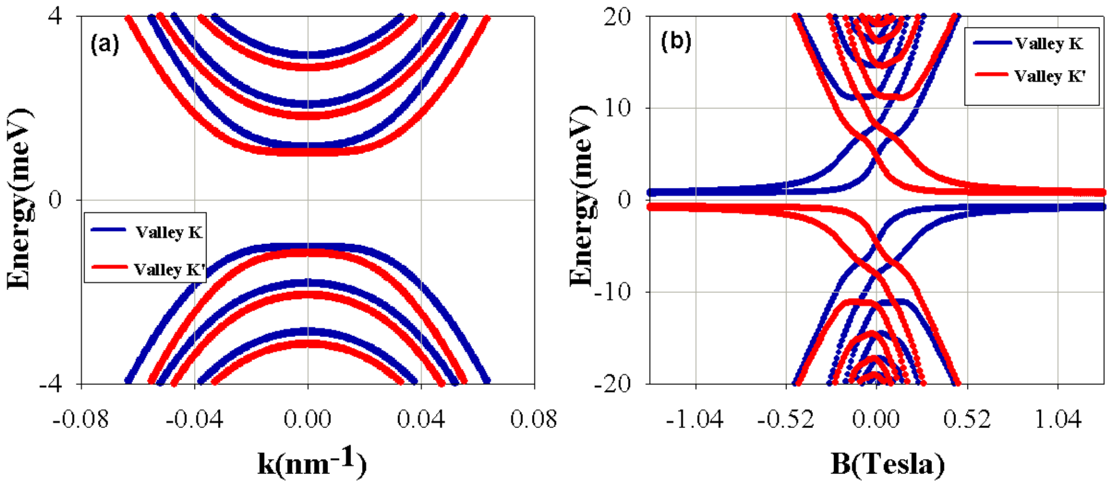

Figure 2.4: a) Band structure of an electrostatic BLG wire in a magnetic field $B = 78$ mT. Different colors are used for the two valleys. b) Energy spectrum as a function of magnetic field at a fixed $k = 0.004$ nm^{-1}.

into Landau levels, discussed in Chap. 1, with precise values

$$\begin{cases} E_l = 0, & l = 0, 1 \\ E_{l\pm} = \pm\hbar\omega_c\sqrt{l(l-1)}\,, & l = 2, 3, \ldots \end{cases} \tag{2.3}$$

with $\omega_c = eB/m^*$ and $m^* = t/2v_F^2 = 0.03m_e$.

2.1.4 Width effect on the energy spectrum

The width L_y of the unbiased region $V_a = 0$ (white color in Fig. 2.1) affects the spectrum details. We study two cases: the first one when $L_y = 150$ nm and the second case when $L_y = 300$ nm. Figure 2.5 shows that when L_y increases the spectrum zero-energy gap rapidly reduces, eventually approaching the gapless 2D limit (Fig. 2.5b). Reversedly, a small L_y yields a larger zero-energy gap as shown in Fig. 2.5a.

The trivial character of Fig. 2.5 spectra, from the point of view of topology classification, corresponds to the observation that no energy branch is ever crossing zero energy, such that band curvatures are always opposite in the upper and lower energy semiplanes.

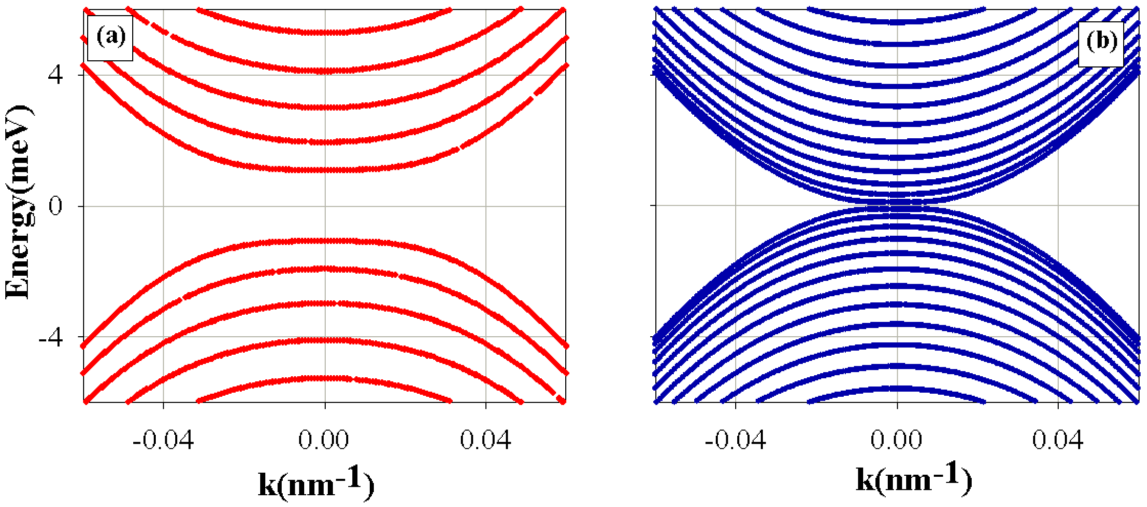

Figure 2.5: Band structure of electrostatic BLG wire with value of potential $V_a = 10$ meV and widths: a) $L_y = 150$ nm, b) $L_y = 300$ nm.

In a sense, there is no band inversion and the two sectors are disconnected. We will study next a situation where such behavior no longer holds, band inversion is present and, therefore, the topology classification is qualitatively different.

2.2 Topological confinement

This Section discusses a qualitatively different type of electrostatic confinement, when the microlectrodes on the same side of the BLG planes take values of different signs, i.e., such that domain walls separating regions of different signs emerge (see Fig. 2.6). Particularly, we will investigate two cases of this type of confinement: a) a so-called single kink, corresponding to a straight-line domain wall, which is an alternative way to create one dimensional localized states in bilayer graphene; b) a double kink which is just the case when we take into account two parallel kinks where the sign inversions of the two kinks occur in reverse order along y. The double kink is also known as a kink-antikink system.

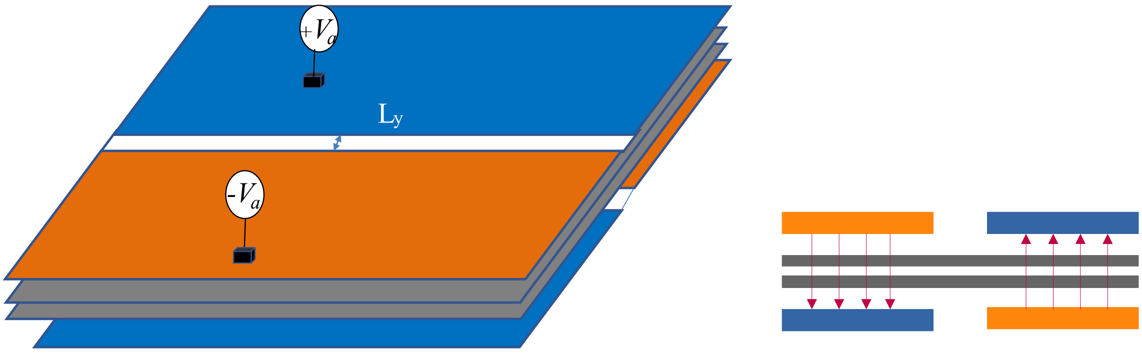

Figure 2.6: Sketch representing the bilayer graphene under kink potential [8].

2.2.1 Single kink potential profile

In this type of confinement, as represented in Fig. 2.6, we have the two sheets of BLG (gray) where the microelectrodes on the two sides of bilayer graphene (blue and orange) in the top and in the bottom are separated by a small width $L_y \approx 0$. The potentials of the microelectrodes change their sign (V_a and $-V_a$) in the xy plane. We also consider the role of an electric field in perpendicular direction to the graphene planes.

The spatial degrees of freedom are x (longitudinal) and y (transverse) and confinement along the line (white) is due to the difference in sign of potential. In the kink configuration, a one dimension localized states in bilayer graphene are around the line of potential inversion, and the term kink is used for the area in the boundary of the potential changing sign from $+$ to $-$, or from $-$ to $+$.

The topological type of confinement has been discussed in 2007 by Martin, Blanter and Morpurgo (MBM) in Ref. [8] also by other authors [52] [53], where they investigate the properties of the localized states propagating along the kink potential and also in a double kink. Those states have a predominant one dimensional and topological character. In a matrix representation of Eq. (2.1), the low energy bilayer Hamiltonian for the system, in one valley K, is:

$$H = \begin{bmatrix} -\frac{V_a}{2} & v_F\pi^+ & 0 & 0 \\ v_F\pi & -\frac{V_a}{2} & t & 0 \\ 0 & t & \frac{V_a}{2} & v_F\pi^+ \\ 0 & 0 & v_F\pi & \frac{V_a}{2} \end{bmatrix}, \tag{2.4}$$

with $\pi = p_x + ip_y$ and $\pi^+ = p_x - ip_y$. For the moment, we consider the case when magnetic field $B = 0$ ($l_z \to \infty$). MBM in their paper used a two-band simplified and reduced Hamiltonian which in the literature is used to describe the bilayer graphene in a simpler way. This Hamiltonian is valid at low energy range ($|E| \ll t/4$) and can be obtained from the 4 by 4 Hamiltonian H given by Eq. (2.4) by a further reduction as detailed in [8] (setting $\hbar \equiv 1$)

$$H = \begin{bmatrix} -\frac{V_a}{2} & v_F\pi^+ & 0 & 0 \\ v_F\pi & -\frac{V_a}{2} & t & 0 \\ 0 & t & \frac{V_a}{2} & v_F\pi^+ \\ 0 & 0 & v_F\pi & \frac{V_a}{2} \end{bmatrix} \to \begin{bmatrix} H_{11} & H_{12} \\ H_{21} & H_{22} \end{bmatrix}. \tag{2.5}$$

To find the reduced effective hamiltonian we consider [54]

$$H_{\text{reduced}} = H_{11} - H_{12}\, H_{22}^{-1}\, H_{21}. \tag{2.6}$$

After diagonalization and with $V_a \ll t$ the reduced Hamiltonian becomes

$$H = - \begin{bmatrix} -\frac{V_a}{2}(1 - \frac{v_F^2 P^2}{t^2}) & -\frac{v_F^2 \pi\dagger^2}{t} \\ -\frac{v_F^2 \pi^2}{t} & \frac{V_a}{2}(1 - \frac{v_F^2 P^2}{t^2}) \end{bmatrix}, \tag{2.7}$$

with $P = \sqrt{p_x^2 + p_y^2}$. The dispersion relation for the spectrum is then

$$E^2 = \frac{V_a^2}{4}\left(1 - \frac{v_F^2 P^2}{t^2}\right)^2 + \frac{v_F^4 P^4}{t^2}\ . \tag{2.8}$$

When we apply an electric field, a gap opens in the spectrum and $v_F P \approx V_a/2$. If $V_a < t$ we neglect P^2 in the first term, and Eq. (2.8) becomes:

$$E^2 = \frac{V^2}{4} + \frac{v_F^4 P^4}{t^2}. \tag{2.9}$$

The eigenstates of the obtained Hamiltonian are two-component spinors $\Psi(x,y) = [\Psi_a(x,y), \Psi_b(x,y)]^T$. In Ref. [8], the momentum along the y direction is conserved and therefore the wavefunction is

$$\Psi(x,y) = \exp(ip_y y) \begin{bmatrix} \varphi_a(x) \\ \varphi_b(x) \end{bmatrix} , \tag{2.10}$$

with p_y the wave vector along y direction. After diagonalization of the dimensionless Hamiltonian the wave equation components have to fulfill two equations

$$-M(x)\varphi_a + (\partial_x + p_y)^2 \varphi_b = \epsilon \varphi_a, \tag{2.11}$$

$$-M(x)\varphi_b + (\partial_x + p_y)^2 \varphi_a = \epsilon \varphi_b, \tag{2.12}$$

where $M(x)$ is defined as $M(x) = V_a \ t \ a^2/2v_F^2$, with a the lattice constant.

Those two equations are not easily analytically solvable for an arbitrary potential profile. MBM consider first the case of single kink where $M(x) = M \ \mathrm{sign}(x)$ (sharp kink). By applying the matching conditions at the kink MBM are able to obtain a homogeneous system with four equations. From its determinant we need to solve the following equation

$$4\alpha^2(\alpha^2 + \beta^2) + 4p_y M\alpha - M^2 = 0, \tag{2.13}$$

with $\alpha(\beta) = 2^{-1/2}[(p_y^4 + M^2 - \epsilon^2)^{1/2} + (-p_y)^2]^{1/2}$. This equation has a solution near zero only if $p_y < 0$ and $M > 0$ The obtained dispersion is

$$p_y = \frac{-\epsilon \pm M/\sqrt{2}}{(\pm\epsilon + M\sqrt{2})^{1/2}} , \tag{2.14}$$

where we define the momentum and the energy of the two topological branches.

Our aim now is to perform a similar analysis for a kink using the four by four Hamiltonian for a given valley $\tau = \pm$. We intend to be rigorous or fundamental in our analysis in order to check whether the differences originate in the Hamiltonian reduction or not.

First step is to clarify the wave function continuity conditions. Assume a step kink given by:

$$V_a(y) = V_a \,\mathrm{sgn}(y)\ . \tag{2.15}$$

The wave function is then a 1D four-component function $\Phi_{\sigma\lambda}(y)$, where σ, $\lambda = \pm$. On general physical grounds we demand the wave function components to be continuous at the position of the kink. Its first derivative is discontinuous however. The discontinuity condition is determined from the eigenvalue equation $h_k\Psi = E\Psi$. We simply write the equation for $y = \epsilon$ and for $y = -\epsilon$ and subtract. Based on the continuity of the wave function components, only the p_y term and the V_a term will survive. This leads to a condition on the first derivative at the kink position. Notice that the usual treatment of integrating the eigenvalue equation as

$$\int_{-\epsilon}^{+\epsilon} H\,\Psi(y)dy = \int_{-\epsilon}^{+\epsilon} E\,\Psi(y)dy. \tag{2.16}$$

in our case leads to the trivial identity $0 = 0$ and, therefore, gives no relevant information. Summarizing, the conditions right at the kink position are

$$\begin{aligned} \Psi(0^+) - \Psi(0^-) &= 0\ , & (2.17)\\ \Psi^{'}(0^+) - \Psi^{'}(0^-) &= \frac{i\tau\, V_a}{\hbar v_F}\,\lambda_z\sigma_y\,\Psi(0)\ . & (2.18) \end{aligned}$$

Notice that Eqs. (2.17) and (2.18) are valid for each component of the wave function, i.e., they amount to a total of 8 equations. They are valid for a sharp interface kink.

Next, we characterize the wave function in each region of constant parameters, $y < 0$ and $y > 0$. With constant parameters the Hamiltonian is locally invariant by translation and we can introduce wavenumbers q such that the wave function can be expanded as:

$$\Psi_{\sigma\lambda}(y) = \sum_q C_q\, e^{iqy}\, \Phi^{(q)}_{\sigma\lambda}\ . \tag{2.19}$$

The q wavenumbers are complex, with a non-vanishing imaginary part, since the states decay for $y = \pm\infty$. The set of evanescent wave numbers and modes $q, \Phi^{(q)}_{\sigma\lambda}$ is obtained from the eigenvalue problem with H given by Eq. (2.1).

$$H\Phi = E\Phi\ . \tag{2.20}$$

We transform Eq. (2.20) from a Hermitian problem to a non-Hermitian q eigenvalue problem by multiplying both sides by $\sigma_x\tau_z$:

$$\left[iv_F\,\hbar k\,s_\tau\,\sigma_z + \frac{t}{2}(i\lambda_x\,\sigma_z - \lambda_y) \pm \frac{V_a}{2}\lambda_z\sigma_y + E\sigma_y\right]\Phi = v_F\,\hbar q\,\Phi\;. \tag{2.21}$$

Equation (2.21) is a linear eigenvalue problem of dimension 4 × 4. It yields 4 complex wavenumbers q_i from the diagonalization of the 4 × 4 matrix in each region (± signs in V_a are for $y > 0$ and $y < 0$, respectively).

The wave function has to be regular for $y \to \pm\infty$ and this excludes two $q's$ in Eq. (2.19) for each region (out of the 4 possible ones); i.e., those having $\mathrm{Im}(q) > 0$ for $y < 0$ and those with $\mathrm{Im}(q) < 0$ for $y > 0$ have to be excluded. They normally come in groups of 4 with different signs of the real and imaginary parts as $q = \pm q_r \pm iq_i$. We are thus left with two wave numbers on each side and, equivalently, 2 coefficients $C_q's$ for the wave function on each side. Let us assume

$$\text{for } y > 0,\;\; \Psi_{\sigma\lambda}(y) = C_1 e^{iq_1 y}\Phi^{(1)}_{\sigma\lambda} + C_2 e^{iq_2 y}\Phi^{(2)}_{\sigma\lambda}, \tag{2.22}$$

$$\text{for } y > 0,\;\; \Psi_{\sigma\lambda}(y) = C_3 e^{iq_3 y}\Phi^{(3)}_{\sigma\lambda} + C_4 e^{iq_4 y}\Phi^{(4)}_{\sigma\lambda}. \tag{2.23}$$

The linear system of Eqs. (2.17)-(2.18) now reads

$$\Phi^{(1)}_{\sigma\lambda}C_1 + \Phi^{(2)}_{\sigma\lambda}C_2 - \Phi^{(3)}_{\sigma\lambda}C_3 - \Phi^{(4)}_{\sigma\lambda}C_4 = 0. \tag{2.24}$$

Notice that imposing the wave function continuity with wave functions given by Eq. (2.19) on each y-side automatically guarantees that the condition on the derivative discontinuity Eq. (2.18) is also fulfilled. This is true because the chosen wave functions of Eq. (2.19) already fulfill Eq. (2.20) by construction when the proper complex wavenumbers $q's$ for a given energy E are used.

Equations (2.24) is a linear system of 4 equations (since $\sigma, \tau = \pm$) and 4 unknowns $\{C_i, i = 1-4\}$. The linear system is homogenous and, therefore, it always has the trivial solution of vanishing amplitudes $C_i = 0$. In addition, however, a nontrivial solution may exist at particular energies such that the determinant of the linear system vanishes.

These are the energies of the in-gap eigenstates we are interested in. In conclusion, we need to determine the linear system coefficients Φ's of Eq. (2.21) and then look for the determinant associated with Eq. (2.24).

We define the solutions for the equation (2.21) and call the set of solutions $\{q, \Phi^{(q)}_{\sigma\lambda}\}$ the complex band structure. It is a non-Hermitian eigenvalue problem for the q's and this explains why the wave numbers are in general complex. Equation (2.21) has some symmetries, namely:

i) Taking the complex conjugate of Eq. (2.21) we notice the solutions come in pairs

$$\{q, \Phi^{(q)}_{\sigma\lambda}\} \leftrightarrow \{q^*, \Phi^{(q)*}_{\sigma\lambda}\}. \tag{2.25}$$

ii) Using the symmetry transformation of Eq. (2.21) by $\lambda_x\sigma_x$ one can relate the solutions of V_a and $-V_a$ as

$$\{q, \Phi^{(q)}_{\sigma\lambda}\} \text{ with } V_a \Leftrightarrow \{q, \lambda_x\sigma_x\Phi^{(q)}_{\sigma\lambda}\} \text{ with } -V_a\ . \tag{2.26}$$

iii) As will be shown below, the q wavenumbers only depend on the square of the energy and kink potential, E^2 and V_a^2 .

iv) Using the symmetry transformation of Eq. (2.21) by τ_x one can relate the solutions of $s_\tau = +$ and $s_\tau = -$ as

$$\{q, \Phi^{(q)}_{\sigma\lambda}\} \text{ with } s_\tau = + \ \leftrightarrow\ \{q, \tau_x\Phi^{(q)}_{\sigma\lambda}\} \text{ with } s_\tau = -\ . \tag{2.27}$$

As already anticipated above, the symmetries imply that with a fixed E the set of $q's$ is the same on both sides of a sharp kink; i.e., four wavenumbers of type $q = \pm q_r \pm iq_i$. We use a matrix representation such the 4×4 matrices are split in bigger blocks for valley (λ) and in smaller blocks for sublattice (σ). For instance we have the following correspondence:

$$\lambda_x\sigma_z = \begin{bmatrix} 0 & 0 & 1 & 0 \\ 0 & 0 & 0 & -1 \\ 1 & 0 & 0 & 0 \\ 0 & -1 & 0 & 0 \end{bmatrix}. \tag{2.28}$$

In the above representation, the matrix M for Eq. (2.24) reads:

$$M = \begin{bmatrix} \alpha & \beta & it & 0 \\ -\beta & -\alpha & 0 & 0 \\ 0 & 0 & \alpha & -\gamma \\ 0 & -it & \gamma & -\alpha \end{bmatrix}, \qquad \text{where} \quad \begin{cases} \alpha = i\hbar k v_F s_\tau, \\ \beta = i(\frac{V_a}{2} - E), \\ \gamma = i(\frac{V_a}{2} + E). \end{cases} \tag{2.29}$$

The q wave numbers are given by the secular equation determinant:

$$\det(M - \hbar v_F\, q\, \mathbb{I}) = 0. \tag{2.30}$$

Expanding the determinant by the minors of the first column (for instance) it is straightforward to derive the analytic expression of the wave numbers:

$$\hbar v_F\, q = \pm\sqrt{\alpha^2 - \delta}, \quad \text{where} \quad \delta = \frac{\gamma^2 + \beta^2}{2} \pm \frac{1}{2}\sqrt{(\gamma^2 + \beta^2)^2 - 4(\beta^2\gamma^2 - \beta\gamma t^2)}. \tag{2.31}$$

We stress that Eq. (2.31) only depends on the parameter combinations

$$\beta^2 + \gamma^2 \;=\; -2\left[\left(\frac{V_a}{2}\right)^2 + E^2\right], \tag{2.32}$$

$$\gamma\beta \;=\; -\left[\left(\frac{V_a}{2}\right)^2 - E^2\right]. \tag{2.33}$$

This confirms the above-mentioned result that the wave numbers only depend of the squares of the energy E and antisymmetric potential V_a, i.e., they are not affected by the signs of these quantities. The complex wavenumbers are the same on both sides of a sharp kink where V_a just changes sign.

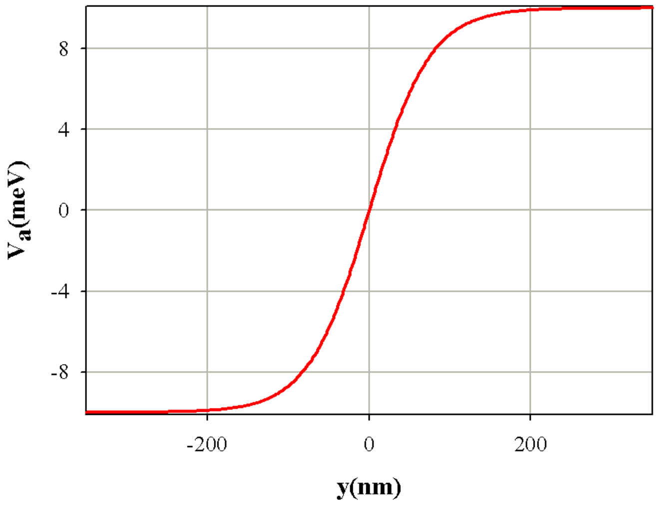

Figure 2.7: Smooth single kink potential representation.

2.2.1.1 Single kink numerical results

We calculate the energy spectrum for a single kink with a smooth potential see(Fig. 2.7). We find that the energy spectrum as a function of the momentum for each valley presents two branches crossing zero energy, in the region of the gap for the case of gated bilayer graphene.

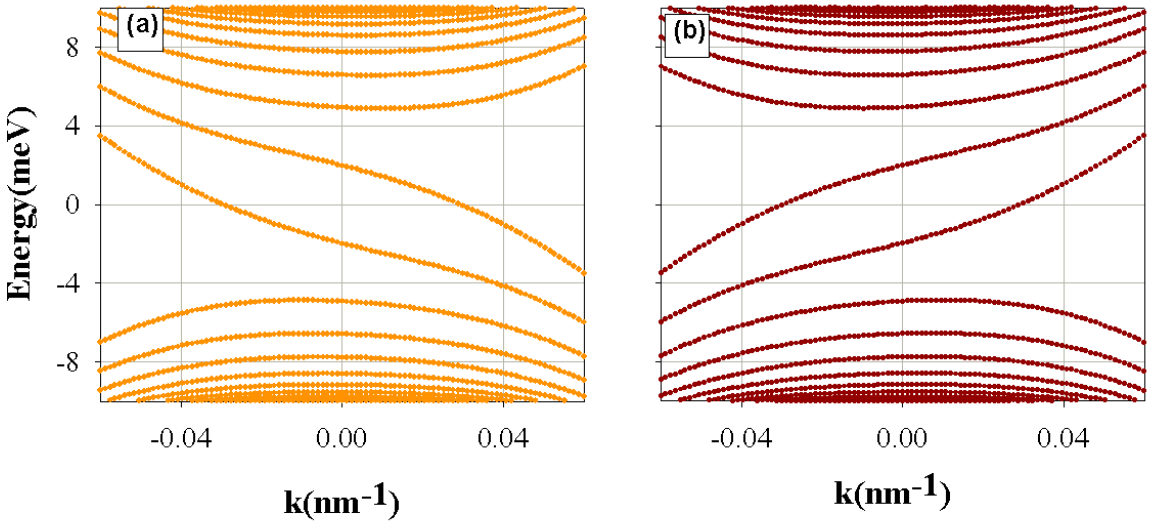

Figure 2.8: Bands of bilayer graphene kink for the two valleys: a) valley K and b) valley K' for a smooth potential $s = 12.5$ nm.

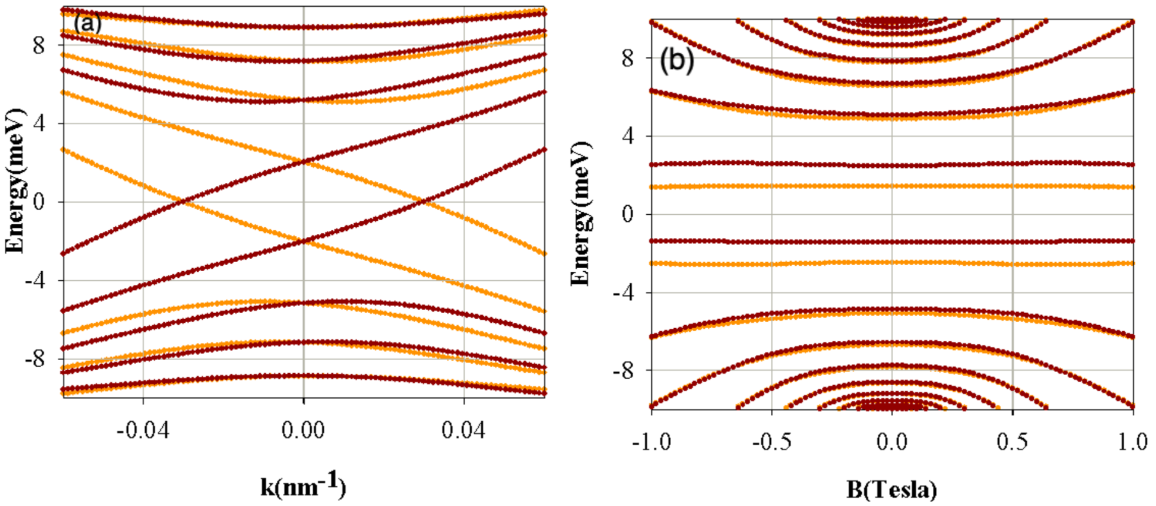

Figure 2.9: (a) Magnetic field dependence of the kink spectrum (K : orange, K': red) on the valleys at $B = 78$ mT, (b) Magnetic field dependence of energy at $k = 0.01$ nm^{-1}

Those states are propagated in opposite direction for each valley, confirming the valley momentum locking of the single kink. Figure 2.8 shows the energy spectrum as a function of momentum for each valley K and K'. We observe that two branches occur at the low energy in the middle of the gap and they propagate in opposite velocity for each valley.

2.2.1.2 Magnetic field dependence

The magnetic field dependence on the energy spectrum for bilayer graphene single kink at a fixed magnetic field $B = 78$ mT is shown in Fig. 2.9 (a). It can be seen by comparing with Fig. 2.8 that the spectrum of confined states is very weakly influenced by the magnetic field. The weak effect of the magnetic field is a consequence of the strong confinement of the states in the single kink potential. Figure. 2.9 (b) shows the magnetic field dependence at a fixed k. Importantly, the valley degeneracy is broken.

2.2.2 Double kink potential profile

Now, we discuss the case of a double kink potential, as presented in Fig. 2.10. In this Figure, the orange regions represent the $-V_a$ potential and the blue regions representing the $+V_a$ potential. The white region is the separation between the two electrodes and the kink-antinkink separation is indicated by L'_y.

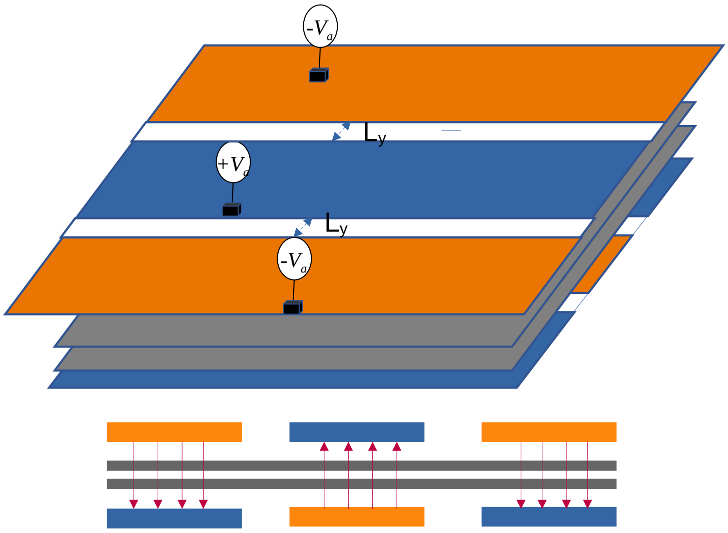

Figure 2.10: Sketch (Top) of bilayer graphene double kink potential created with voltage gates as indicated. We also show the electric field direction in the bottom sketch.

Figure 2.11.(a) shows the spectrum with double kink profile at zero magnetic field. As we see in the figure, at low energy there are four branches crossing zero energy, for each valley. Therefore, there are 8 branches in total and at $B = 0$ the two valleys are exactly valley degenerate [55].

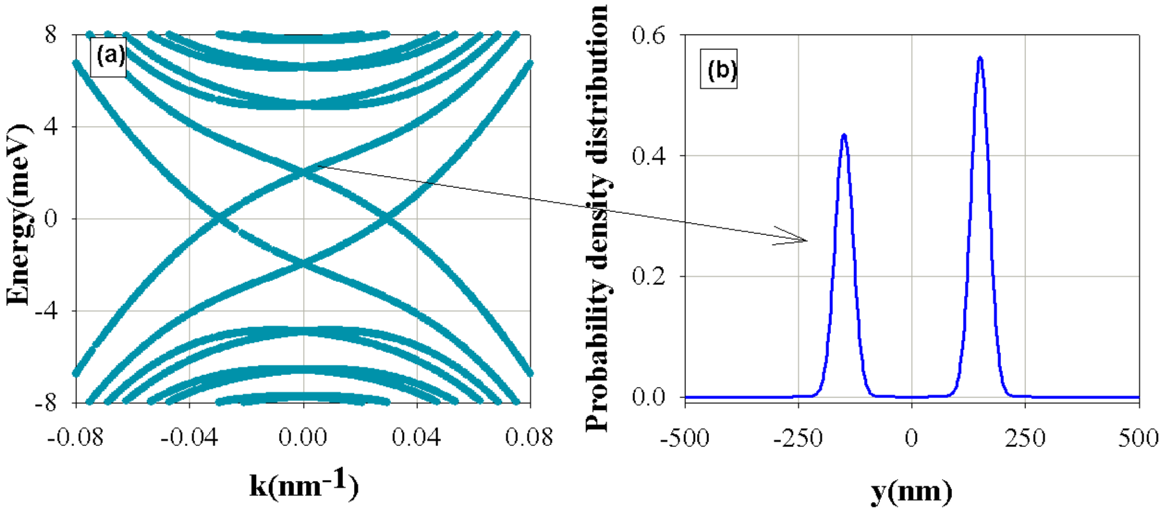

Figure 2.11: a) Bands of bilayer graphene under double kink potential at $B = 0$. b) Density distribution for the 1st state at $k = 0.002$ nm^{-1}.

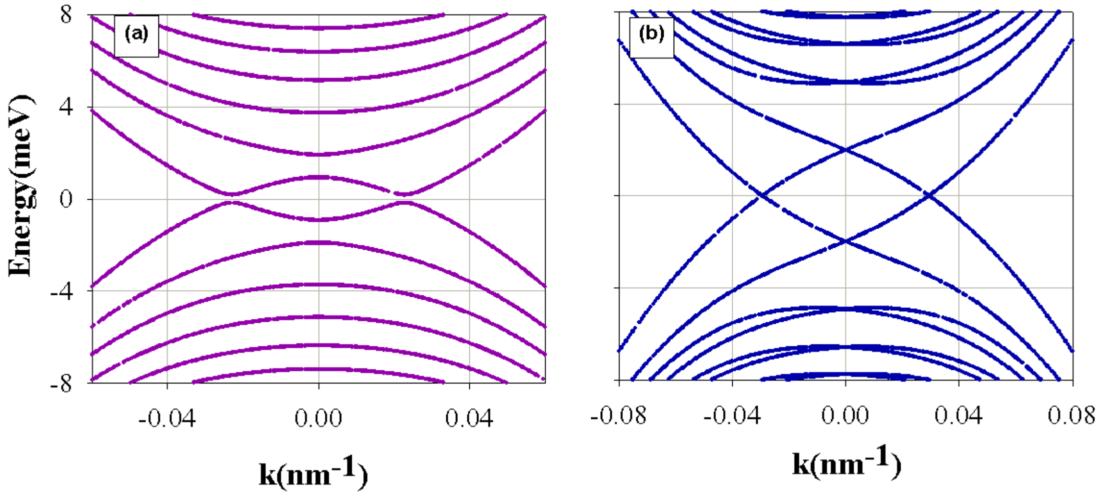

Figure 2.12: a) Bands of bilayer graphene under double kink potential at $B = 0$ T with $L'_y = 50$ nm; b) the same with $L'_y = 350$ nm.

In Fig .2.11.(b) we show the density distribution for the first state at the momentum k=0.002 nm^{-1}. We obtain a smooth density, which confirms the confinement of the state.

2.2.2.1 Dependence of the kink separation of the energy spectrum

Figure. 2.12 shows the dependence of the separation L'_y between the two kinks on bilayer graphene spectrum. When L'_y is small the behavior of the branches is changing and a small gap opens around $E = 0$. This will be important for the study of constrictions in Chapter 3.

2.2.2.2 Magnetic field dependence

As in the trivial confinement, the topological confinement shows a magnetic field dependence. As shown in the Fig. 2.13(a) the magnetic field of $B = 78$ mT breaks the valley degeneracy where the branches are shifted, the width $L'_y = 50$ nm opens the gap, with blue branches corresponding to valley K and red one corresponding to valley K'. In Fig. 2.13(b) we observe that if the width L'_y increases the spectrum is gapless and the valley degeneracy is broken.

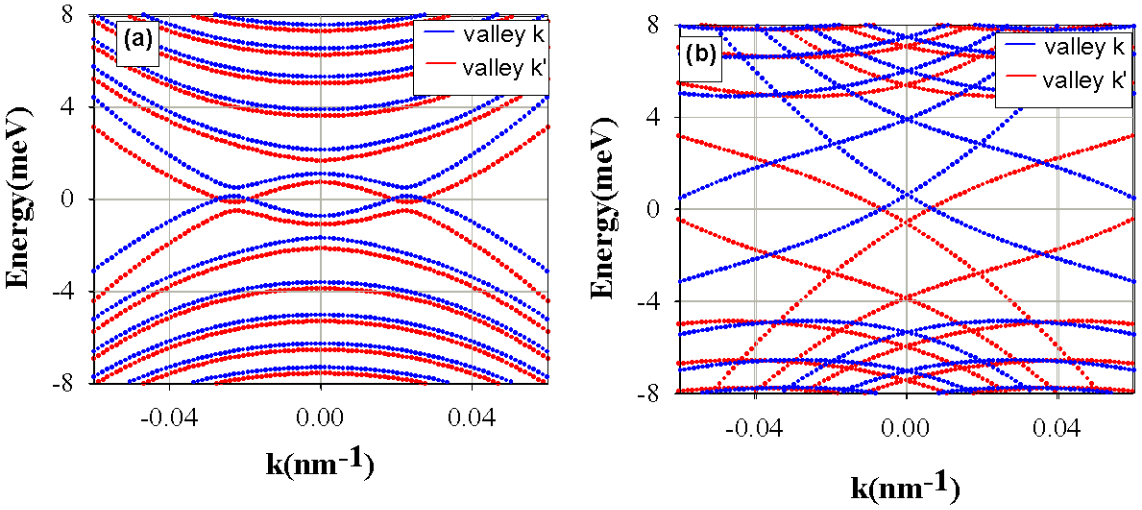

Figure 2.13: a) Bands of bilayer graphene under double kink potential at $B = 78$ mT with $L'_y = 50$ nm; b) the same with $L'_y = 350$ nm.

We also calculate the energy as function of magnetic field for a double kink potential at $k = 0.004$ nm^{-1} for both valleys (see Fig. 2.14). We find that the magnetic field does not show the Landau levels as in trivial confinement. We can see that there is no zero Landau level, but rather two parallel branches for each valley. Those topological branches do not fulfill the condition for Landau levels shown in Eq. (2.3).

2.3 Symmetries of the Hamiltonian

The strip 1D Hamiltonian with a fixed wavenumber, Eq. (2.1), has the following symmetries:

a) Valley symmetry. H commutes with τ_z and thus its eigenstates can always be labelled by a proper valley quantum number $\tau = \pm$.

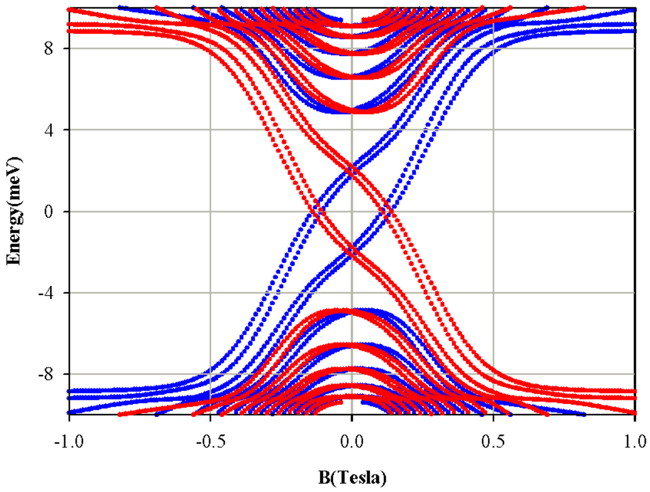

Figure 2.14: a) Energy as a function of magnetic field for bilayer graphene under double kink potential with L'_y=350 nm and $k = 0.004$ nm^{-1}.

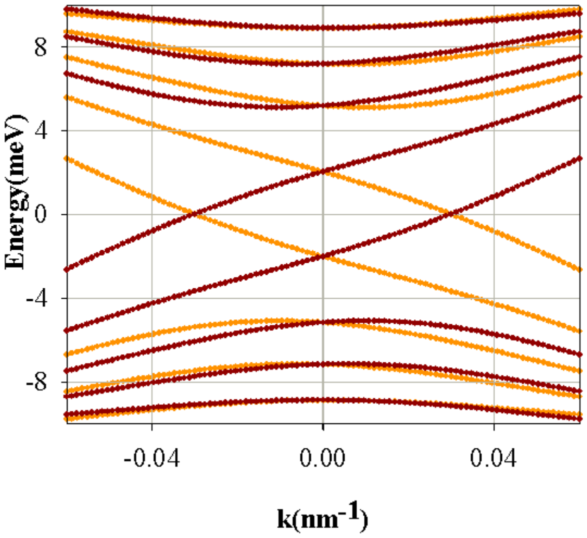

Figure 2.15: Bands for the two valleys at B=0 T for a single kink and smooth potential s =12.5 nm

As seen in Fig. 2.15, the valley is a good quantum number and this can be observed in the figure with two branches for each valley propagating in opposite directions.

b) Chiral symmetry ($\mathcal{C}$). For a vanishing symmetric potential ($V_s = 0$), eigenvalues of H come in pairs ±.

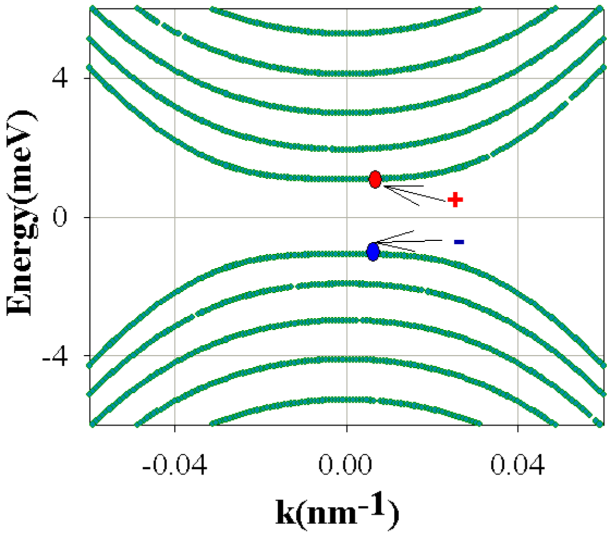

Figure 2.16: Bands of bilayer graphene at $B = 0$ and $V_a = 10$meV for a chosen valley K

The time reversal Θ and chiral-symmetry $\mathcal{C}$ operators and transformations relevant to our system read

$$\begin{aligned} &\Theta = i\tau_y\mathcal{K} &&\Rightarrow \quad \Theta^2 = -1\ , \quad \Theta H(B)\Theta = -H(-B)\ , \\ &\mathcal{C} = \sigma_x\tau_x\lambda_y &&\Rightarrow \quad \mathcal{C}^2 = 1\ , \qquad \mathcal{C}H\mathcal{C} = -H\ , \end{aligned} \tag{2.34}$$

where $\mathcal{K}$ refers to complex conjugation. The symmetry transformations on a state $|Ekv\rangle$ with a given energy, momentum and valley are given by $\Theta|Ekv\rangle \propto |E\bar{k}\bar{v}\rangle$ and $\mathcal{C}|Ekv\rangle \propto |\bar{E}k\bar{v}\rangle$.

Figure 2.16 shows that the states comes in pairs with different sign as represented by red color for the state of positive energy and blue for the state of negative energy, i.e they are symmetric.

2.4 Conclusion

In this chapter we have discussed the two confinement types due to the potential voltage applied to the bilayer graphene wires. On one hand, if the potential sign is the same on each side of the sheets, the spectrum shows a gap around zero energy and there are no confined states in the low energy gap. On the other hand, if the applied voltage in the same sheet of BLG is changing sign, this implies that the sides show opposite signs (the polarity inversion), and there exist chiral states which are localized at the interface between the two potential regions.

In the trivial confinement if the width of the wire is large the spectrum of energy becomes nearly gapless. Otherwise the spectrum opens a large gap and the behavior has 2D character. In the topological confinement for a single or double kink the behavior differs and the wave function has 1D character and the spectrum shows states propagating in opposite directions inside the gap, with two branches crossing zero energy.

These two confinement types also show a difference under the application of a perpendicular magnetic field. For the trivial confinement, the magnetic field dependence on the spectrum shows Landau levels in contrast to the topological confinement where this phenomenon is absent.

Chapter 3

Scattering of topological kink-antikink states in bilayer graphene structures

In this chapter, we will discuss scattering phenomena of the topological states under double kink potential, as introduced in Sec. 2.2.2. We will show here that kink-antikink local potentials enable modulated scattering of topological currents. We propose a device in which we can control the scattering of the topological states. This consists of a system that is composed of left and right regions and a central scatterer. The distribution of top/bottom gates enables the formation of a lateral constriction over the two parallel kinks. We find that the kink-antikink coupling leads to anomalous steps in the junction conductance. Further, when the constriction detaches from the propagating modes the conductance reveals the system energy spectrum.

3.1 Back-scattering-control proposal device

We already mentioned that bilayer graphene is an interesting material since we can tune its gap by applying an electric field. The application of a perpendicular electric field creates a potential difference between the two layers which finally lifts the electronic degeneracy [56, 57]. The gap thus opened can now be used to design tunnel barriers and quantum point contacts [58, 59]. Unlike monolayer point contacts that are fabricated by etching [60,61] and show trapped states due to edge roughness, BLG electrostatic quantum wires display clear conductance quantization steps. Further, if two of these barriers are connected in a series the device works as a quantum dot [41,62–64]. Therefore, robust spin or valley qubits can form in BLG dots showing a discrete spectrum. In the application of the inhomogeneous electric fields (kink potential) that changes its sign as we detailed in Sec. 2.2.2 we accomplish the creation of topological kink states.

The challenge then is how to probe and manipulate these unique kink states. This can be achieved with pairs of gates whose voltage is tuned independently in both the top and bottom layers for a single kink [50,51]. Experimentally, a conductance of $4e^2/h$ is observed [50,51,65] which demonstrates the presence of two current-carrying spin-degenerate valley-polarized modes. Alternate combinations of dual gates can be implemented for guiding these modes in valley valves and beam splitters [66–68]. However, signatures of disorder are detected, inducing backscattering and intervalley mixing. What is needed is a controlled source of backscattering that would allow to shape ballistic beam splitters for, e.g., topological valleytronic interferometry [69]. Here, we show that this is possible with a careful distribution of top/bottom gate pairs, enabling the formation of a lateral constriction over *two* parallel kinks, as sketched in Fig. 3.1(a). The two kinks have symmetric changes in the field polarity and opposite propagation directions for a given valley, thus one kink being the antikink of the other [8, 55]. We below demonstrate that a kink-antikink constriction is able to modulate the transmission electrostatically, what paves the way for the fabrication of topological quantum point contacts and wires.

Importantly, the setup can be slightly rearranged to also furnish bound states when the kink-antikink constriction (Fig. 3.1(b)) transforms into a side loop (Fig. 3.1(c)). Previous works on similar BLG islands assumed a sharp-potential kink [70] or infinite-mass boundary conditions [71] that create rings exhibiting Aharonov-Bohm energy levels. However, these are closed systems and as such their properties would be difficult to examine in an experiment. In contrast, our loops are weakly coupled to the external (side) kinks, topological as well. We show that the measured conductance peak pattern is caused by the system level distribution. Therefore, the setup is most suitable for doing spectroscopy

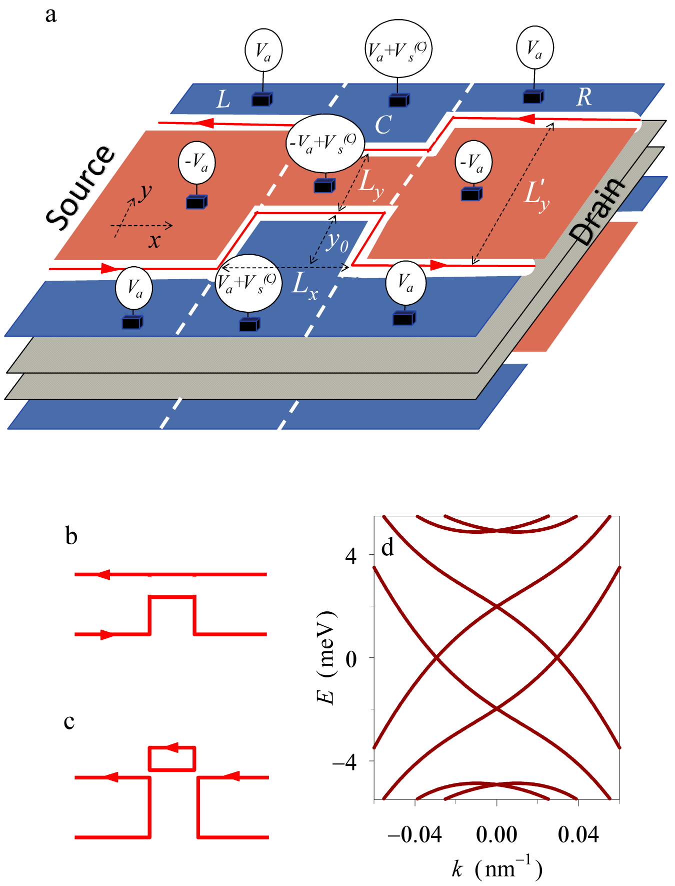

Figure 3.1: (a) Schematic of a bilayer graphene kink-antikink system with lead regions (L and R) and a central scatterer (C). The electric field direction on the graphene layers (gray sheets) is controlled by the voltages applied to the nine top and bottom gates (blue and orange regions). The values of the V_a applied potentials to the lower gates (not shown) are reversed with respect to the top gates. The field inversion between the blue and orange regions creates an interface (white region) where topological modes emerge. Additionally, a voltage $V_s^{(C)}$ is applied only to the central region. Red lines represent these propagating topological modes for the valley K. K' modes are obtained by reversing the arrows. Current is generated from the left (source) terminal to the right (drain) terminal. Dimensions and position of the central scatterer are given by L_x, L_y and y_0, while the asymptotic separation of the two kinks is L'_y. (b,c) Selected configurations representing a particular constriction (b) and side loop (c), the latter formed when $y_0 > L'_y$. (d) Energy bands of a translationally invariant kink-antikink wire of width $L'_y = 300\,\mathrm{nm}$, kink potential height $V_a = 10\,\mathrm{meV}$ and potential smoothness $s = 38\,\mathrm{nm}$. Each band is fourfold degenerate (spin and valley) in the absence of magnetic fields.

of chiral bound states.

Let us discuss in more detail our proposal, as illustrated in Fig. 3.1(a), and highlight our main findings. The system consists of a BLG with the same gate distribution in both the upper and lower graphene layers (gray sheets). The applied potentials to the lower gates, not shown in Fig. 3.1(a), reverse the values for V_a with respect to the top gates but keep the same value for $V_s^{(C)}$, as detailed below in Sec. 3.2. The changes in electric field orientation occur in the white interfaces defining, respectively, the topological kink and antikink that form the quasi-one dimensional (1D) propagating channels. The arrows in Fig. 3.1(a) qualitatively indicate electron propagation for a given valley on the BLG planes when the kink and antikink are well separated. x is the transport direction. The edge states are confined along y and the direction perpendicular to the graphene layers is denoted with z (not shown here). Electronic motion is determined by chirality due to valley-momentum locking (we only depict states from valley K).

A narrow constriction in the central region allows for a controlled transmission of the injected beams. In our parametrization (Fig. 3.1(a)), a constriction corresponds to having $L_y < L'_y$ and $y_0 \leq L'_y - L_y$. A particular example for a constriction is shown in Fig. 3.1(b) for $y_0 = L'_y - L_y$, although other configurations are possible. We find that for narrow constrictions the precise value of y_0 is not relevant and the conductance shows *anomalous* steps as the central potential is varied. If $y_0 \geq L'_y$ or $y_0 \leq -L_y$ the constriction becomes a loop that detaches from the left and right channels; Fig. 3.1(c) shows a case for $y_0 > L'_y$. For narrow loops the conductance displays *resonant* peaks as a function of central potential, their location giving information about the energy levels inside the loop. Altogether, the structure is a remarkable playground for electrical transport studies of both propagating and localized topological valley states.

3.2 Model

We use an effective eight-component model, valid for low energies near the Dirac points of the BLG crystalline band structure. Our starting point is the Hamiltonian given by

Eq. (2.1) [21, 72] which is repeated here for convenience:

$$H = \upsilon_F \left(p_x - \frac{y}{l_z^2} \right) \sigma_x \tau_z + \upsilon_F \, p_y \, \sigma_y + t(\lambda_+ \sigma_- + \lambda_- \sigma_+) + V_s + V_a(y)\lambda_z \quad , (2.1)$$

where V_s and V_a are respectively the symmetric and asymmetric potentials applied to the layers. We recall that for uniform potentials, V_s is just a global energy shift while V_a is a displacement energy that opens a gap in the BLG spectrum. The inhomogenous system of Fig. 3.1(a) has position dependent potentials $V_a(y)$ and $V_s(x)$, with transitions between plateau values defined by the gates.

We first discuss the spectrum that arises from Eq. (2.1) for a translationally invariant kink-antikink system at $B = 0$ and $V_s = 0$. The absence of a central region in Fig. 3.1(a) can be represented by $L_x = 0$ or, alternatively, by $y_0 = 0$ and $L'_y = L_y$. In this case, states propagate along x and are characterized by a real wave number k, i.e., $p_x \to \hbar k$ in Eq. (2.1). Whenever $V_a = V_a(y)$ changes its sign the gap is inverted and as a consequence four topological states per valley appear at each kink [8, 55]. These correspond to the branches seen around zero energy in Fig. 3.1(d). The states above $E = 4.2$ meV are extended states that do not remain attached to the kinks in contrast to the topological states. Further, the energy bands in Fig. 3.1(d) are not bounded either from below or from above since Eq. (2.1) describes Dirac fermions. We also note that H is both valley diagonal (so that each valley can be independently treated in a four-component subspace) and diagonal in the real spin basis. However, whereas all states are hereafter degenerate for spins up and down, the spectrum is not valley degenerate but obeys $E(k, \tau_z \to 1) = E(-k, \tau_z \to -1)$ due to time reversal symmetry. As a consequence, kink-antikink currents are valley unpolarized. Later, we will remark that a magnetic field breaks time reversal symmetry and thus valley polarizations can be observed in the measured conductance.

In our calculations, the kink potentials vary smoothly in y by means of a diffusivity s (see Sec. 2.1.1 for details of the potential modeling). This smoothness becomes important when the kink-antikink separation is small, i.e., the constriction in Fig. 3.1(b) or the loop in Fig. 3.1(c). Then, s couples the kink states running on the two sides, a mechanism that is eventually responsible for the transmission modulation. Along the transport direction x, the potential interfaces are considered sharp. This assumption is well justified since the mode wavelength λ is much larger than the characteristic length l_a for inversion of the static potentials. Electrostatic modeling in bilayer graphene [50, 51] yields an estimate $l_a < 50$ nm, while in our calculations we typically have $\lambda \gtrsim 300$ nm.

We next consider the inhomogenous situation with L, C and R regions along the transport direction x, sketched in Fig. 3.1(a). The distribution of applied potentials is seen in Fig. 3.1(a) for the top layer. Gates on the bottom layer have reversed V_a and the same central shift $V_s^{(C)}$. We solve the scattering problem in the presence of either the constriction or the loop using complex band structure methods as discussed in Sec. 2.2.1 [73, 74]. A survey of this method is given in Sec. 3.4.2. The technique is especially well suited to describe piecewise homogenous potentials in topological systems. For each region $a = L, C, R$ in Fig. 3.1(a), a large set of complex wavenumbers and eigenstates $\{k^{(a)}, \phi_k^{(a)}\}$ is determined by exact diagonalization [75]. These sets of solutions are then properly matched at the interfaces between central (C) and side regions (L, R). The ensuing linear system of equations yields the transmission amplitudes $t_{n'n}$ from input mode n to output mode n'. The electric conductance is then determined by the two-terminal formula $G = (2e^2/h) \sum_{nn'} |t_{n'n}|^2$, where spin degeneracy is already taken into account and we assume zero temperature (the experiments in Ref. [58] are done at a very low temperature of 1.7 K). The set of complex wavenumbers and wavefunctions of each region is obtained with a finite difference discretization of a 1D equation depending only on y since the x dependence disappears thanks to the homogeneity of each region along the transport direction. This 1D character enables an accurate numerical resolution for large numbers of y grid points, while no grid in x is needed.

The use of grid discretization methods for Dirac-like problems leads to the infamous fermion doubling problem [76–78], which introduces spurious replica states (see App. 7.1). These are characterized by very short wavelength oscillations, strongly fluctuating from one grid point to the next. Similar replicas are obtained in our approach when calculating the complex band structure of each region $\{k^{(a)}, \phi_k^{(a)}\}$. We filter out the replicas by coarse graining, performing an average with the right or left neighboring point and neglecting those states whose norm is affected by coarse graining. For dense grids, we easily arrive at an unambiguous identification of the physical states, which need to be smooth on the grid by definition. Thus, the fermion doubling problem does not affect the linear system that determines the conductance since G is based only on the sets of previously filtered solutions $\{k^{(a)}, \phi_k^{(a)}\}$ and no further spatial grid is required near the interfaces.

3.3 Results

We study two systems formed with the gate distribution and geometry depicted in Fig. 3.1(a): (i) when $0 < y_0 \leq L'_y - L_y$ propagating modes can exist within the central area and a quantum point contact behavior is expected (Fig. 3.1(b)); (ii) when $y_0 > L'_y$ a loop detaches from the left and right leads (Fig. 3.1(c)) and we will consequently find quantum resonance effects. In both devices, a key parameter is the symmetric potential $V_s^{(C)}$ in the central region, which acts as an effective local probe allowing energy spectroscopy of the constriction.

3.3.1 Quantum point contacts

We first present results for a constriction corresponding to a narrow point contact with a kink-antikink separation of 100 nm. This value is compatible with the width of presently available BLG point contacts [58, 59]. We set the kink diffusivity to $s = 38\,\text{nm}$, which is taken from the electric potential distribution in dual split gate BLG devices [50, 51], and assume an almost vanishing Fermi energy $E = 0.02\,\text{meV}$, close to the charge neutrality point. The results are not strongly affected by changes around this value, as long as higher energy modes in the asymptotic kink-antikink are not activated and remain far from the Fermi energy (cf. Fig. 3.1(d)).

The conductance for a $1\,\mu$m-long constriction (hereafter the wire) as a function of the central potential is shown in Fig. 3.2(a). We observe that G is strongly suppressed around $V_s^{(C)} = 0$ (region A). This is in principle a surprise since the presence of the edge states at $E = 0$ in Fig. 3.1(d) would imply a fully transparent constriction. However, when we

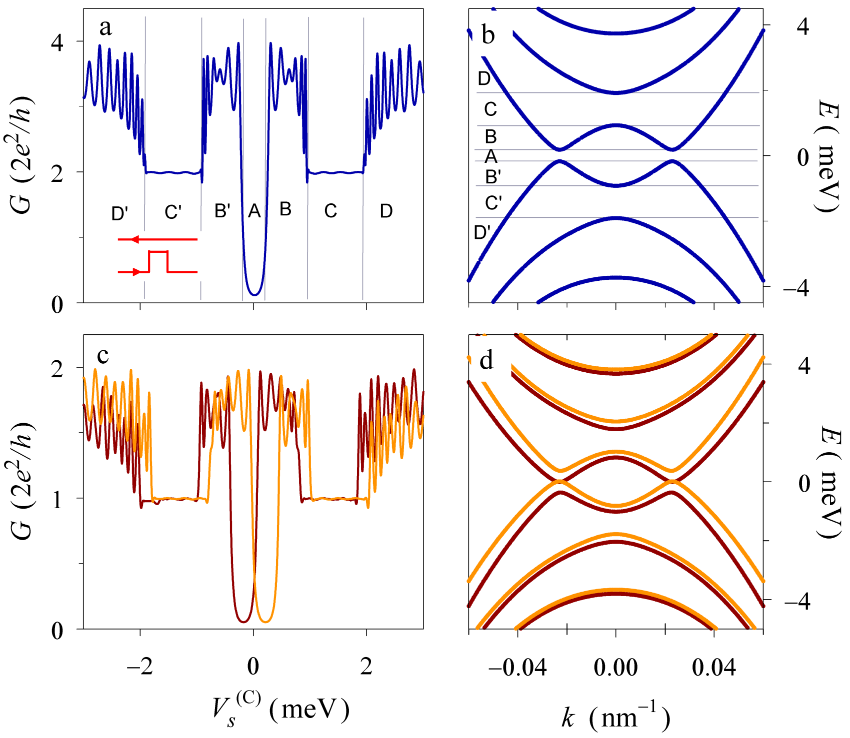

Figure 3.2: Results for a narrow constriction (inset in panel a) with $L_y = 100\,\text{nm}$, $y_0 = 200\,\text{nm}$ and a Fermi energy $E = 0.02\,\text{meV}$. (a) Conductance for $L_x = 1\,\mu\text{m}$ as a function of the central potential $V_s^{(C)}$. (b) Energy bands for a kink-antikink wire having the same parameters of the constriction. The capital letters and horizontal lines indicate the correspondence with the conductance ranges of panel a. (c,d) Same as panels a and b, respectively, with a magnetic field of $B = 50\,\text{mT}$. The two colors mark the two different valleys.

plot in Fig. 3.2b the wire band structure we notice that the topological bands display an absolute gap (for any k) in region A (details of this gap are discussed in App. 3.4.1). The kink potentials in the constriction couple the edge states, leading to an almost complete backscattering and hence a reduction of the conductance. G does not reach zero because the electrons can traverse the constriction by tunnel effect, which yields in any case a tiny value for G. Then, as $V_s^{(C)}$ increases the energy exceeds the gap and we find in region B two propagating states with positive velocity, per valley and spin. It follows that G quickly reaches the quantized value of $8e^2/h$. If $V_s^{(C)}$ is further enhanced we enter region C, where a single mode is only allowed, thus bringing G down to an anomalous step of $4e^2/h$. Finally, larger values of $V_s^{(C)}$ approach us into region D, where another

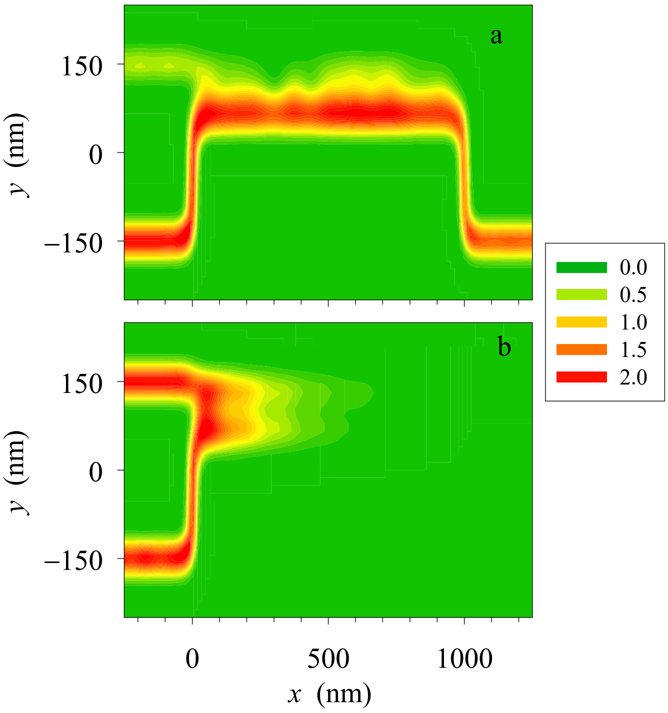

Figure 3.3: Density distribution, in arbitrary units, for the scattering states corresponding to the conductance curves of Fig. 3.2(c). Panels a and b are for the two different valleys K and K', respectively. Parameters: $L_x = 1000$ nm, $L_y = 100$ nm, $L'_y = 300$ nm, $y_0 = 200$ nm, $B = 50$ mT, $E = 0.02$ meV and $V_s^{(C)} = 0.2$ meV.

mode starts to contribute and G grows again. The oscillations seen in Fig. 3.2(a) are due to quantum interference of several modes coexisting in the wire. We can thus conclude that there is a remarkable correspondence between G and the wire energy bands. In fact, the particle-hole symmetry of Fig. 3.2(b) implies that $G(V_s^{(C)}) = G(-V_s^{(C)})$, as found in Fig. 3.2(a). We also point out that for nonzero temperatures the conductance curves will be thermal smeared.

A small magnetic field, in the mT range, suffices to yield large effects on the constriction conductance even if the valley splitting of the energy bands is small (Fig. 3.2(c)). Here, we choose to separately display each valley contribution to the conductance. Accordingly, the scale of G reduces a factor $2e^2/h$ as compared with Fig. 3.2(a). We find that the conductance shifts in opposite directions for the two valleys $\tau_z \to \pm 1$, making

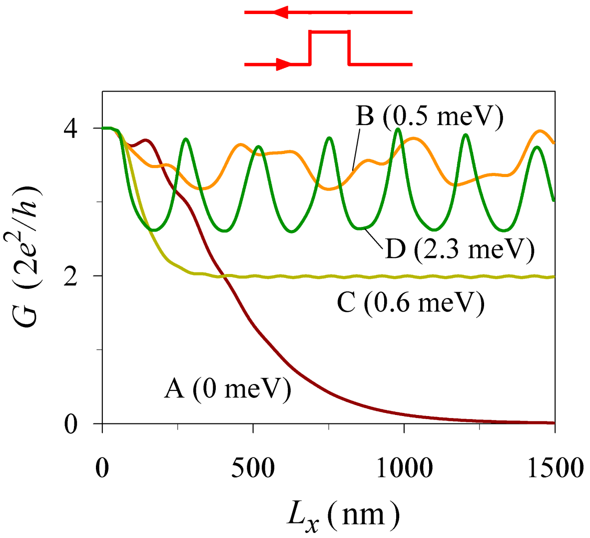

Figure 3.4: Dependence of the conductance on the constriction length L_x for the results of Fig. 3.2(a) and selected values of $V_s^{(C)}$, as given in parenthesis. A-D labels are used to indicate the same regions of Fig. 3.2(a).

it possible the creation of highly polarized valley currents, where one valley component is essentially blocked while the other is transmitted. The valley split bands are shown in Fig. 3.2(d). This behavior can be also seen with a single kink due to valley-momentum locking.

However, if we wish to invert the current valley polarization with a kink we would need to revert the extended lateral gates defining the kink whereas Fig. 3.2(c) shows the interesting possibility of switching the valley polarization by simply changing $V_s^{(C)}$, leaving both the lateral gates defining the kinks and the magnetic field fixed. Therefore, our system would work as an *electrically tunable, fully reversible valley filter* using tiny magnetic fields. Notice that BLG valley filters based on nontopological states require much larger fields, in the tesla range [79].

This is better seen in Fig. 3.3, where we plot the density distribution of the Fermi-energy scattering states when electrons are injected from the source terminal (left side). The two valleys (Fig. 3.3(a) and Fig. 3.3(b)) contribute differently since the magnetic field is finite. While for valley K electrons impinge from the bottom left kink (Fig. 3.3(a)), the opposite valley K' electrons (Fig. 3.3(b)) enter from the top left kink. The former (latter) are mostly transmitted (reflected), giving rise to a valley polarized current in the drain terminal (right side).

The dependence of G on the constriction length L_x (see Fig. 3.4) further supports our interpretation. We display the conductance for $V_s^{(C)}$ corresponding to the four regions indicated in Fig. 3.2(a). In the gapped region A the conductance decays exponentially for large values of L_x, which agrees with a transport mechanism based on tunnel effect. In region B the conductance shows an oscillatory behavior up to arbitrarily large distances, implying a Fabry-Perot interference between propagating modes in the central area. The conductance becomes quantized at $4e^2/h$ in region C, which occurs when the interfaces between the leads and the constriction becomes transparent. Finally, in region D we recover the oscillatory behavior due to the activation of a new transport channel. In all cases the role of quantum tunneling for small L_x is clearly seen because the conductance increases as L_x shrinks to zero and scattering thus disappears.

3.3.2 Side loops

Let us turn to the loops created as the gate position y_0 shown in Fig. 3.1(a) increases. Then, the edge states in the central region detach as illustrated in Fig. 3.1(c). Figure 3.5(a) shows in this case a conductance pattern that strongly differs from the wire system of Fig. 3.2(a). G is characterized by resonant peaks that reach values of the order of $4e^2/h$ (we plot $G/2$ for convenience). Interestingly, these peaks are causally correlated with the discrete levels in the closed loop. To see this, we plot in Fig. 3.5(d) the loop energy spectrum.

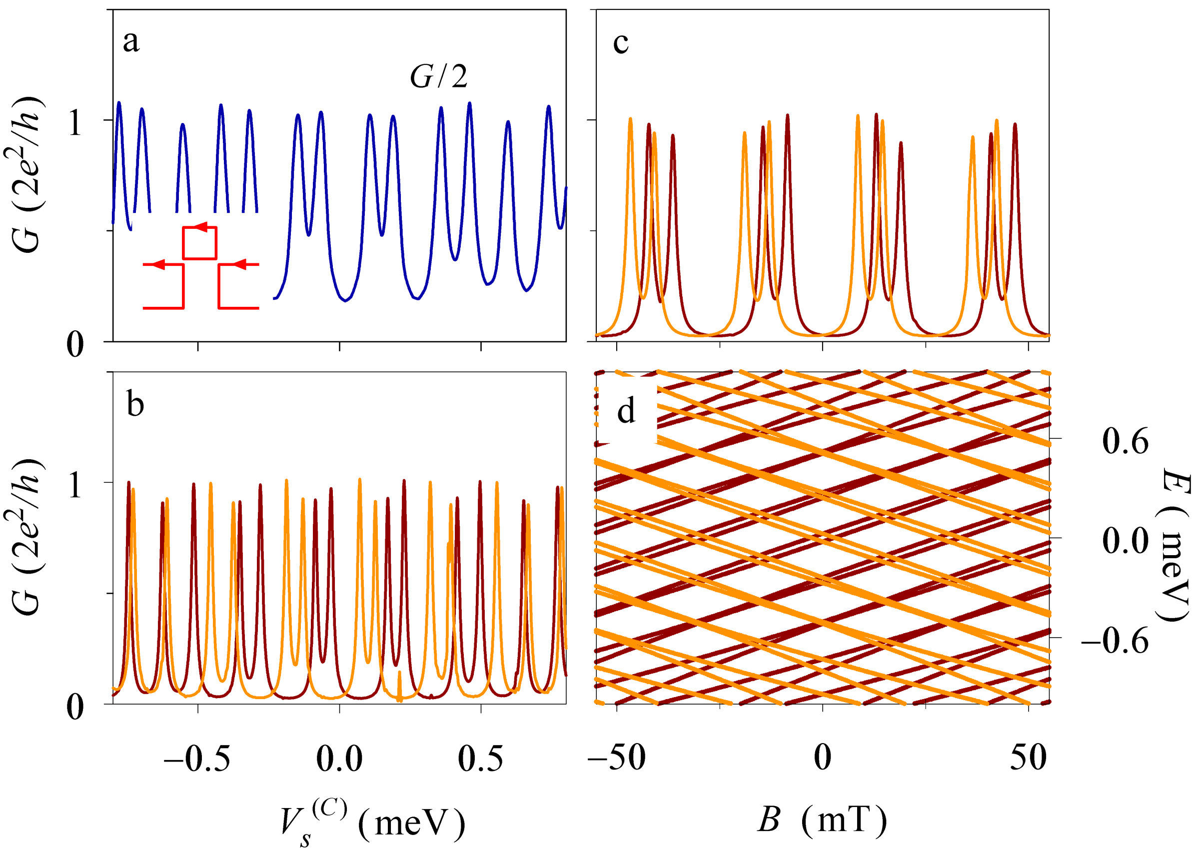

Figure 3.5: Results for a side loop (inset in panel a) with $L_y = 150\,\mathrm{nm}$, $y_0 = 310\,\mathrm{nm}$ and Fermi energy $E = 0.02$ meV. (a,b) Conductance for $L_x = 1\,\mu\mathrm{m}$ as a function of the central potential $V_s^{(C)}$ for $B = 0$ (a) and $B = 50\,\mathrm{mT}$ (b). (c) Conductance as a function of the magnetic field for $V_s(C) = 0$. (d) Energy levels for the finite loop $(L_x, L_y) = (1\,\mu\mathrm{m}, 150\,\mathrm{nm})$ as a function of the field. The two colors in panels b-d indicate the two different valleys. The peak separation [around 0.04 meV in (b)] could be resolved at low temperatures $T \lesssim 0.5\,\mathrm{K}$.

We find that the position of the conductance peaks agree, apart from a slight renormalization due to the coupling with to external edge states, with the level positions. The particular peak structure is highly sensitive to the loop dimensions (L_x, L_y) due to quantum confinement.

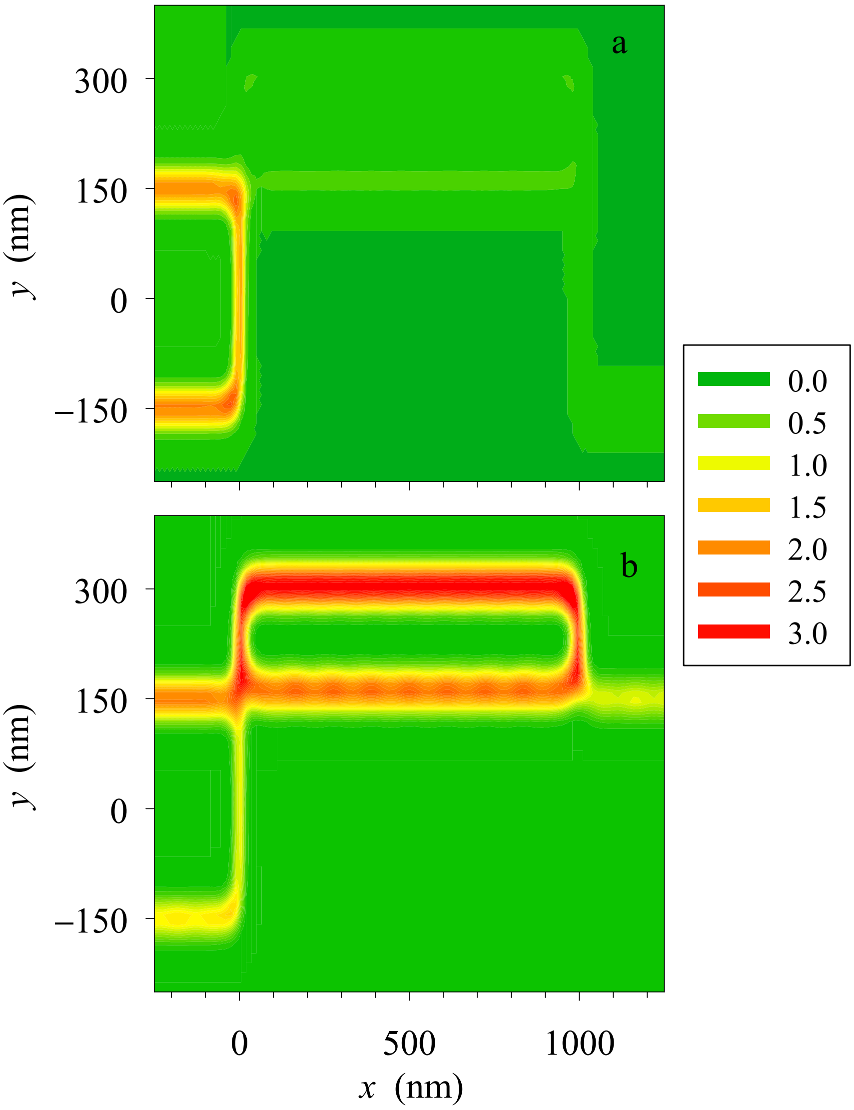

Figure 3.6: Density distribution corresponding to the results of a side loop depicted in Fig. 3.5(b). The central gate potential is $V_s^{(C)} = 0.3\,\text{meV}$ and it corresponds to a K' valley peak (light color) in Fig. 3.5(b). Panels a and b are for the two different valleys K and K', respectively. Parameters: $L_x = 1000$ nm, $L_y = 150$ nm, $L'_y = 300$ nm, $y_0 = 310$ nm, $B = 50$ mT, $E = 0.02$ meV and $V_s^{(C)} = 0.3$ meV.

A small magnetic field splits the conductance peaks, as shown in Fig. 3.5(b) where we plot the valley resolved G for $B = 50$ mT. It is noticeable that the peak widths are significantly reduced in the presence of B, thus leading to smaller conductance minima; cf. Figs. 3.5(a) and 3.5(c).

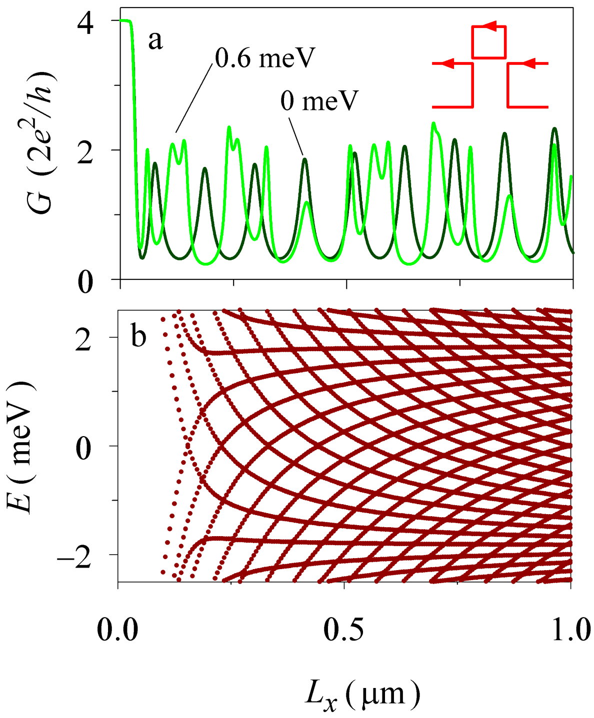

Figure 3.7: (a) L_x dependence of the conductance for two selected values of $V_s^{(C)}$ for the parameters of the $L_y = 150$ nm side loop of Fig. 3.5(a). (b) Energy levels of the closed rectangular loop with $L_y = 150$ nm as a function of L_x.

The conductance splitting is explained with the level behavior as a function of B as shown in Fig. 3.5(d). The field acts differently on the two valleys, thus raising (lowering) the energy for $\tau_z \to 1$ ($\tau_z \to -1$). B-splitting of the two valleys is also present for the case of non topological bound states in graphene circular quantum dots, discussed in Ref. [80], where states of the same angular momentum and opposite valleys show opposite dispersions at low fields. Besides the splitting, the spectrum in Fig. 3.5(d) for topological loops shows a pattern of almost parallel lines for each valley, reflecting a quantization condition of the topological states along the perimeter of the loop [70]. Our results obey reciprocity, i.e., G is unchanged when both B and the valley index are simultaneously reversed, as can be seen in Fig. 3.5(c). It is also worth stressing that the valley and gate sensitivity allows, as in the constriction, switching the valley polarization of the current by soley tuning the gate potential, only that a finer tuning is needed in the detached

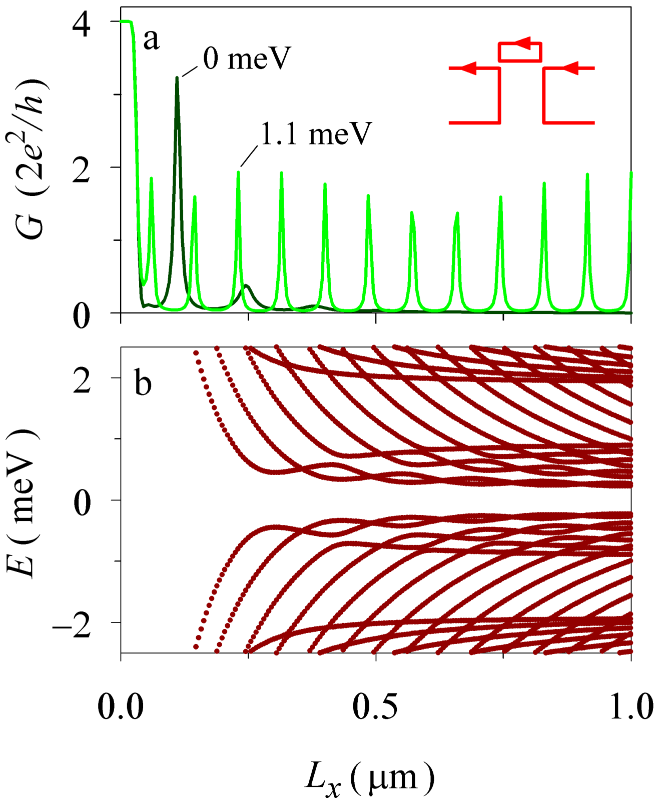

Figure 3.8: (a) L_x dependence of the conductance for a narrow loop ($L_y = 100$ nm) and two selected values of $V_s^{(C)}$ with the rest of the parameters as in Fig. 3.7. (b) Energy levels of the closed loop with the same $L_y = 100$ nm as a function of L_x.

loop in order to hit the narrower peak maxima. Resolving the narrow peaks needs low temperatures to avoid thermal broadening, which we can estimate below 500 mK based on Fig. 3.5.

Probability density distributions in space provide a more visual support for this valley switch effect (see Fig. 3.6). We note that just one valley is populating the loop (Fig. 3.6(b)) while the other one is reflected (Fig. 3.6(a)). Thus, the valley-split resonant conductances of side loops in small magnetic fields imply high valley accumulations on the loop for specific gate potentials.

We now briefly discuss the dependence on L_x. In Fig. 3.7 we show results for a wide loop of $L_y = 150$ nm as in Fig. 3.5(a). For $V_s^{(C)}$ corresponding to a conductance valley in

Fig. 3.5(a) the conductance curve in Fig. 3.7(a) (black line) shows a single-mode regular spacing, which is in agreement with the degeneracy due to level crossing for $E = 0$ of Fig. 3.7(b). In contrast, for a $V_s^{(C)}$ value that generates a G peak in Fig. 3.5(a) the conductance curve shows multiple-mode spacings in Fig. 3.7(a) (light green line). Further, we get accidental crossings at values of L_x that lead to additional factor-2 degeneracies in Fig. 3.7(b). The case of a narrow loop ($L_y = 100$ nm) is shown in Fig. 3.8. In contrast to the previous case, the conductance valley curve is quenched as L_x increases (black line in Fig. 3.8(a)) whereas the peak curve exhibits a beating pattern overimposed to the peak sequence (green line). Figure 3.8(b) shows the energy levels when the narrow loop is closed. We observe regions with a bunching of levels separated from others with regularly spaced levels. This is consistent with the conductance peaks obtained in Fig. 3.8(a). Despite the fact that the conductance patterns depend on the specific geometry of the loop (via L_x and L_y), in all cases the conductance peaks are correlated with the energy levels of the closed loop. Thus, the conductance serves as an excellent tool to probe the internal structure of topologically bound states.

3.4 Discussion

3.4.1 Kink-antikink gap

We address here how the gap of the kink-antinkink band structure (see Fig. 3.2(b)) varies with the separation L_y and the potential diffusivity s. The results are shown in Fig. 3.9(a) and (b), respectively, and they confirm, as was anticipated (see Fig. 3.4), that the gap strongly increases when L_y decreases. However, it is remarkable that this dependence is non monotonic, with oscillations and with particular values of L_y and s for which the gap vanishes. This behavior can be attributed to the oscillations of the wave functions [8, 55], as can be seen from the overlap of two displaced kink states

$$\mathcal{O}(L_y) = \left| \int dy \, \boldsymbol{\phi}^{T*}(y) \, \boldsymbol{\phi}(y - L_y) \right| \, , \tag{3.1}$$

shown in the inset to Fig. 3.9(a). In Eq. (3.1) $\boldsymbol{\phi}$ is the eight-component wave function (and $\boldsymbol{\phi}^T$ its transpose) for a real k near the branch crossing at zero energy of the single

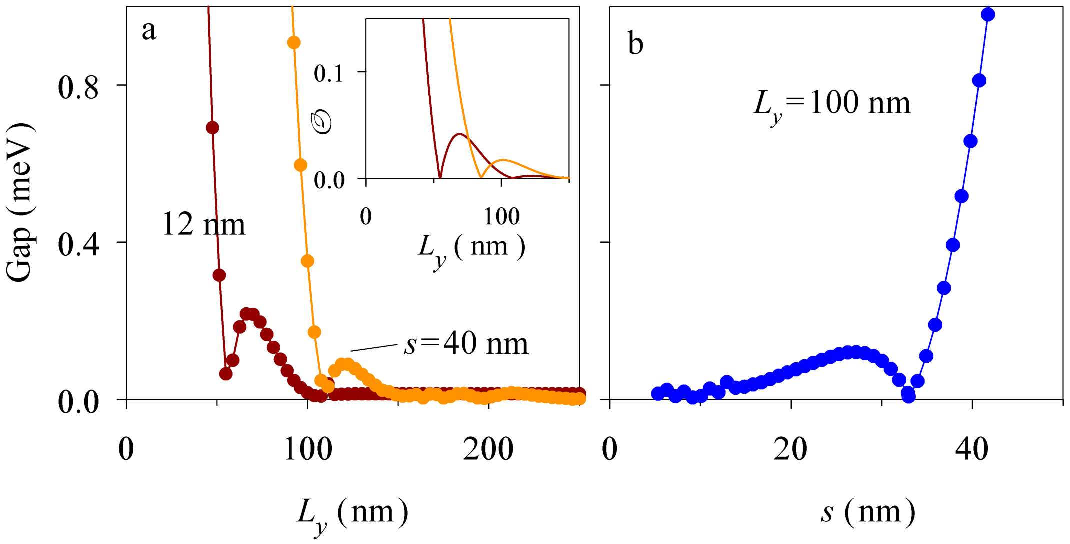

Figure 3.9: a) Energy gap of the kink-antikink band structure as a function of the separation L_y and for two potential diffusivities s. The data points are obtained from the numerical band structure while the joining lines are a guide to the eye. The inset shows the wave function overlap $\mathcal{O}$ of independent kink and antikink as a function of distance with the same color code. b) Energy gap as a function of the diffusivity for a fixed separation. Parameters: $V_a = 10\,\mathrm{meV}$, $V_s = 0$.

kink. For the steep potential in Fig. 3.9 ($s = 12\,\mathrm{nm}$) the L_y of minimum gap and the L_y of vanishing overlap are in good agreement, while for the smooth potential ($s = 38\,\mathrm{nm}$) the agreement is only qualitative.

3.4.2 Scattering with complex band structure

Having mentioned in Sec. 3.2 the overall idea of the complex-band-structure approach, we here present the details of the method. The double junction, Fig. 3.1, is formed by three regions $a = L, C, R$, each one homogenous along x. Introducing a local wave number $p_x \to \hbar k^{(a)}$ and a factorizing wave function $\phi_k^{(a)}(y\eta_\sigma\eta_\tau\eta_\lambda)e^{ik^{(a)}x}$, with $\eta_{\sigma\tau\lambda} = 1, 2$ representing the pseudospin discrete components, the energy eigenmode equation from Hamiltonian given by Eq. (2.1) for each region can be recast as

$$\begin{aligned}\Big[&\tfrac{E}{v_F}\,\tau_z\sigma_x + \hbar\tfrac{y}{l_z^2} - i p_y\tau_z\sigma_z - \tfrac{t}{2v_F}\,\tau_z(\lambda_x + i\lambda_y\sigma_z)\\ &-\tfrac{V_s}{v_F}\,\tau_z\sigma_x - \tfrac{V_a(y)}{v_F}\,\lambda_z\tau_z\sigma_x\Big]\,\phi_k^{(a)} = \hbar k^{(a)}\,\phi_k^{(a)}\ ,\end{aligned} \tag{3.2}$$

where we left-multiplied all terms by $\sigma_x\tau_z/v_F$, included a global sign change and moved the $k^{(a)}$ linear term to the right-hand side. Equation (3.2) is an eigenvalue equation for the mode sets $\{k^{(a)}, \phi_k^{(a)}\}$ corresponding to a given energy E. The problem is non-Hermitian due to the $ip_y\tau_z\sigma_z$ and $i\lambda_y\sigma_z$ contributions, physically allowing the possibility of complex wave numbers $k^{(a)}$. We solve Eq. (3.2) as a matrix eigenvalue problem, introducing a uniformly spaced 1D grid for the y coordinate, determining the topological modes smoothly vanishing at the y boundaries with numerical methods well suited to large sparse matrices [75]. The local complex wavenumbers and modes are our complex band structure basis sets in term of which we represent the solution in each region of the double junction.

region	mode character	condition
C	output	none
L	input/output prop.	$I_k^{(a)} > 0(< 0)$; $\mathrm{Im}(k^{(a)}) = 0$
L	input/output evan.	$\mathrm{Im}(k^{(a)}) > 0(< 0)$
R	input/output prop.	$I_k^{(a)} < 0(> 0)$; $\mathrm{Im}(k^{(a)}) = 0$
R	input/output evan.	$\mathrm{Im}(k^{(a)}) < 0(> 0)$

Table 3.1: Summary of the conditions for mode clasification as input or output in the three device regions. $I_k^{(a)}$ is the mode flux defined in Eq. (3.6).

The wave function is given by a set of amplitudes $\{C_k^{(a)}\}$ in each x-homogenous region as

$$\Psi^{(a)}(xy\eta_\sigma\eta_\tau\eta_\lambda) = \sum_{k^{(a)}} C_k^{(a)}\, \phi_k^{(a)}(y\eta_\sigma\eta_\tau\eta_\lambda)\, e^{ik^{(a)}(x-x_k^{(a)})}\ . \tag{3.3}$$

The $x_k^{(a)}$ values in Eq. (3.3) are a gauge-like choice for the amplitudes $C_k^{(a)}$. This choice has its importance to avoid numerical instabilities due to exponentially large numbers with complex wave numbers. For $a = L(R)$, the sum in Eq. (3.3) only includes wavenumbers with either zero or negative (positive) imaginary parts and we set $x_k^{(L,R)} = x_{1,2}$, with $x_{1,2}$ the positions of the two interfaces. In the central region, however, Eq. (3.3) includes wave numbers with both ≤ 0 and > 0 imaginary parts, and we set $x_k^{(C)} = x_2$ and x_1 for those two cases, respectively.

At the two interfaces $x_{1,2}$ the wave function fulfills continuity. This is the only requirement with a Dirac-like Hamiltonian like Eq. (2.1), as opposed to a Schrödinger problem where the kinetic term also requires continuity of the wave function first derivative. The continuity conditions yield the amplitudes of outgoing modes $C_k^{(L,C,R)}$ in terms of those for input modes. The latter are assumed nonvanishing in the left lead only. Thus, we obtain a closed set of linear equations by projecting the continuity conditions at the two interfaces on the total set of outgoing complex modes. In detail, the linear system reads

$$\left\{\begin{array}{lll} \displaystyle\sum_{k^{(L)}\,\mathrm{out}} \mathcal{M}^{(aL)}_{k'k}\, C^{(L)}_k & \displaystyle -\sum_{k^{(C)}\,\mathrm{out}} \mathcal{M}^{(aC)}_{k'k}\, e^{ik^{(C)}(x_1-x^{(C)}_k)}\, C^{(C)}_k & \\ & \displaystyle = -\sum_{k^{(L)}\,\mathrm{in\,prop.}} \mathcal{M}^{(aL)}_{k'k}\, C^{(L)}_k \ , & \text{if } x^{(a)}_{k'} = x_1 \ , \\ \displaystyle\sum_{k^{(R)}\,\mathrm{out}} \mathcal{M}^{(aR)}_{k'k}\, C^{(R)}_k & \displaystyle -\sum_{k^{(C)}\,\mathrm{out}} \mathcal{M}^{(aC)}_{k'k}\, e^{ik^{(C)}(x_2-x^{(C)}_k)}\, C^{(C)}_k & \\ & = 0 \ , & \text{if } x^{(a)}_{k'} = x_2 \ , \end{array}\right. \tag{3.4}$$

$$\mathcal{M}^{(ab)}_{k'k} = \sum_{\eta_\sigma \eta_\tau \eta_\lambda} \int dy\, \phi^{(a)*}_{k'}\, \phi^{(b)}_k \ , \tag{3.5}$$

where we have defined the overlap matrices 3.5 and, as mentioned, the sum on the right-hand side of Eq. (3.4) is restricted to the $k^{(L)}$ input propagating modes (with vanishing imaginary wavenumber) while those on the left-hand side contain output modes of all types, i.e., propagating and evanescent.

The input/output character of the modes is summarized in Tab. 3.1. Notice that in the central region all modes are output modes, while in left and right regions there can be input modes of propagating or evanescent character, in our notation. In L and R, the propagating modes are classified as input or output depending on their quasiparticle flux, defined as (see App. 7.2)

$$I^{(a)}_k = \langle \phi^{(a)}_k | v_F \tau_z \sigma_x | \phi^{(a)}_k \rangle \ , \tag{3.6}$$

where $\partial H/\partial p_x = v_F \tau_z \sigma_x$ is the x-velocity operator.

Setting $C^{(L)}_k = 1$ for a particular input propagating mode in Eq. (3.4), with all other inputs vanishing, we obtain a particular input/output pair transmission $t_{n'n} \propto C^{(L,R)}_{k'}$ by solving the linear system. We have numerically checked that flux conservation is fulfilled in our method when the number of modes in each region is large enough. Typically, with 300 modes in each region we obtain a flux conservation with an error of 0.1% or even smaller.

3.5 Conclusions

We have proposed a versatile nanodevice for topological studies in quantum valley transport. Transmission manipulation is achieved by means of a kink-antikink local potential that allows the formation of (i) point contacts with anomalous quantized conductance and (ii) side loops with chiral quasi-bound states. The obtained conductance curves provide information on the system energy spectrum. For tiny magnetic fields we obtain a valley polarization effect and this polarization is tunable with the gate potential.

Possible drawbacks of our proposal might be the effect of imperfections and misalignments of top and bottom gates in Fig. 3.1(a) as well as the presence of disorder due to impurities. Our results, however, suggest robustness against small gate displacements since we take into account smooth transition profiles of the asymmetric potential with diffusivity values as large as $s \approx 40\,\mathrm{nm}$. On the other hand, the chiral character of the low-energy valley-momentum-locked states offers protected transmission against backscattering by impurities that conserve the valley degree of freedom [81].

The illustrative examples considered in this work do not exhaust the capabilities of the system, and more sophisticated setups could be envisaged. Further, our model could be straightforwardly extended to multivalley materials other than bilayer graphene such as silicene [82], sonic crystals [83] and photonic platforms [84].

Chapter 4

Geometry effects in topologically confined bilayer graphene loops

In this chapter, we investigate the topological electronic confinement in bilayer graphene in topological loops of different shapes (circle, square, rectangle, and irregular polygon). These loops are created by lateral gates acting via gap inversion on the two graphene sheets. We find that the behavior of the spectrum is different from the one obtained in the wires (see Chap. 2). We discuss also here two models: a quantum perimeter model (QPM) which is based on Ref. [8], and a quantum 2D model (Q2DM) which consists of solving numerically the low-energy Hamiltonian.

4.1 Introduction

In Chapter 2, the confined states were intrinsically 1D-like, with a characteristic transverse decay length, and they propagate along the domain wall with locked relative orientations of momentum and valley pseudospin. In the absence of valley mixing potentials states for the K and K' valleys, electrons propagate along the wall, without backscattering, showing opposite chiralities. This property is similar to the helical states within the quantum spin Hall effect [85–87] if we replace spin with the valley pseudospin of graphene.

Now, here in this chapter, let us suppose that the external gates are arranged in such

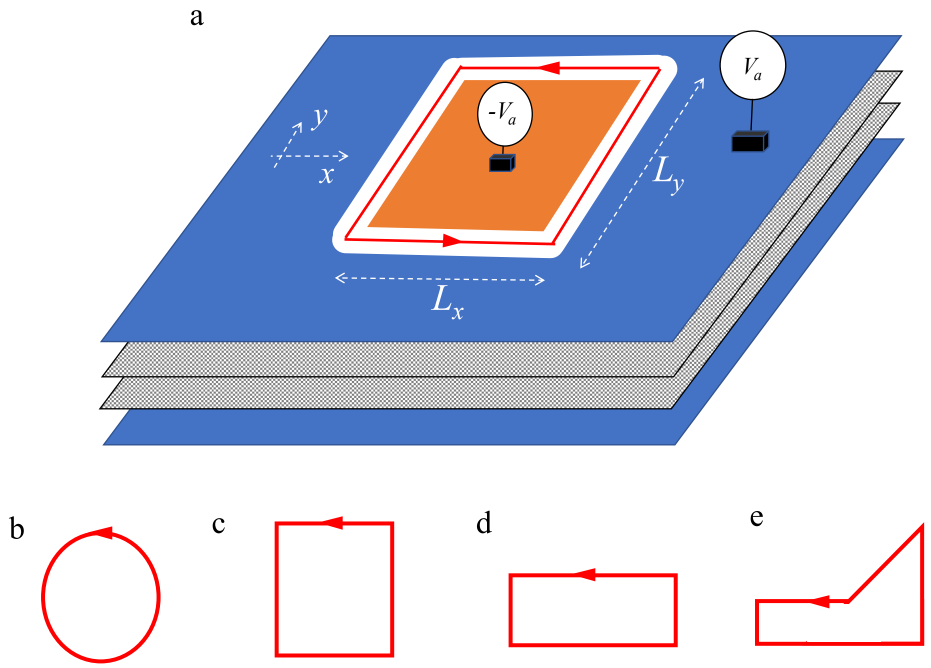

Figure 4.1: a) Scheme of a topological loop showing the bilayer graphene sheets (gray) and lateral gates with the applied gate potentials $\pm V_a$ (orange and blue, respectively). Two identical lower gates, hidden behind the lower graphene sheet, have the opposite potentials of the corresponding top gates. The white 1D region between orange and blue gates hosts the topological loop state on the graphene sheets, with counterpropagation for the two valleys. A red arrow is indicating the circulation for only one of the two valleys. b)-e) Loop shapes considered in this chapter, from highest to lowest symmetry: circle, square, rectangle and irregular polygon.

a way that the domain wall closes into itself. A schematic representation is shown in Fig. 4.1a. Then, a loop forms supporting electronic bound states [70] and the following question naturally arises. What is the effect of different loop shapes onto the energy spectrum of these bound states? Being 1D-like, topologically confined sates in BLG are expected to essentially depend on the loop perimeter unlike the trivial potential confinement, which depends both on the surface and the shape of the confining region. Nevertheless, it is important to notice that the domain-wall states depicted with a red line in Fig. 4.1a are in reality quasi-1D with a finite spatial width. Therefore, the discrete energy spectrum will be in general a function of the system's geometrical symmetries, the region aspect ratio, etc. Below, we present a detailed investigation for topological loops of different shapes and symmetries. First, we show with the aid of an exactly solvable model that the energy spectrum is uniquely determined by the loop perimeter provided that the system size is large. Yet, for smaller loops finite size effects become important and the spectrum depends on the particular geometrical structure. This dependence is better seen in the sequence of zero energy crossing and anticrossings as the perimeter increases.

In the presence of a magnetic field B, the dispersion is affected by the flux piercing the topological loop. This creates an energy splitting for the two valleys and an asymmetry with respect to energy inversion ($E \to -E$) in the spectra as a function of perimeter. The B-dependence of the spectra with a fixed perimeter and shape is characterized by magnetic periodicities of Aharonov-Bohm type. Therefore, the loops host persistent currents at finite fields that, similarly to the $B = 0$ spectra, exhibit geometry dependent features in the small size limit, showing that currents would serve as an excellent tool to probe topologically confined states in BLG nanostructures.

4.2 Theory

4.2.1 A quantum perimeter model (QPM)

An analytic model of topological loops in BLG can be devised utilizing the results of Ref. [8] for a straight domain wall with an abrupt transition $+V_a$ to $-V_a$ (the kink). The analytic relations between linear momentum p along the kink and energy E of the two topological branches, corresponding to the two valleys (K, K'), were given in Ref. [8] and in Sec.2.2.1 as $p = f_{1,2}(E)$, with

$$f_{1,2}(E) = \frac{-E \pm \frac{V_a}{\sqrt{2}}}{\left(\mp E + V_a\sqrt{2}\right)^{1/2}} \frac{\sqrt{t}}{v_F} \, , \tag{4.1}$$

where the Fermi velocity $\hbar v_F = 660\,\mathrm{meV\,nm}$ and the interlayer coupling $t = 380\,\mathrm{meV}$ are BLG intrinsic parameters, as already stated in Sec. 1.2.2.

In a closed loop of perimeter $\mathcal{P}$ we can assume that the tangent momentum p is quantized, such that an integer number of wavelengths must fit into $\mathcal{P}$,

$$p \to p_n \equiv \hbar \frac{2\pi n}{\mathcal{P}} \; , \quad n = \pm 1, \pm 2, \dots \; , \tag{4.2}$$

where negative n's represent negative momenta (i.e., opposite propagation) and the perimeter quantization in terms of wavelength λ reads $\mathcal{P} = |n|\lambda$. Since the Berry phase in BLG is 2π (see Sec. 1.4) [37] its effect is already contained in the integer n's of Eq. (4.2).

We can also add a magnetic field, represented by a vector potential $\vec{A}$, and write the circulation integral

$$\int_{\mathcal{P}} dl \, (p_n + eA_t) = f_{1,2}(E) \int_{\mathcal{P}} dl \; , \tag{4.3}$$

where A_t is the component of the vector potential tangent to the kink. Noticing that $\int_{\mathcal{P}} dl = \mathcal{P}$ and $\int_{\mathcal{P}} A_t \, dl = SB \equiv \Phi$ (S, B and Φ being the loop surface, the perpendicular magnetic field and the magnetic flux, respectively) we find an implicit condition from which one can derive the bound state energy E for a given loop perimeter, magnetic flux and principal quantum number n:

$$f_{1,2}(E) = \frac{2\pi\hbar}{\mathcal{P}} \left(\frac{\Phi}{\Phi_0} + n \right) \; , \tag{4.4}$$

where $\Phi_0 = h/e$ is the flux quantum.

Equation (4.4) is our quantum perimeter model (QPM) for bound states in BLG topological loops. As anticipated, when $\Phi = 0$ the relation depends only on the perimeter and is totally independent of the loop geometry. At finite fields, however, the bound-state energies depend on the loop surface through the Aharonov-Bohm flux ratio Φ/Φ_0. We expect the QPM to be reliable for large enough loops, when different parts of the loop do not interfere. In small loops, the traversal extension of the topological states becomes comparable to the distances inside the loop and the QPM breaks down. Below, we investigate deviations from the QPM using an exact approach for BLG within the continuum limit.

4.2.2 A quantum 2D model (Q2DM)

The low-energy Hamiltonian describing the states that are formed in two-dimensional (2D) BLG nanostructures for energies near the Dirac points is the one that we used in our previous chapters [72,88] (see Eq. (2.1)):

$$\begin{aligned} H &= v_F \left(p_x - \hbar \frac{y}{2l_z^2} \right) \tau_z \sigma_x + v_F \left(p_y + \hbar \frac{x}{2l_z^2} \right) \sigma_y \\ &+ \frac{t}{2} \left(\lambda_x \sigma_x + \lambda_y \sigma_y \right) + V_a(x,y)\, \lambda_z \ , \end{aligned} \tag{4.5}$$

where $\sigma_{x,y,z}$, $\tau_{x,y,z}$ and $\lambda_{x,y,z}$ are Pauli matrices for the sublattice, valley and layer pseudo spins, respectively. A topological loop forms from a space dependent function $V_a(x,y)$ that, as sketched in Fig. 4.1a, takes the constant values $+V_a$ ($-V_a$) outside (inside) the loop. In our numerical simulations, we consider a smooth spatial transition with a diffusivity [9] $s = 12.5$ nm to mimic a realistic experiment [50,51]. Details of how we model the closed loops of different shapes are given in the Section. 4.4.1. Finally, the perpendicular field strength B is included in the magnetic length $l_z = \sqrt{\hbar/eB}$.

We numerically look for the eigenstates of the Hamiltonian given by Eq. (4.5) using finite difference discretization of the xy plane in a square grid [75]. The spurious solutions due to fermion doubling [76–78] have been filtered out as in Ref. [9] by coarse graining the wave functions (see App. 7.1) . Our method can handle any symmetry of the loop, in contrast to radial grids which are of smaller dimension and more efficient computationally, but can only describe radially symmetric structures by construction [89]. In all the cases treated below we have checked that good convergence with the grid size is reached.

The Hamiltonian given by Eq. (4.5) fulfills a chiral symmetry given by operator $\mathcal{C} = \sigma_x \tau_x \lambda_y$ relating eigenstates of opposite energies $\mathcal{C}^{-1} H \mathcal{C} = -H$ with $\mathcal{C}^2 = 1$ and $\mathcal{C}^{-1} = \mathcal{C}$. In absence of magnetic field it also fulfills time reversal symmetry $\Theta = i\tau_y \mathcal{K}$, with $\mathcal{K}$ representing complex conjugation, giving $\Theta^{-1} H \Theta = H$ with $\Theta^2 = -1$ and $\Theta^{-1} = -\Theta$. Notice that the presence of valley pseudospin yields $\Theta^2 = -1$, which is similar to the result for time reversal inversion of a spin 1/2 system. Differently to $\mathcal{C}$-symmetry, the result $\Theta^{-1} H \Theta = H$ implies a relation between states of the same energy. That is, if

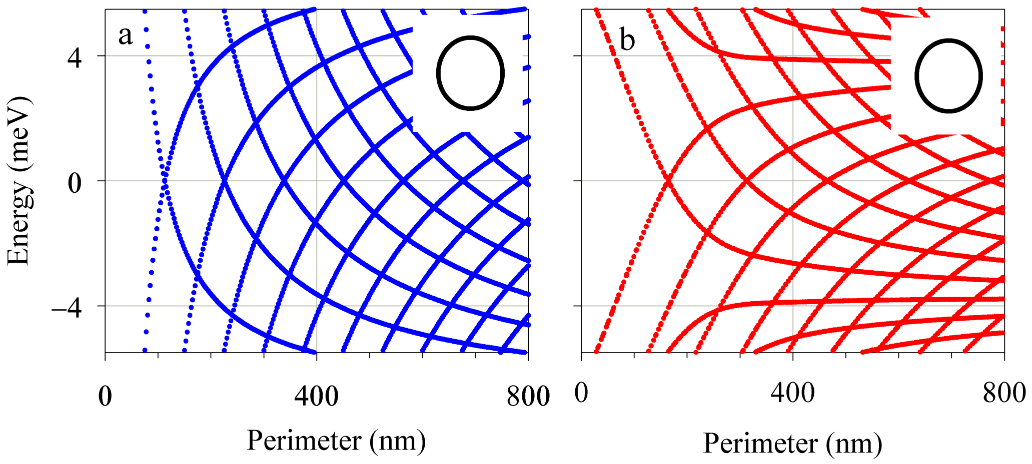

Figure 4.2: QPM (a) and Q2DM (b) energy spectrum for a circle as a function of its perimeter at zero magnetic field. Parameters: wall potential $V_a = 10\,\mathrm{meV}$ and smoothness $s = 12.5\,\mathrm{nm}$.

$|a\rangle$ is an energy eigenstate, then $\Theta|a\rangle$ and $\mathcal{C}|a\rangle$ are energy eigenstates of the same and opposite energies, respectively. We stress that both $\mathcal{C}$ and Θ are valley flip symmetry transformations due to the $\tau_{x,y}$ Pauli matrices.

4.3 Results

Figure 4.2 compares the bound state energies in the analytical (QPM) and numerical (Q2DM) approaches as a function of the loop perimeter when the structure is a circle. Qualitatively, both approaches nicely agree. At zero energy and zero field, Eq. (4.4) from the QPM predicts a sequence of uniformly spaced branch crossings, with spacing given by the zero-energy wavelength

$$\lambda_0 = 2^{3/4}\frac{2\pi\,\hbar v_F}{\sqrt{V_a t}}\ , \tag{4.6}$$

which for $V_a = 10$ meV yields $\lambda_0 \simeq 113$ nm. We then find a qualitatively good correspondence with the zero energy crossings obtained numerically in the Q2DM. Physically, in a ring each branch corresponds to an angular momentum $L_z \equiv xp_y - yp_x$ and, therefore, can produce crossings with additional branches of different angular momenta. For energies departing from zero, the main difference between panels a and b of Fig. 4.2 is that the energy branches are more densely spaced in Q2DM than QPM. This difference can be attributed to the small diffusivity $s = 12.5\,\mathrm{nm}$ used in the QD2M. A smoother 1D kink is known to reduce the spacing of energy branches [9, 55].

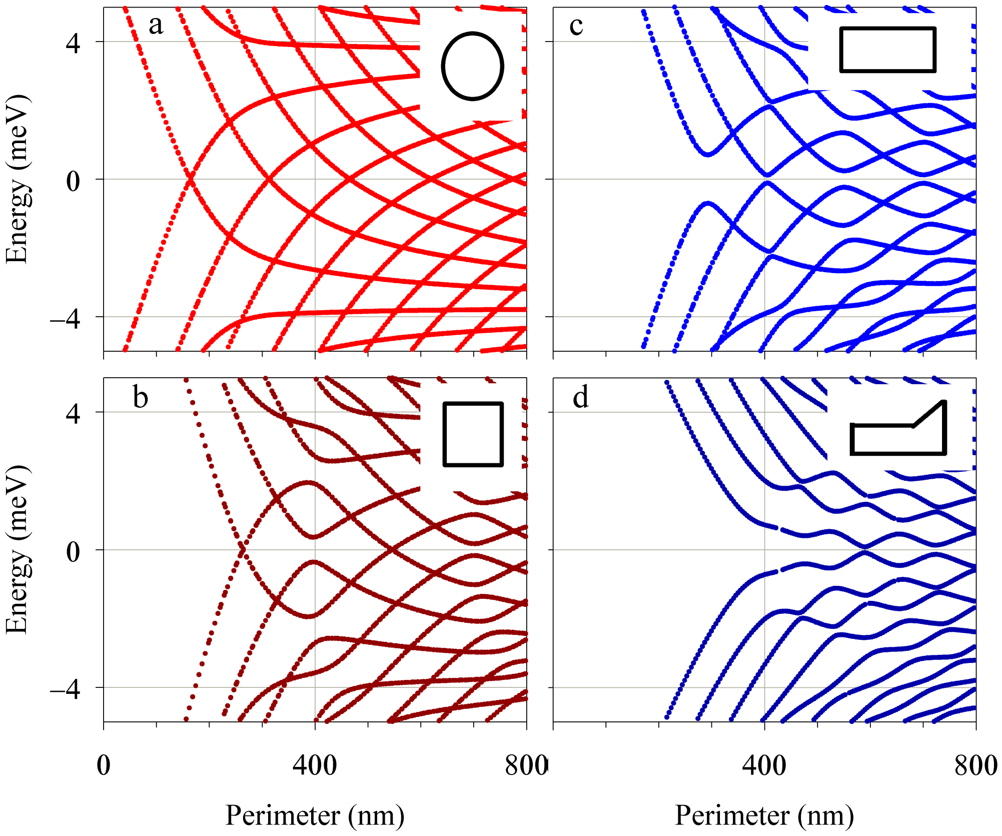

Figure 4.3: Q2DM energy spectra as a function of perimeter for circle (a), square (b), rectangle with aspect ratio $L_y = L_x/2$ (c) and irregular polygon (d). Parameters as in Fig. 4.2.

In Fig. 4.3 we show the Q2DM energy spectra for different loop shapes as a function of their perimeters. Remarkably, the spectrum for noncircular loops show anticrossings of the branches. The square (b) shows an alternation of zero energy crossings and anticrossings as the perimeter increases. Both the rectangle (c) and the irregular polygon (d) show zero energy anticrossings in all cases, although the size of the anticrossing gap is not uniform. There is a general tendency for all shapes to decrease the anticrossing gaps for large perimeter, making the spectra shape independent in this limit.

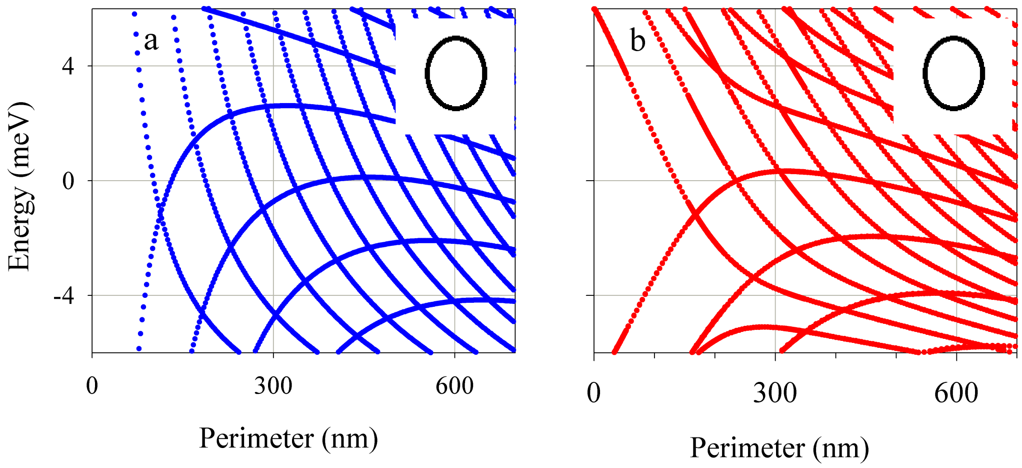

Figure 4.4: Same as Fig. 4.2 with a finite magnetic field. Parameters: wall potential $V_a = 10\,\mathrm{meV}$, smoothness $s = 12.5\,\mathrm{nm}$ and magnetic field $B = 0.5\,\mathrm{T}$.

The fact that, in addition to the circle, only the square shows crossings for some branches can be understood as a symmetry consequence. Inspired by the QPM, the branch crossing is possible in a square when, simultaneously, two conditions are fufilled

$$\left\{ \begin{array}{l} \mathcal{P} = n_1 \lambda_0 \ , \\ e^{ik_0 L_x} = \pm i \Rightarrow \mathcal{P} = (2n_2 + 1)\lambda_0 \ , \end{array} \right. \qquad n_1, n_2 \in \mathbb{N} \ , \tag{4.7}$$

where $k_0 = 2\pi/\lambda_0$ is the mode wavenumber. Only with n_1 odd the crossing is then possible, as indeed obtained in Fig. 4.3b. The second condition in Eq. (4.7) corresponds to the requirement that a translation along the perimeter by the length of a side changes the state in a $\pm i$ phase, which occurs when the total number of wavelengths to distribute in the four square sides is odd $n_1 = 2n_2 + 1$. In a rectangle, one should replace L_x by $L_x + L_y$ in this second condition, which then becomes incompatible with the first one and no crossing is therefore allowed. For the irregular shape (d), the lack of any symmetry is responsible for the absence of crossings in the spectrum. We next discuss the results in the presence of a magnetic field B. Figure 4.4 compares the analytic and numeric results for a circular loop when $B = 0.5$ T. The magnetic field breaks the valley degeneracy of the loop eigenmodes, yielding asymmetric spectra with respect to energy inversion. We remark that Fig. 4.4 shows the results for a given valley. The results for the opposite

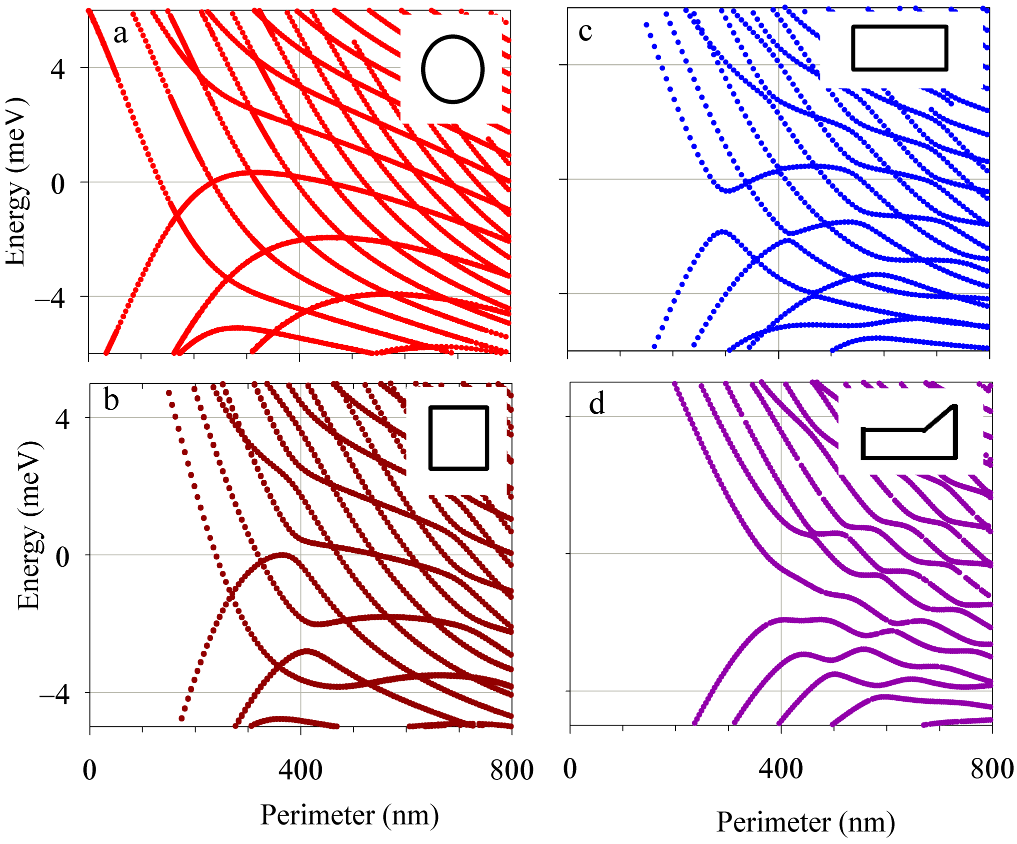

Figure 4.5: Same as Fig. 4.3 with a finite magnetic field $B = 0.5$ T. Parameters as in Fig. 4.4.

valley, shown in Sec. 4.4.1, are shifted in the opposite direction restoring the symmetry of the spectrum for both energy and valley inversion ($\mathcal{C}$ symmetry). There is again a good qualitative agreement between QPM and Q2DM, the most noticeable difference being the denser bunching of the energy branches within Q2DM, as in the $B = 0$ cases discussed above. In Fig. 4.5 we show the results of the 2D model at finite magnetic field for the different shapes. The field-induded asymmetry is similar when the geometrical structure changes. Branch anticrossings are present for nonsymmetic shapes, although they are not centered at zero energy but shifted vertically. Similarly to $B = 0$ (cf. Fig. 4.3), we find that with an increase of the perimeter the shape-dependent features of the spectrum are washed out.

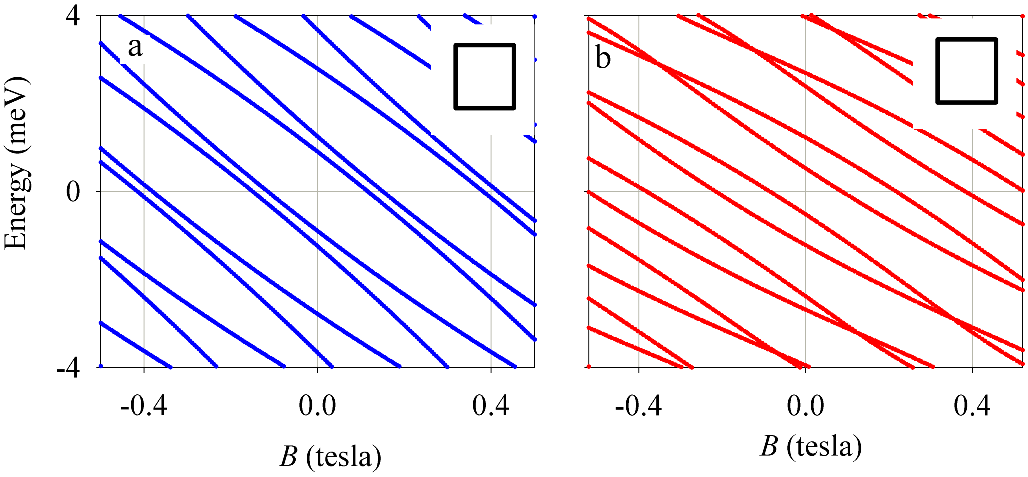

Figure 4.6: Spectrum as a function of magnetic field for a square loop of a fixed perimeter in QPM (a) and Q2DM (b). Parameters: wall potential $V_a = 10\,\mathrm{meV}$, smoothness $s = 12.5\,\mathrm{nm}$ and perimeter $\mathcal{P} = 500\,\mathrm{nm}$.

As a function of magnetic field, for a fixed loop dimension and shape, the loop spectrum shows a periodic behavior that is reminiscent of the Aharonov-Bohm effect. Figure 4.6 shows the result for a square in the QPM and Q2DM, both in good qualitative agreement. The energy branches come in doublets, originating from the two kink branches $f_{1,2}$ given by Eq. (4.1). The results in Fig. 4.6 are in general asymmetric with respect to energy inversion, in the same way as for the results as a function of perimeter (Fig. 4.5); the energy inversion symmetry being fulfilled at $B = 0$ only. For different shapes the results show a similar periodicity, only that the field spacings between branch doublets must be scaled by the enclosed flux Φ.

As with previous figures, the results of Fig. 4.6 are for a single valley; the energy branches for the reversed valley having the exactly opposite slope, as the chiral symmetry dictates. The magnetic field slope of the branches is clearly indicating that the loop sustains persistent currents in finite fields, as discussed already for trivial and topological circular rings in Refs. [70, 90], respectively. Hence, we investigate the shape dependence of the persistent current in topological loops as a possible probe of the geometric effects on topologically confined states. For definiteness, we focus on the current associated to the the persistent current J_1 for the different shapes is shown in Fig. 4.7 for a fixed perimeter of 500 nm. Due to the aforementioned valley and energy inversion symmetry, the persistent current has an odd symmetry with respect to field inversion, implying a vanishing value at zero field.

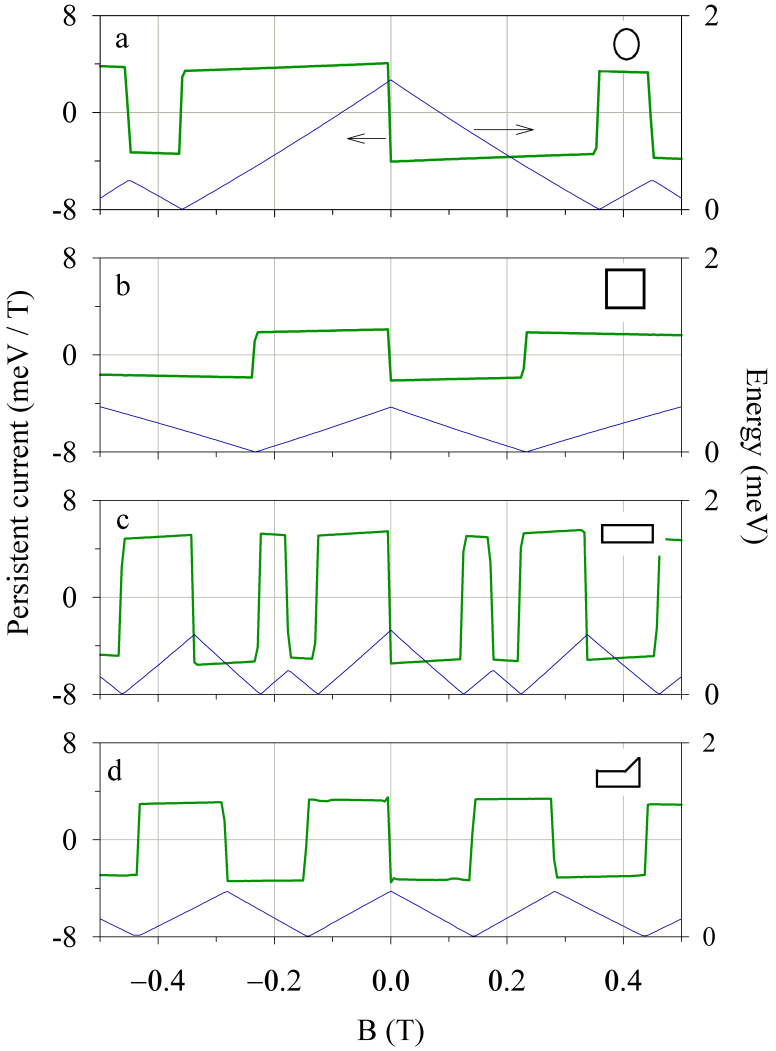

Figure 4.7: Persistent current J_1 (thick line, left scale) and energy E_1 (thin line, right scale) of the lowest positive state as a function of the magnetic field for a fixed perimeter loop and the different shapes indicated in each panel. Parameters as in Fig. 4.6.

lowest positive-energy quasiparticle of the spectrum E_1 from the derivative [91]

$$J_1 = \frac{\partial E_1}{\partial B} \, . \tag{4.8}$$

The current is characterized by a sequence of alternating plateaus of almost constant values. This is an effect of the nearly linear dispersion of the energy levels with magnetic field. Positive and negative plateaus correspond to persistent currents of opposite valleys, circulating with opposed chiralities. For very large perimeters the QPM predicts a B-dependence of the persistent current only through the flux Φ. Therefore, the shape dependence can be scaled by the loop surface. However, in smaller loops the Q2DM yields a nontrivial shape dependence. Along the sequence from high symmetry (a, circle) to low symmetry (b square, c rectangle and d irregular shapes) the behavior looks qualitatively similar, but the plateau lengths are reduced due to the increased number of field transitions. This is also expected since the flux Φ is reduced for the deformed loops. Therefore, measuring the persistent current yields valuable information on the geometrical structure of the loop.

4.4 Discussions

4.4.1 Modeling

The Q2DM low energy Hamiltonian, Eq. (2.1), requires a specific spatial dependence of the asymmetric potential $V_a(x, y)$. This section contains the details of the modeling of different loop shapes with $V_a(x, y)$ smooth profiles parameterized with a diffusivity s. The circle is described by a simple combination of logistic functions in the radial coordinate $r = \sqrt{x^2 + y^2}$,

$$\begin{aligned} V_a^{(cir)}(r) &= V_a^{(in)}\,\mathcal{F}(r; R_0, s) \\ &+ V_a^{(out)}\,(\,1 - \mathcal{F}(r; R_0, s)\,)\ , \end{aligned} \tag{4.9}$$

where $V_a^{(in,out)}$ are the constant values of asymetric potential inside/outside of the loop and the logistic function reads

$$\mathcal{F}(r; R_0, s) = \frac{1}{1 + \exp\left[(r - R_0)/s\right]}\ . \tag{4.10}$$

To describe smooth square and rectangle shapes we first introduce the ranges of the

Cartesian coordinates $x \in [x_a, x_b]$, $y \in [y_a, y_b]$ representing the loop inner area and then use a similar smooth parametrization in each Cartesian direction. Namely,

$$\begin{aligned} V_a^{(squ,rect)}(r) &= V_a^{(in)}\, \mathcal{F}_{2D}(x,y) \\ &+ V_a^{(out)}\, (\, 1 - \mathcal{F}_{2D}(x,y)\,)\ , \end{aligned} \tag{4.11}$$

where

$$\begin{aligned} \mathcal{F}_{2D}(x,y) &= (\, \mathcal{F}(x;x_b,s) - \mathcal{F}(x;x_a,s)\,) \\ &\times\ (\, \mathcal{F}(y;y_b,s) - \mathcal{F}(y;y_a,s)\,)\ . \end{aligned} \tag{4.12}$$

Finally, for the irregular shape we use the same modeling of Eq. (4.11) but with the modification that y_b is no longer constant but the following piecewise function of x

$$y_b(x) = \begin{cases} 0\ , & x < 0\ , \\ x\, y_b/x_b\ , & x > 0\ . \end{cases} \tag{4.13}$$

Notice that we assume centered positions of the loop, with $x_{a,b} = \mp L_x/2$ and $y_{a,b} = \mp L_y/2$. For completeness, the perimeters for the different shapes are $\mathcal{P}_{cir} = 2\pi R_0$, $\mathcal{P}_{squ} = 4L_x$, $\mathcal{P}_{rect} = 2(L_x + L_y)$, $\mathcal{P}_{irr} = \frac{3}{2}(L_x + L_y) + \frac{1}{2}\sqrt{L_x^2 + L_y^2}$.

The QPM analytic model of Sec. 4.2.1 is based on the energies of a sharp straight kink. [8] Therefore, we expect an agreement between QPM and Q2DM in the limit of small values of s. Such comparison is explicitly made in Fig. 4.8 for circles with 6 and 1 nm diffusivities. Panels b and d of Fig 4.8 indeed show the expected agreement for $s = 1$ nm and magnetic fields of 0 and 0.5 teslas. On the other hand, the 6 nm results (Figs. 4.8ac) show increasing deviations towards the low perimeter and large energy directions.

We also stress here that the QPM-Q2DM precise correspondence of Figs. 4.8bd confirms the absence of any Berry-phase deviation from integer n's in the quantization rule given by Eq. (4.4).

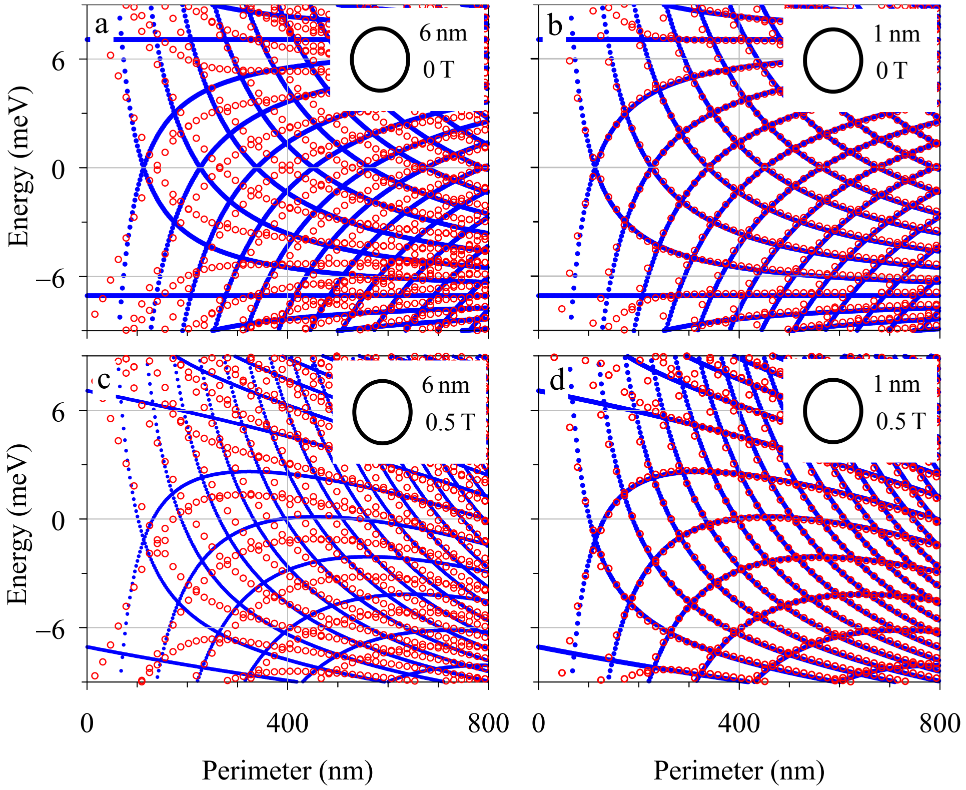

Figure 4.8: Energy eigenvalues of circular loops as a function of perimeter for different diffusivities and magnetic fields as indicated in each panel. Small symbols (blue) and open circles (red) correspond, respectively, to QPM and Q2DM. Notice that the analytic model exactly reproduces the low-energy numerical results only in the limit of sharp potentials (b, d).

4.4.2 Valley reversal

To better illustrate the relation between the different valleys in presence of a magnetic field, Fig. 4.9 shows the opposite-valley results with respect to Fig. 4.4. Due to chiral symmetry $\mathcal{C}$ eigenstates of reversed valleys have exactly sign-reversed energies. As you can see that the spectrum showing a reverse picture in opposite the other valley. The zero-energy crossing is shifted above zero vertically, and the symmetry of the spectrum is broken. This confirms that the magnetic field has the effect to break the valley degeneracy.

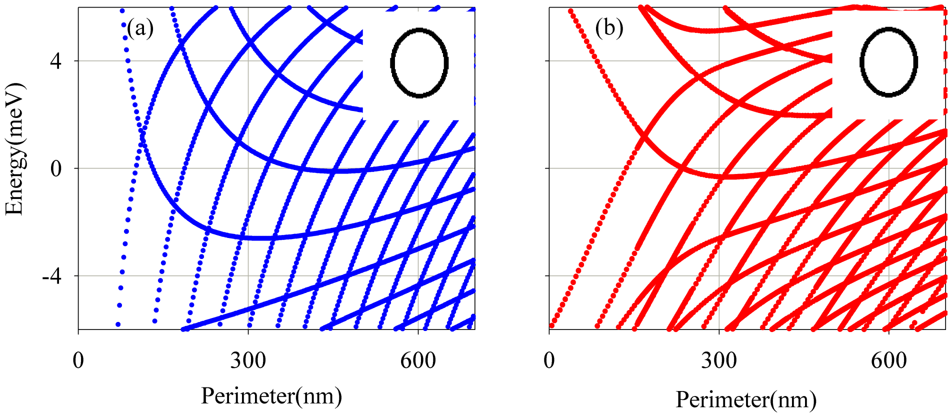

Figure 4.9: Same results of Fig. 4.4 but for the opposite valley.

4.5 Conclusions

We have investigated the confined states in topological loops built in bilayer graphene. We have devised an analytical model, the quantum perimeter model (QPM), based on the infinite straight kink, that provides the wavelength quantization along the loop perimeter. In addition, a full quantum 2D model (Q2DM), valid at low energies, has been numerically solved in order to ascertain the validity of the analytical model. A general good agreement between both models is found. For large sizes, the energy spectra are almost insensitive to the loop shape, as expected from QPM. For small sizes, we have found that Q2DM reflects shape dependence in the emergence of zero-energy crossings for circles, alternating crossings-anticrossings for squares, and only anticrossings for other more irregular structures. The magnetic field introduces energy-inversion asymmetries of the spectrum for a single valley and Aharonov-Bohm periodicities. Shape-dependent anticrossings in small loops are also present with magnetic fields. Finally, we have found that persistent currents are sensitive to shape-dependent features in presence of magnetic fields, which makes electric currents a useful tool to look into bound states in topological systems.

Overall, our results are helpful for tailoring potential structures, finding the optimal geometry for possible applications in quantum computation with topological qubits or for valleytronic devices. Since there could be deviations from the intended symmetry due to fabrication limitations, our study emphasizes the importance of taking into account emerging spatial asymmetries for a careful characterization of the underlying physical system.

Chapter 5

Trivial and topological bound states in bilayer graphene quantum dots and rings

In this chapter, we discuss and compare two different types of confinement in bilayer graphene closed system by top and bottom gating with symmetrical microelectrodes. As discussed in previous chapters, trivial confinement corresponds to the same polarity of all top gates, which is opposed to that of all bottom ones. Topological confinement requires the polarity of part of the top-bottom pairs of gates to be reversed. We show that the main qualitative difference between trivial and topological bound states manifests itself in the magnetic field dependence. We illustrate our findings with an explicit calculation of the energy spectrum for quantum dots and rings. Trivial confinement shows bunching of levels into degenerate Landau bands, with an energy asymmetric gap, while topological confinement shows no field-induced gap and a sequence of state branches always crossing zero-energy.

5.1 Introduction

In this chapter, we will show and discuss fully confined states that could be unambiguously detected by examining their behavior with an external magnetic field, which allows us to distinguish between both (trival and topological) binding mechanisms. Figure 5.1

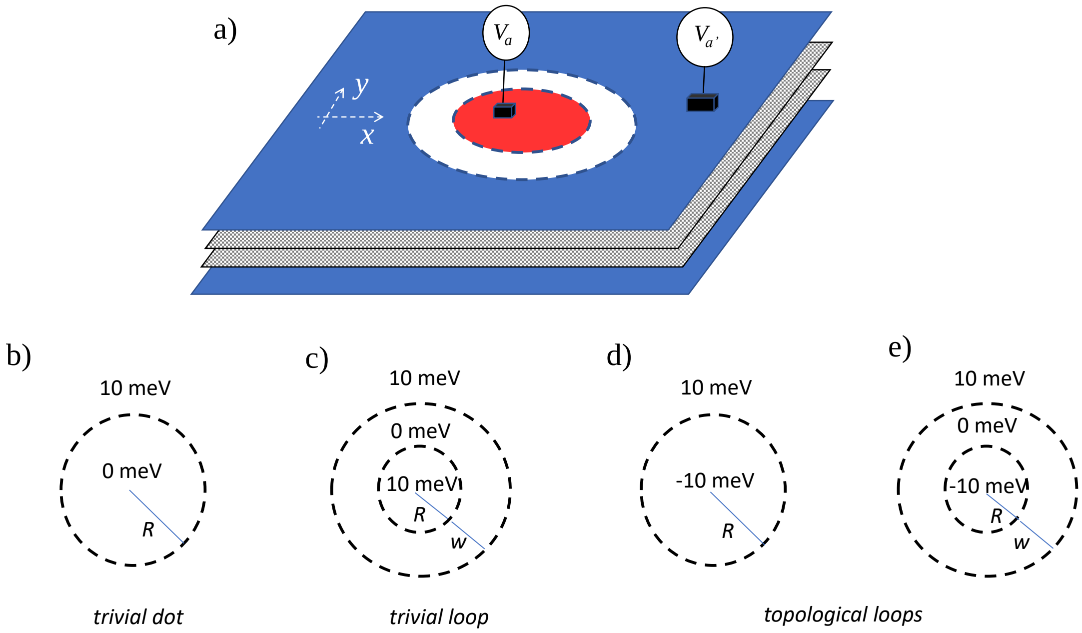

Figure 5.1: a) Generic distribution of top-bottom gate pairs inducing the formation of bound states in BLG. Only the top gates are shown (red and blue), with a similar ditribution of bottom gates hidden under the two graphene layers (gray planes). The potentials V_a, V_a' are reversed in the bottom gates. b)-e) Selected configurations for bound states in BLG nanostructures induced by the indicated gate potentials: trivial dot of radius R (b), trivial ring of radius R and width w (c), and topological rings of radius R with vanishing width (d) and finite width w (e).

shows a sketch of a BLG system with top-bottom gating defining circular nanostructures. The distribution of gates is symmetric, i.e., the same for top and bottom sheets while the applied potentials V_a on the top gates is sign reversed with respect to the bottom gates. This way, a potential difference is created between the two graphene layers sandwiched by a given pair of top-bottom gates. Due to the proximity of both graphene layers, much smaller than the gates separation, the effective interlayer field will be smaller than the inter-gate field, but it may be tuned in a proportional way.

We recall that *trivial confinement* is the case when all gates on a given side, top or bottom, have the same sign. This corresponds to all gate pairs inducing an electric field in the same direction, say upwards, confinement on the plane of BLG being caused by the preference of electrons to attach to the regions of low or vanishing electric field. This is indicated by the white region in Fig. 5.1a, and in the 0 meV region of Fig. 5.1b (trivial dot) and Fig. 5.1c (trivial ring). Calculations of trivial dots and rings can be found, e.g., in Refs. [80, 92].

As discussed in previous chapters, *topological confinement*, on the other hand, requires gates on a given side, top or bottom, to have potentials of different signs. This way, the BLG interlayer field changes direction creating a topological domain wall able to bind electrons as discussed in Sec. 2.1. Figure 5.1c sketches the situation of a topological circular ring. We stress that, differently to the trivial confinement, the topological confinement does not require an extended region of vanishing field; even an abrupt domain wall as in Fig. 5.1c creates bound states. This is already indicating the predominantly 1D character of topological states in BLG, as opposed to the predominantly 2D character of the trivial confinement. As shown below, this results in conspicuous physical differences regarding the spectrum dependence on magnetic field.

We can now present the main findings of this chapter. In the presence of a perpendicular magnetic field, trivial confinement spectra show a bunching of levels indicating the emergence of the 2D physics of Landau levels in BLG. The larger the 2D region of trivial states, the smaller the field at which Landau-level bunching is observed. At zero field there is a finite-size spectrum discretization that evolves as a function of the field into the mentioned level bunching and the formation of a gap for energies in $[0, \sqrt{2}\hbar\omega_c]$, where ω_c is the BLG intrinsic cyclotron energy defined below. Quite differently, topological structures like those in Fig. 5.1d,e do not show the formation of a gap with magnetic field, but a periodic repetition of continuum branches crossing zero energy. Below, we provide quantitative comparisons of the magnetic energy spectra of BLG trivial and topological confinements, emphasizing the differences between both types. These comparisons are based on numerical calculations that use radial grids with small spacings, allowing high precision for circular dots and rings. In some cases we also consider 2D grid calculations, only to confirm the physical scenario for systems departing from circular symmetry.

5.2 Model

We consider a 2D (xy) continuum model for the low-energy excitations of BLG, already used in our previous chapters, and also by many other authors (see Refs. [72, 88] for reviews). The Hamiltonian reads, given here as a reminder of Eq. (4.5),

$$\begin{aligned} H &= v_F \left(p_x - \hbar \frac{y}{2l_z^2} \right) \tau_z \sigma_x + v_F \left(p_y + \hbar \frac{x}{2l_z^2} \right) \sigma_y \\ &+ \frac{t}{2} \left(\lambda_x \sigma_x + \lambda_y \sigma_y \right) + V_a(x,y) \, \lambda_z \end{aligned} \tag{4.5}$$

As usual, $\hbar v_F = 660 \, \mathrm{meV \, nm}$ and $t = 380 \, \mathrm{meV}$ are the Fermi velocity and interlayer coupling, respectively. The sublattice, layer and valley two-fold discrete degrees of freedom of BLG are represented by the $\sigma_{x,y,z}$, $\lambda_{x,y,z}$ and $\tau_{x,y,z}$ sets of Pauli matrices, respectively. The influence of a vertical magnetic field B is included by means of the magnetic length parameter $l_z = \sqrt{\hbar/eB}$, in a symmetric gauge affecting the p_x and p_y operators.

A remarkable property of BLG is that confinement to nanostructures can be achieved with the Hamiltonian of Eq. (4.5) by space modulation of the layer-asymmetry potential $V_a(x,y)$ as we discussed in Sec. 2.1.1. This is a potential imbalance between the two graphene layers that can be tuned by top and bottom gating, as sketched in Fig. 5.1. Physically, the electrons have a preference to stay in regions where this potential imbalance is lower and this can be exploited to confine charges in nanostructures whose shape is controlled by the shape of the gates. A simplest geometry of confinement that has attracted much attention is the circularly symmetric shape, both as quantum dots and rings. Noncircular shapes have been discussed in Ref. [10].

In this chapter we consider a layer-asymmetry potential of circular shape which is different from the one used in Chapter 2 where we discussed the case of bilayer graphene wire. The potential is parameterized as:

$$\begin{aligned} V_a(r) &= V_a^{(in)} \frac{1}{1 + e^{(r-R)/s}} \\ &+ V_a^{(out)} \left(1 - \frac{1}{1 + e^{(r-R-w)/s}} \right) \,, \end{aligned} \tag{5.1}$$

where $V_a^{(in)}$ represents an inner saturation value for $r < R$ and $V_a^{(out)}$ an outer saturation value for $r > R + w$. The potential $V_a(r)$ is vanishing for $r \in [R, R + w]$ and s is a small diffusivity introduced for numerical stability. Appropriately choosing parameters R, w and $V_a^{(in,out)}$ it is possible to model the different types of confinements sketched in Fig. 5.1.

As mentioned in Sec. 5.1, the aim of this chapter is to compare two qualitatively different types of confinement in BLG: trivial confinement corresponding to saturation potentials of the same sign, $\text{sgn}(V_a^{(in)}) = \text{sgn}(V_a^{(out)})$, and topological confinement corresponding to saturation potentials of different signs, $\text{sgn}(V_a^{(in)}) \neq \text{sgn}(V_a^{(out)})$. Our parameterization allows a flexible modelling of trivial dots and rings. It also allows us to describe topological rings of zero or finite widths. Previous works have investigated trivial dots and rings as well as topological rings, but the latter only with $w = 0$ [10]. Here we will also explore the case of a topological ring with a finite w, where potential $V_a(r)$ vanishes and the electrons are essentially free to move.

In presence of a vertical magnetic field, electron states in bulk BLG, with $V_a(r) = 0$, are characterized by the emergence of discrete Landau levels [88]. According to the discussion in Sec. 1.2.3, the Landau levels read :

$$\left\{ \begin{array}{lcl} E_0 & = & 0 \, , \\ E_1 & = & 0 \, , \\ E_{\ell,\pm} & = & \pm\hbar\omega_c\sqrt{\ell(\ell-1)} \, , \quad \ell = 2, 3, 4 \ldots \end{array} \right. \tag{5.2}$$

There exists a two-fold degenerate Landau level at zero energy and a sequence of field-dispersing levels at both positive and negative energies. The cyclotron frequency in Eq. (5.2) is $\omega_c = eB/m_0$, with a mass parameter given by the BLG intrinsic parameters, $m_0 = t/2v_F^2$ (see Sec. 1.2.2). The spectrum of Eq. (5.2) is degenerate for both valleys.

In finite structures like those in Fig. 5.1 we can expect the emergence of Landau levels for high enough fields provided that the system contains a 2D-like region, i.e., a region with $V_a = 0$ where locally electron motion is free and the system resembles bulk BLG. We will show below that, indeed, our calculations indicate Landau level formation in trivial dots (Fig.5.1b), trivial rings (Fig.5.1c) and topological rings of finite width (Fig.5.1e), but not in topological rings of vanishing width (Fig.5.1d). The latter only contain 1D-like loop states, whose energies show B-periodic repetitions of linearly dispersing branches reflecting the Aharonov-Bohm periodicities in the flux piercing the loop.

A practical advantage of the circular symmetry is that we can define subspaces of fixed angular momentum m, performing independent diagonalizations in each m subspace. Notice, first, that valley subspaces are always independent in the Hamiltonian of Eq. (4.5), irrespectively of the spatial circular or noncircular symmetry. We can then assume $\tau_z \equiv 1$, with the reversed valley $\tau_z \equiv -1$ eigenvalues being given by symmetry arguments (see Sec .4.2.2) reversing the energy signs of the $\tau_z \equiv 1$ eigenvalues. In the remaining sublattice and layer subspaces, a 4 component spinor spatial wave function for angular momentum m can be written:

$$\begin{pmatrix} e^{i(m-1)\theta} C_1(r) \\ e^{im\theta} C_2(r) \\ e^{im\theta} C_3(r) \\ e^{i(m+1)\theta} C_4(r) \end{pmatrix} \tag{5.3}$$

with (r, θ) the polar coordinates.

It can be shown that, with the spinor wave function of Eq. (5.3) and Hamiltonian H of Eq. (4.5), one can fully remove the θ-dependencies and diagonalize a purely radial Hamiltonian $H_m(r, p_r)$ for each angular momentum m,

$$\begin{aligned} H_m(r, p_r) &= v_F \, p_r \, \sigma_x \\ &+ \hbar v_F \left(\frac{m}{r} + \frac{r}{2l_z^2} \right) \sigma_y - \hbar v_F \frac{1}{2r} \, \sigma_y \lambda_z \\ &+ \frac{t}{2} (\lambda_x \sigma_x + \lambda_y \sigma_y) + V_a(r) \, \lambda_z \, , \end{aligned} \tag{5.4}$$

with $p_r = -i\hbar \, d/dr$ the radial momentum.

Hamiltonian H_m can be diagonalized for a given layer-asymmetry potential $V_a(r)$ using finite differences in a radial grid and imposing the zero condition at the boundaries. Notice that with $m \neq 0$ there is a $1/r$ divergence at the origin in Eq. (5.4), which is compensated by the behavior of the wave function. Numerically, this is more easily taken into account by including a finite value of R (even if quite small) as in trivial and topological rings. An important aspect to bear in mind in the grid diagonalization of Eq. (5.4) is the possible appearance of spurious solutions due to the known-problem of Fermion doubling for Dirac Hamiltonians (see App. 7.1). We have carefully considered this, filtering out spurious solutions by defining grid-average wave functions and elliminating those solutions whose norm is affected by such grid averaging [9]. As mentioned in Sec. 5.1, we have also performed in some test cases the diagonalization of the Hamiltonian given by Eq. (4.5) without separating in subspaces of angular momentum. However, this is much more demanding computationally and we have only checked the agreement of both methods in a few selected cases.

5.3 Results

Figure 5.2 presents selected results for trivial and topological circular systems as a function of size, in zero magnetic field. A trivial ring (Fig. 5.2a) is characterized by a conspicuous gap in the spectrum around zero energy, due to the energy quantization induced by the finite w. In trivial dots or rings with smaller w this energy gap is much reduced or totally closed for large values of the radius (Fig. 5.2b). In sharp contrast, the topological systems present a qualitatively different behavior (Fig. 5.2cd). Intersecting energy branches of positive and negative slopes, always crossing zero energy are the main characteristic of the topological systems.

In $w = 0$ topological loops (Fig. 5.2d) the pattern of crossings is very regular and, as discussed in Ref. [10], can be explained with a quantization rule for 1D closed orbits, similar to the Bohr-Sommerfeld one. The topological ring of finite width (Fig. 5.2c) presents a remarkable behavior, simultaneously showing the zero energy intersecting branches and also a merging of horizontal branches at energies $\approx \pm 2\,\mathrm{meV}$, clearly reminiscent of the gap in a trivial ring of the same size (Fig. 5.2a).

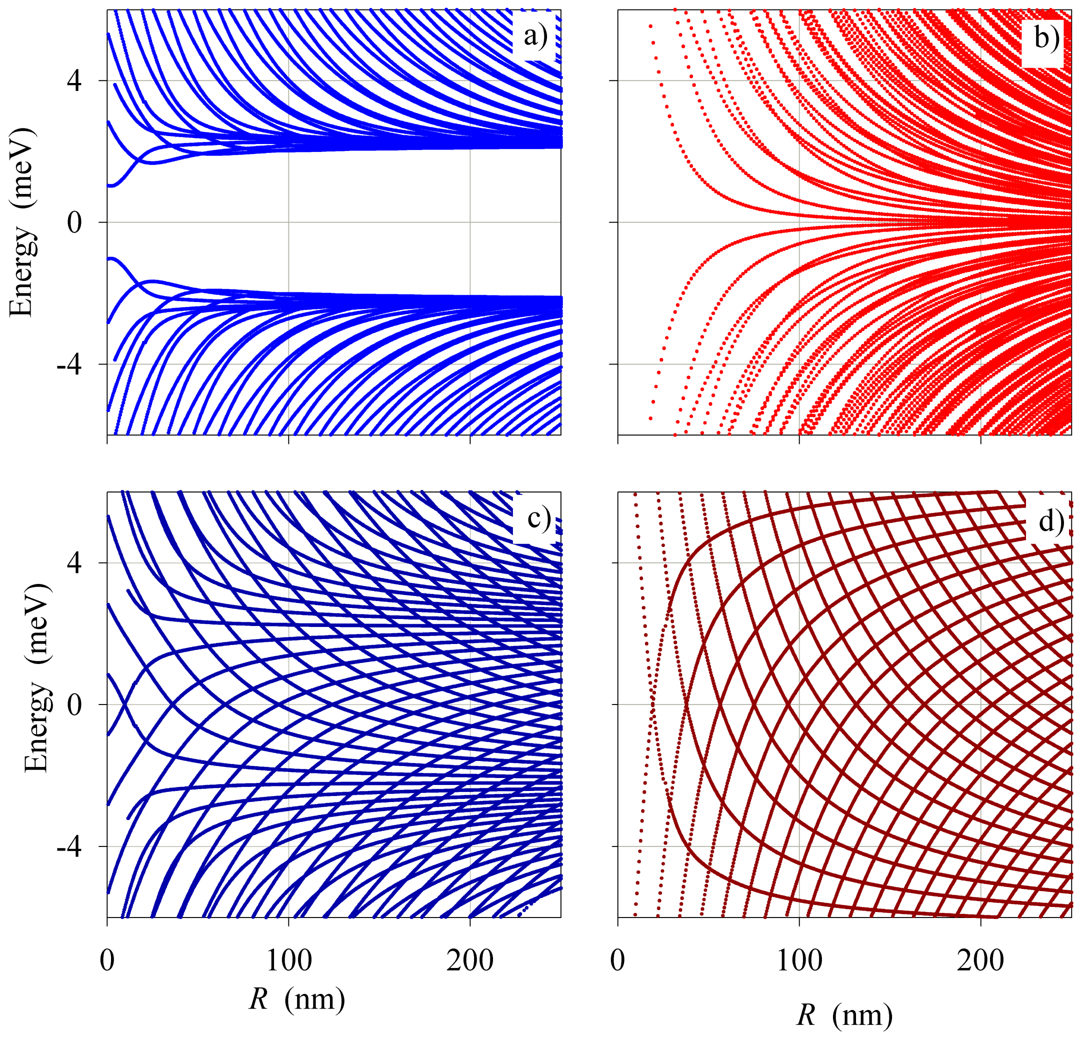

Figure 5.2: Spectrum of eigenvalues with vanishing magnetic field. (a) Trivial ring, $V_a^{(in)} = V_a^{(out)} = 10\,\mathrm{meV}$, $w = 50\,\mathrm{nm}$; (b) trivial dot, $V_a^{(in)} = 0$, $V_a^{(out)} = 10\,\mathrm{meV}$, $w = 0$; (c) topological ring $V_a^{(in)} = -V_a^{(out)} = -10\,\mathrm{meV}$, $w = 50\,\mathrm{nm}$; (d) topological ring $V_a^{(in)} = -V_a^{(out)} = -10\,\mathrm{meV}$, $w = 0$. In all cases we use $s = 2.5\,\mathrm{nm}$.

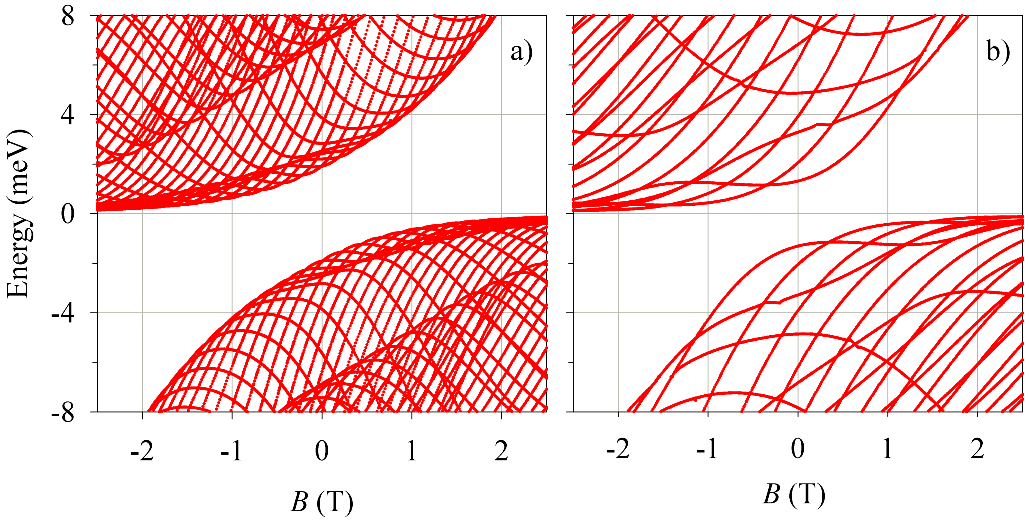

Figure 5.3: Spectra as a function of perpendicular magnetic field of trivial rings (Fig. 5.1c) with (a) $R = 50\,\mathrm{nm}$, $w = 50\,\mathrm{nm}$; (b) $R = 10\,\mathrm{nm}$, $w = 50\,\mathrm{nm}$. Panel (b) is similar to a trivial dot. We use the same $V_a^{(in)}$, $V_a^{(out)}$ and s of Fig. 5.2.

We consider next the role of a perpendicular magnetic field. As discussed above, in systems with regions of 2D electronic motion there is a competition of finite size and B-field discretization into Landau levels; the latter being eventually dominant for large enough fields. Figures 5.3a and 5.3b show the results for trivial rings with a large and a small width w, respectively; the latter resembling a quantum dot. Figure 5.3 is for one valley ($\tau_z = +1$), with the spectrum for the complementary valley ($\tau_z = -1$) being given by reversing the energy signs. The most noticeable feature in Fig. 5.3 is the evolution of the energy gap position. Zero energy is the gap center for $B = 0$ but it evolves into a gap edge at large fields. This is a clear indication of Landau band discretization. For instance, with positive magnetic fields the bulk Landau gap $[0, \sqrt{2}\hbar\omega_c]$ at 1.5 T is $[0, 7.5\,\mathrm{meV}]$, in good qualitative agreement with the results of Fig. 5.3. This figure also shows how for the same value of w the spectrum of a ring with a larger R contains more bands and a cleaner merging into Landau levels at large fields.

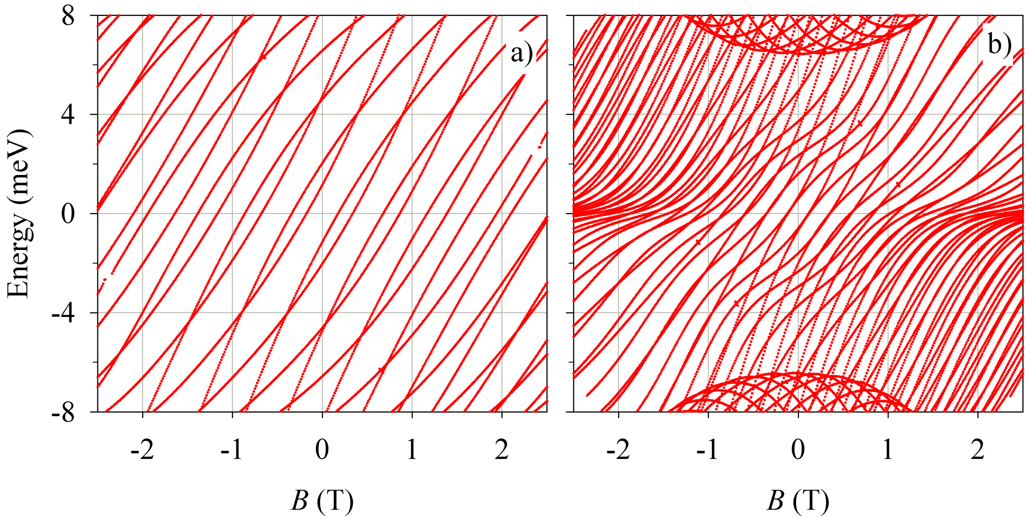

Figure 5.4: Spectra of topological rings (Fig. 5.1d,e) with (a) $R = 50\,\mathrm{nm}$, $w = 0\,\mathrm{nm}$; (b) $R = 50\,\mathrm{nm}$, $w = 50\,\mathrm{nm}$. We use the same $V_a^{(in)}$, $V_a^{(out)}$ and s of Fig. 5.2.

The spectra for topological systems in magnetic field are shown in Fig. 5.4. As anticipated in Sec. 5.1, the topological loop of zero width (Fig. 5.4a) shows no signs of Landau level physics. Instead, its level spectrum is a sequence of almost parallel branches with similar B-slopes. Figure 5.4 is for one valley, the reversed valley having similar branches but with the opposite B-slopes. The case of a topological loop of finite width (Fig. 5.4b) is again most remarkable (as in Fig. 5.2c), showing the mentioned almost parallel branches and, also, signatures of Landau level discretization. The latter is hinted by the level bunching around zero energy for large (positive and negative) fields, as well as by the new branches emerging at large (positive and negative) energies in Fig. 5.4b.

5.4 Discussion and conclusions

We have discussed two types of confinement in BLG nanostructures induced by top and bottom gating. Trivial and topological confinement differ in the potential signs applied to the gates. The regions with zero layer-asymmetry potential correspond to locally free electronic motion.

Confronting Figs. 5.3 and 5.4 we observe the sharp differences in the eigenvalue spectra of trivial and topological systems. The B-increasing gap (for a given valley), with one gap edge pierced at $E = 0$, is a characteristic that permits to intrinsically differentiate trivial and topological states in BLG systems. Landau level physics requires a 2D region of vanishing layer-asymmetry potential, where electron motion is locally free. On the contrary, topological rings of vanishing width behave a purely 1D loops and do not show signatures of Landau level formation. Instead, they display B-periodicities indicating Aharonov-Bohm physics reminiscent of the flux periodicities of rings built with metals or semiconductor 2D electron gases.

At $B = 0$ trivial rings and dots have an energy gap centered around zero energy, larger for the case of rings than for dots. Switching on a magnetic field, this gap evolves into the mentioned non-centered gap of Landau level physics. Quite remarkably, topological rings of finite width manifest both Aharonov-Bohm periodicities and signatures of Landau level discretization in magnetic field.

Our numerical estimates suggest that the magnetic spectrum of both confinement types could detected using today's experimental techniques, which would represent a significant step toward topological quantum computation in graphene systems.

Chapter 6

Conclusion and perspective

In this thesis we investigated the electrostatic confinement and scattering of electrons in BLG nanostructures. We discussed the trivial and topological confinements that can be created by different electrostatic potentials applied to top and bottom microelectrodes acting on the BLG sheets. In our study, we used the effective model of low energy Hamiltonian to investigate the behavior of both types of states.

In the trivial confinement the applied potentials are of a common sign (say positive) for the top microelectrodes and of a common reversed sign (say negative) for the bottom microelectrodes. A voltage difference is created between the BLG layers directly underneath the microelectrodes and this causes an opening of the local gap. The confinement is then induced on those regions with vanishing local gap and a zero potential difference between the two graphene layers. For an electrostatic BLG wire the zero potential region not affected by the microelectrodes is infinite along x and has a width L_y along y. Chapter 2 discussed in detail the wire case, determining its energy spectrum as a function of the momentum along the wire and showing how the gap decreases as the width L_y increases.

When we apply a perpendicular magnetic field to the BLG sheets, the valley degeneracy is broken and the spectrum of energy as a function of the magnetic field shows different levels dispersions depending on the valley index. The results show that the spectrum is characterized by the emergence of discrete Landau levels, with a two-fold degenerate Landau level close to zero energy and a sequence of discrete levels at higher positive and lower negative energies.

The topological confinement in BLG is achieved when the top microelectrodes display sign inversions, with the corresponding exactly opposite inversions in the bottom microelectrodes. As a consequence there are boundaries separating BLG regions with interlayer electric field in opposite directions. As detailed in Sec. 2.2, the behavior of the energy spectrum shows qualitative differences with respect to the trivial confinement. We discussed the topological confinement by a single kink potential and a double kink. Our results for a single kink show topological states in the middle of the gap, with two branches for each valley propagating in opposite directions. For the double kink, there are four branches for each valley. The topological confinement with magnetic field also breaks valley degeneracy of the states, as in the trivial confinement, showing a weak dependence on the field for the single kink and a larger shift of the energy branches for the double kink.

In Chapter 3 we have presented our published paper corresponding to the scattering of the topological kink-antikink states, in which we propose and study a device for controlling the scattering of those states. Transmission manipulation is achieved by means of a kink-antikink constriction that allows the formation of point contacts with anomalous quantized conductance and side loops with chiral quasi-bound states. We calculate the conductance, demonstrating how the obtained conductance curves provide information on the system energy spectrum. We obtain a valley polarization for tiny magnetic field which is tunable with the gate potential.

Chapter 4 describes the geometry dependence in bilayer graphene topological loops. We took into account in the study four shapes: circle, square, rectangle, and irregular polygon. We calculated the energy spectrum for each case and we found that the energy spectrum is shape dependent for the topological loops of small size. For a rectangle and square we obtained characteristic zero energy crossings and anticrossings. The magnetic field introduces energy-inversion asymmetries of the spectrum for a single valley and Aharonov-Bohm periodicities in field intensity. Shape-dependent anticrossings in small loops are also present with magnetic fields. We also calculated the persistent currents and we found that they are sensitive to shape-dependent features in presence of magnetic fields, which makes electric currents a useful tool to look into bound states in topological systems.

In Chapter 5 we investigated and compared the two types of confinement, trivial and topological, for circular dots and rings. We have calculated the energy spectrum for both confinements taking into account four cases: two for trivial confinement (trivial dot and trivial loop) and two for topological confinement (topological ring of zero width and of finite width). We have calculated the energy spectrum and its magnetic field dependence, stressing how for the trivial confinement the spectrum opens a gap around zero energy, with state branches never crossing zero energy. In contrast, the topological confinement shows continuous state branches evolving from negative to positive energies and thus crossing zero energy.

The effective Hamiltonian adequately describes the low energy spectrum, near the BLG Dirac points. It has allowed us for a reliable description of low energy features in the different situations and for the types of confinement mentioned above. Care must be taken, nevertheless, in a correct filtering of spurious states appearing as Fermion doubling artifacts. The formalism also describes orbital magnetic field effects in a four subband model (sublattice and layer) for each valley. In large structures such as in the kink-antikink analysis we found remarkable orbital effects and valley filterings with small fields in the millitesla range. In dots and rings we found field effects such as the emergence of Landau levels in the few tesla range.

As limitations of our approach, we can mention our neglecting of Coulomb interaction (charging energies) in BLG quantum dots, whose importance for the two-electron spectrum with a valley transition at low magnetic field has been discussed in Refs. [93–95]. In large systems, as intended in this thesis, charging effects are small but they are increasingly important as the size is reduced. The spin degree of freedom was also completely neglected, assuming vanishingly small Zeeman splitting and spin-orbit interactions in BLG, in comparison to other effects. A more refined description of smaller energy effects would also require including these spin-related interactions. In particular, it has been shown that spin-orbit interaction alone can create quasi-bound [96] and bound [97] states [98] in, e.g, InAs quantum conductors. It would be interesting to investigate this effect in bilayer graphene nanostructures and its competition with the topological confinement discussed in this thesis. Another interesting avenue of research is the generation of spin-independent currents using wave interference in the presence of ferromagnetic contacts [99, 100].

Finally, we intend to investigate the kink-antikink potential in trilayer graphene, comparing also with the trivial confinement and calculating the conductance in both cases. The energy spectrum of this type of confinement was discussed in Ref. [101]. We also want to work in the future on the spin-orbit coupling in BLG material, where several works have addressed the spin-orbit coupling in the presence of weak or large electric fields [102, 103]. In our case we want to investigate the relevance of spin-orbit interactions with topological kink potentials.

Chapter 7

Appendices

7.1 Appendix A Fermion doubling problem in Dirac-like Hamiltonians

In this thesis, we have used numerical methods for solving the Hamiltonian given by Eq. (2.1). We used the finite difference method which is a method that transforms an abstract equation into an equation that can be solved numerically, with matrix techniques.

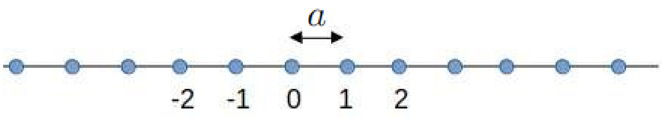

Figure 7.1: A one-dimensional grid where a is the spacing

This method relies on discretizing a function on a grid. The grid is a set of points as represented in Fig. 7.1, in which the wave function is represented by its values on those points.

After the discretization, which yields the first derivative with finite difference formulas, we find first a wrong spectrum represented in Fig. 7.2 in which the number of fermions is doubled (eight branches instead of four branches). This is the infamous fermion doubling

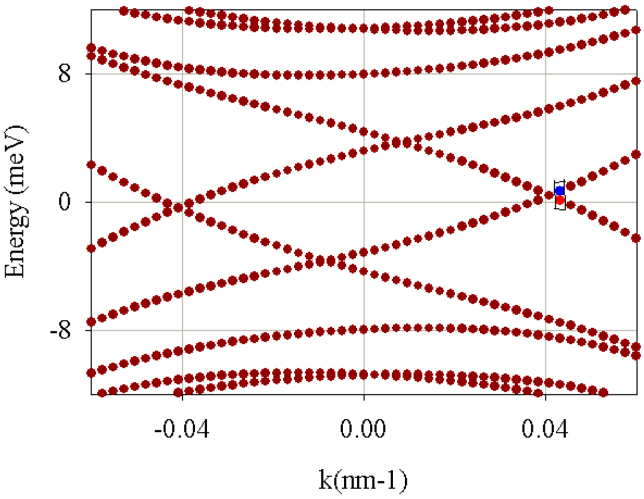

Figure 7.2: Energy band spectrum of bilayer graphene under single kink potential ($V_a = 10$ meV, $B = 0$ T and $s = 12$ nm) for one valley K showing 4 branches at low energy two physically good and two spurious. The two points show the kind of states: Red state represents the spurious state and the blue one represents the good state.

problem [76, 78].

In tight binding, this is equivalent to the approximation in momentum space $k \approx \sin(ka)/a$. In the limit $a \to 0$ they carry infinite momentum. If k is small and a is finite the approximation makes sense and is good. But for $ka = \pi$ the sinus vanishes and implies that $k = \pi/a$ is so a large value for small a spacing that leads to spurious states [76, 78]. To eliminate this problem, there are several methods in the literature such as Wilson's solution, whereby by adding terms to the Hamiltonian we can remove the double states to obtain physically meaningful results [104].

Our proposed method is the filtering of spurious states. This is the method that we used in this thesis. The filtering is done by calculating the average of the right (or left) neighboring point with:

$$\tilde{\Psi}(i) = \frac{\Psi(i) + \Psi(i+1)}{2}. \tag{7.1}$$

- If the norm $\tilde{N} = \sum_{\sigma\lambda} \int |\tilde{\Psi}(y)|^2 dy \approx 1$ then the state is good. This means that is physically good and this is confirmed when we calculate the density of this state. We find

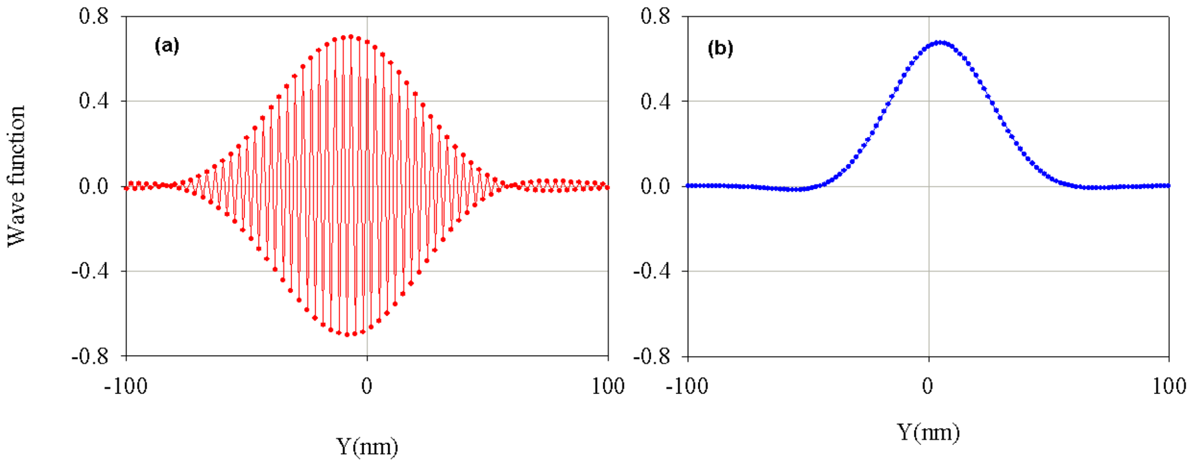

Figure 7.3: a) The wave function plot for a spurious state, b) The wave function plot for a good state (at $k = 0.05$ nm^{-1} and $V_a = 10$ meV).

that the density is smooth, showing the confinement of this state.

- If the norm $\tilde{N} = \sum_{\sigma\lambda} \displaystyle\int |\tilde{\Psi}(y)|^2 dy \approx 0$ then the state is spurious. In this case the density and the wave function of this states shows oscillations, which means that this state is not a physical state.

Figure 7.2 represents the energy spectrum of bilayer graphene under kink potential with a fermion doubling problem. The figure shows four branches for each valley. The extra two branches are due to the fermion doubling problem and are spurious or artifact states. They are not physically good states. seen in Fig. 7.2, the blue points correspond to good states and the red one corresponds to the spurious states.

To better differentiate between them, we have calculated the wave function for the good states (physically good) and the spurious states (artifacts). Fig. 7.3(a) represents the wave function for a spurious state with oscillations is opposite to Fig. 7.3(b), which shows the wave function for the good state confirming the confinement (smooth density). By using the filtering method those spurious states are removed and we get only the physically good ones.

7.2 Appendix B Current calculation

In graphene, we describe the low energy electrons as massless Dirac fermions. We can start our calculation from Eq. (1.10), in where the Schrodinger equation takes the form:

$$i\hbar \, \frac{\psi(\vec{r},t)}{dt} = H\psi(\vec{r},t), \tag{7.2}$$

with $\vec{r} = (x, y)$ and the wave function we can presented as:

$$\psi(\vec{r},t) = \begin{pmatrix} A(\vec{r},t) \\ B(\vec{r},t) \end{pmatrix}. \tag{7.3}$$

We consider a 1D case. The Hamiltonian reads then: $H = -i\hbar \; v_F \; \sigma_x \; \partial/\partial_x$.

Thus, we obtain two coupled equations:

$$\frac{\partial}{\partial t} \begin{pmatrix} A(x) \\ B(x) \end{pmatrix} = -i\hbar v_F \begin{pmatrix} 0 & \frac{\partial}{\partial x} \\ \frac{\partial}{\partial x} & 0 \end{pmatrix} \begin{pmatrix} A(x) \\ B(x) \end{pmatrix}. \tag{7.4}$$

We consider the continuity equation $(\partial/\partial t)\rho = \vec{\nabla}.\vec{J}$, and $(\partial/\partial t)\rho = (\partial/\partial t) \mid \psi \mid^2$ Thus, the probability current density for graphene in x and y directions reads as:

$$J_x = v_F \; \Psi^\dagger \begin{pmatrix} \sigma_x & 0 \\ 0 & \sigma_x \end{pmatrix} \Psi, \tag{7.5}$$

and

The previous calculation can be extended to the y direction:

$$J_y = v_F \; \Psi^\dagger \begin{pmatrix} \sigma_y & 0 \\ 0 & \sigma_y \end{pmatrix} \Psi, \tag{7.6}$$

with v_F the Fermi velocity, Ψ the wave function and $\sigma_{x,y}$ the Pauli matrices.

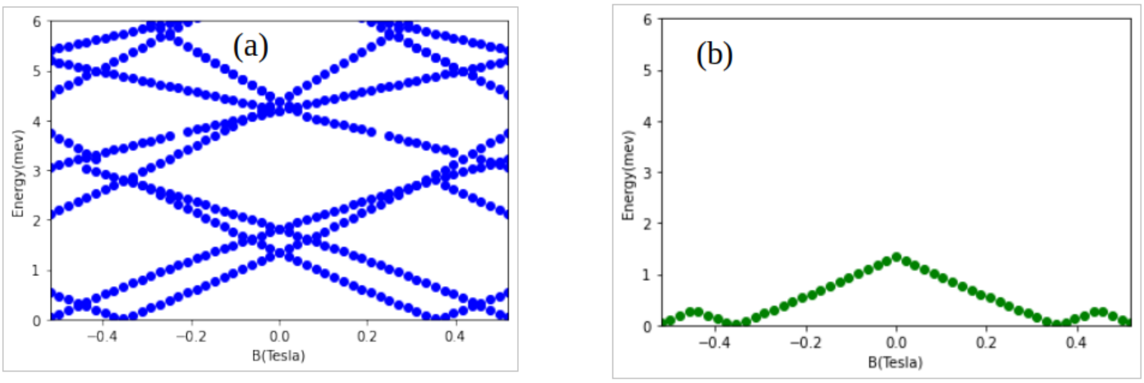

Figure 7.4: (a)Energy spectrum of rings as function of magnetic field for the two valleys K and K'. (b) The minimum positive states. (With $V_a = 10$ meV and $s = 12$ nm

A derivation of Eq. (7.6) is included in Ref. [105] where they calculate the angular current density for a single layer graphene quantum ring.

In our case, the persistent current is calculated for closed loops such as rings, squares, rectangles, or any shape presented in Chap. 3 using the relation as discussed in Ref. [90] and Ref. [106] in where the persistent current in a closed loop shows a periodic behavior as a function of magnetic field using the following formula :

$$J_I = \frac{\partial E}{\partial B} \tag{7.7}$$

where we calculated the derivative from the spectrum of energy as a function of the magnetic field (see Fig. 4.6) and we take the derivative of the minimum of the positive state for both valleys $E > 0$ (see Fig. 7.4).

Bibliography

[1] Lieven, V. & Eriksson, M. Quantum computing with semiconductor spins. *Physics Today* **72**, 38 (2019).

[2] Zajac, D. M. *et al.* Resonantly driven CNOT gate for electron spins. *Science* **359**, 439–442 (2018).

[3] Bednarek, S., Pawłowski, J. & Skubis, A. Manipulation of a single electron spin in a quantum dot without magnetic field. *Applied Physics Letters* **100**, 203103 (2012).

[4] Russ, M. & Burkard, G. Three-electron spin qubits. *Journal of physics, Condensed matter* **29**, 393001 (2017).

[5] Schaibley, J. R. *et al.* Valleytronics in 2D materials. *Nature Reviews Materials* **1**, 16055 (2016).

[6] Rycerz, A. & Tworzydło, J. Valley filter and valley valve in graphene. *Nature Phys.* **3**, 172–175 (2007).

[7] Sui, M. *et al.* Gate-tunable topological valley transport in bilayer graphene. *Nature Physics* **11**, 1027–1031 (2015). URL `https://doi.org/10.1038/nphys3485`.

[8] Martin, I., Blanter, Y. M. & Morpurgo, A. F. Topological confinement in bilayer graphene. *Phys. Rev. Lett.* **100**, 036804 (2008).

[9] Benchtaber, N., Sánchez, D. & Serra, L. Scattering of topological kink-antikink states in bilayer graphene structures. *Phys. Rev. B* **104**, 155303 (2021).

[10] Benchtaber, N., Sánchez, D. & Serra, L. Geometry effects in topologically confined bilayer graphene loops. *New Journal of Physics* **24**, 013001 (2021).

[11] Benchtaber, N., Sánchez, D. & Serra, L. Trivial and topological bound states in bilayer graphene quantum dots and rings. *Physica Status Solidi (b)* 2200023 (2022).

[12] Geim, A. & Novoselov, K. S. The rise of graphene. *Nature Materials* **6**, 183–191 (2007).

[13] Cooper, D. & al. Experimental review of graphene. *International Scholarly Research Notices* **2012**, 56 (2012).

[14] Changgu, L. & al. Measurement of the elastic properties and intrinsic strength of monolayer graphene. *Science* **321**, 385–8 (2008).

[15] Wallace, P. R. & al. The band theory of graphite. *Phys. Rev.* **71**, 622–634 (1947).

[16] Neto, C. & al. The electronic properties of graphene. *Rev. Mod. Phys.* **81**, 109–162 (2009).

[17] Avouris, P. Graphene: Electronic and photonic properties and devices. *Nano Letters* **10**, 4285–4294 (2010).

[18] Slonczewski, J. C. & Weiss, P. R. Band structure of graphite. *Phys. Rev.* **109**, 272–279 (1958).

[19] Semenoff, G. W. Condensed-matter simulation of a three-dimensional anomaly. *Phys. Rev. Lett.* **53**, 2449–2452 (1984).

[20] Haldane, F. D. M. Model for a quantum Hall effect without Landau levels: condensed-matter realization of the "parity anomaly". *Phys. Rev. Lett.* **61**, 2015–2018 (1988).

[21] McCann, E. & Koshino, M. The electronic properties of bilayer graphene. *Reports on Progress in Physics* **76**, 056503 (2013).

[22] Zou, K., Hong, X. & Zhu, J. Effective mass of electrons and holes in bilayer graphene: Electron-hole asymmetry and electron-electron interaction. *Phys. Rev. B* **84**, 085408 (2011).

[23] De Martino, A., Dell'Anna, L. & Egger, R. Magnetic confinement of massless Dirac fermions in graphene. *Phys. Rev. Lett.* **98**, 066802 (2007).

[24] Mireles, F. & Schliemann, J. Energy spectrum and landau levels in bilayer graphene with spin–orbit interaction. *New Journal of Physics* **14**, 093026 (2012).

[25] Datta, S. *Electronic transport in mesoscopic systems* (Cambridge, 1995).

[26] Blanter, Y. & Büttiker, M. Shot noise in mesoscopic conductors. *Physics Reports* **336**, 1–166 (2000).

[27] Reed, M. A. Quantum dots. *Scientific American* **268**, 118–123 (1993).

[28] van Houten, H. & Beenakker, C. Quantum point contacts. *Physics Today* **49**, 22–27 (1996).

[29] van Houten, H. & Beenakker, C. W. J. Quantum point contacts the quantization of ballistic electron transport through a constriction demonstrates that conduction is transmission. (1996).

[30] Beenakker, C. & van Houten, H. Quantum transport in semiconductor nanostructures. *Solid State Physics* 1–228 (1991).

[31] Barlas, Y., Pereg-Barnea, T., Polini, M., Asgari, R. & MacDonald, A. H. Chirality and correlations in graphene. *Phys. Rev. Lett.* **98**, 236601 (2007).

[32] Alomar, M. I. & Sánchez, D. Thermoelectric effects in graphene with local spin-orbit interaction. *Phys. Rev. B* **89**, 115422 (2014).

[33] Kato, T. On the adiabatic theorem of quantum mechanics. *Journal of the Physical Society of Japan* **5**, 435–439 (1950).

[34] Pancharatnam, S. Generalized theory of interference, and its applications. *Proceedings of the Indian Academy of Sciences Section* **44**, 247–262 (1956).

[35] Berry, M. V. Quantal phase factors accompanying adiabatic changes. *Proceedings of Royal society* **392**, 45–57 (1984).

[36] Xiao, D., Chang, M.-C. & Niu, Q. Berry phase effects on electronic properties. *Rev. Mod. Phys.* **82**, 1959–2007 (2010).

[37] Park, C.-H. & Marzari, N. Berry phase and pseudospin winding number in bilayer graphene. *Phys. Rev. B* **84**, 205440 (2011).

[38] Tian, P., Tang, L., Teng, K. & Lau, S. Graphene quantum dots from chemistry to applications. *Materials Today Chemistry* **10**, 221–258 (2018).

[39] Ge, Z. *et al.* Visualization and manipulation of bilayer graphene quantum dots with broken rotational symmetry and nontrivial topology. *Nano Letters* **20**, 8682–8688 (2020).

[40] Banszerus, L. *et al.* Single-electron double quantum dots in bilayer graphene. *Nano Letters* **20**, 2005–2011 (2020).

[41] Eich, M. *et al.* Spin and valley states in gate-defined bilayer graphene quantum dots. *Phys. Rev. X* **8**, 031023 (2018).

[42] Banszerus, L. *et al.* Electron–hole crossover in gate-controlled bilayer graphene quantum dots. *Nano Letters* **20**, 7709–7715 (2020).

[43] Volk, C. *et al.* Electronic excited states in bilayer graphene double quantum dots. *Nano Letters* **11**, 3581–3586 (2011).

[44] Li Jing, W. K. Gate-controlled topological conducting channels in bilayer graphene. *Nature Nanotechnology* **11**, 1060–1065 (2016).

[45] Mania E., T. T. e. a., Cadore A.R. Topological valley transport at the curved boundary of a folded bilayer graphene. *Communications Physics* **2**, 6 (2019).

[46] Yin LJ., Q. J. e. a., Jiang H. Direct imaging of topological edge states at a bilayer graphene domain wall. *Nature communications* **7**, 11760 (2016).

[47] Castro, E. V. & et al, N. Biased bilayer graphene semiconductor with a gap tunable by the electric field effect. *Phys. Rev. Lett.* **99**, 216802 (2007).

[48] McCann, E. Asymmetry gap in the electronic band structure of bilayer graphene. *Phys. Rev. B* **74**, 161403 (2006).

[49] Nemnes, G., Mitran, T., Manolescu, A. & Dragoman, D. Electric and thermoelectric properties of graphene bilayers with extrinsic impurities under applied electric field. *Physica B: Condensed Matter* **561**, 9–15 (2019).

[50] Li, J. *et al.* Gate-controlled topological conducting channels in bilayer graphene. *Nature Nanotechnology* **11**, 1060–1065 (2016).

[51] Chen, H. *et al.* Gate controlled valley polarizer in bilayer graphene. *Nature Communications* **11**, 1202 (2020).

[52] Zarenia, M., Pereira, J. M., Farias, G. A. & Peeters, F. M. Topological confinement in an antisymmetric potential in bilayer graphene in the presence of a magnetic field. *Nanoscale Research Letters Journal* **6**, 452 (2011).

[53] Albuhairan, H. Y., Abdullah, H. M. & Schwingenschlögl, U. Transport and confinement in bilayer chiral borophene. *2D Materials* **9**, 025031 (2022).

[54] Weckbecker, D. *et al.* Low-energy theory for the graphene twist bilayer. *Phys. Rev. B* **93**, 035452 (2016).

[55] Zarenia, M., Pereira, J. M., Farias, G. A. & Peeters, F. M. Chiral states in bilayer graphene: Magnetic field dependence and gap opening. *Phys. Rev. B* **84**, 125451 (2011).

[56] Zhang, Y. *et al.* Direct observation of a widely tunable bandgap in bilayer graphene. *Nature* **459**, 820–823 (2009).

[57] Overweg, H. *et al.* Electrostatically induced quantum point contacts in bilayer graphene. *Nano Letters* **18**, 553–559 (2018).

[58] Overweg, H. *et al.* Topologically nontrivial valley states in bilayer graphene quantum point contacts. *Phys. Rev. Lett.* **121**, 257702 (2018).

[59] Kraft, R. *et al.* Valley subband splitting in bilayer graphene quantum point contacts. *Phys. Rev. Lett.* **121**, 257703 (2018).

[60] Terrés, B. *et al.* Size quantization of dirac fermions in graphene constrictions. *Nature Communications* **7**, 11528 (2016).

[61] Clericò, V. *et al.* Quantum nanoconstrictions fabricated by cryo-etching in encapsulated graphene. *Sci. Rep.* **9**, 13572 (2019).

[62] Kurzmann, A. *et al.* Charge detection in gate-defined bilayer graphene quantum dots. *Nano Letters* **19**, 5216–5221 (2019).

[63] Banszerus, L. *et al.* Electron hole crossover in gate-controlled bilayer graphene quantum dots. *Nano Letters* **20**, 7709–7715 (2020).

[64] Banszerus, L. *et al.* Pulsed-gate spectroscopy of single-electron spin states in bilayer graphene quantum dots. *Phys. Rev. B* **103**, L081404 (2021).

[65] Ju, L. *et al.* Topological valley transport at bilayer graphene domain walls. *Nature* **520**, 650–655 (2015).

[66] Xiao, D., Yao, W. & Niu, Q. Valley-contrasting physics in graphene: Magnetic moment and topological transport. *Phys. Rev. Lett.* **99**, 236809 (2007).

[67] Qiao, Z., Jung, J., Niu, Q. & MacDonald, A. H. Electronic highways in bilayer graphene. *Nano Letters* **11**, 3453–3459 (2011).

[68] Li, J. *et al.* A valley valve and electron beam splitter. *Science* **362**, 1149–1152 (2018).

[69] Cheng, S.-g., Liu, H., Jiang, H., Sun, Q.-F. & Xie, X. C. Manipulation and characterization of the valley-polarized topological kink states in graphene-based interferometers. *Phys. Rev. Lett.* **121**, 156801 (2018).

[70] Xavier, L. J. P., Pereira, J. M., Chaves, A., Farias, G. A. & Peeters, F. M. Topological confinement in graphene bilayer quantum rings. *Applied Physics Letters* **96**, 212108 (2010).

[71] da Costa, D., Zarenia, M., Chaves, A., Farias, G. & Peeters, F. Analytical study of the energy levels in bilayer graphene quantum dots. *Carbon* **78**, 392–400 (2014).

[72] Rozhkov, A., Sboychakov, A., Rakhmanov, A. & Nori, F. Electronic properties of graphene-based bilayer systems. *Physics Reports* **648**, 1–104 (2016).

[73] Serra, L. Majorana modes and complex band structure of quantum wires. *Phys. Rev. B* **87**, 075440 (2013).

[74] Osca, J. & Serra, L. Complex band-structure analysis and topological physics of Majorana nanowires. *Eur. Phys. J. B* **92**, 101 (2019).

[75] Lehoucq, R. B., Sorensen, D. C. & Yang, C. *ARPACK Users Guide: Solution of Large-Scale Eigenvalue Problems with Implicitly Restarted Arnoldi Methods* (Philadelphia: SIAM, 1998).

[76] Susskind, L. Lattice fermions. *Phys. Rev. D* **16**, 3031–3039 (1977).

[77] Nielsen, H. & Ninomiya, M. Absence of neutrinos on a lattice: (i) proof by homotopy theory. *Nuclear Physics B* **185**, 20–40 (1981).

[78] Hernández, A. R. & Lewenkopf, C. H. Finite-difference method for transport of two-dimensional massless Dirac fermions in a ribbon geometry. *Phys. Rev. B* **86**, 155439 (2012).

[79] Park, C. Magnetoelectrically controlled valley filter and valley valve in bilayer graphene. *Phys. Rev. Applied* **11**, 044033 (2019).

[80] Recher, P., Nilsson, J., Burkard, G. & Trauzettel, B. Bound states and magnetic field induced valley splitting in gate-tunable graphene quantum dots. *Phys. Rev. B* **79**, 085407 (2009).

[81] Li, J., Martin, I., Büttiker, M. & Morpurgo, A. F. Topological origin of subgap conductance in insulating bilayer graphene. *Nature Physics.* **7**, 38 (2011).

[82] Pan, H. *et al.* Valley-polarized quantum anomalous Hall effect in silicene. *Phys. Rev. Lett.* **112**, 106802 (2014).

[83] Lu, J. *et al.* Observation of topological valley transport of sound in sonic crystals. *Nature Physics* **13**, 369 (2017).

[84] Gao, F. *et al.* Topologically protected refraction of robust kink states in valley photonic crystals. *Nature Physics* **14**, 140 (2017).

[85] Kane, C. L. & Mele, E. J. Quantum spin Hall effect in graphene. *Phys. Rev. Lett.* **95**, 226801 (2005).

[86] Bernevig, B. A., Hughes, T. L. & Zhang, S.-C. Quantum spin Hall effect and topological phase transition in HgTe quantum wells. *Science* **314**, 1757 (2006).

[87] König, M. *et al.* Quantum spin Hall insulator state in hgte quantum wells. *Science* **318**, 766 (2007).

[88] McCann, E. & Koshino, M. The electronic properties of bilayer graphene. *Reports on Progress in Physics* **76**, 056503 (2013).

[89] Zarenia, M., Pereira, J. M., Peeters, F. M. & Farias, G. A. Electrostatically confined quantum rings in bilayer graphene. *Nano Letters* **9**, 4088–4092 (2009).

[90] Recher, P. *et al.* Aharonov-Bohm effect and broken valley degeneracy in graphene rings. *Phys. Rev. B* **76**, 235404 (2007).

[91] Büttiker, M., Imry, Y. & Landauer, R. Josephson behavior in small normal one-dimensional rings. *Physics Letters A* **96**, 365–367 (1983).

[92] Zarenia, M., Pereira, J. M., Chaves, A., Peeters, F. M. & Farias, G. A. Erratum: Simplified model for the energy levels of quantum rings in single layer and bilayer graphene. *Phys. Rev. B* **82**, 119906 (2010).

[93] Allen, M. T., Martin, J. & Yacoby, A. Gate-defined quantum confinement in suspended bilayer graphene. *Nature Communication* **3**, 934 (2012).

[94] Zarenia, M., Partoens, B., Chakraborty, T. & Peeters, F. M. Electron-electron interactions in bilayer graphene quantum dots. *Phys Rev B* **88**, 245432 (2013).

[95] Lozano, I. *et al.* Thermoelectric transport through interacting quantum dots in graphene. *The European Physical Journal Special Topics* **227**, 1969–1979 (2019).

[96] Sánchez, D. & Serra, L. Fano-Rashba effect in a quantum wire. *Phys. Rev. B* **74**, 153313 (2006).

[97] Crisan, M., Sánchez, D., López, R., Serra, L. & Grosu, I. Localized magnetic states in Rashba dots. *Phys. Rev. B* **79**, 125319 (2009).

[98] Karwacki, Ł., Trocha, P. & Barnaś , J. Spin-dependent thermoelectric properties of a Kondo-correlated quantum dot with rashba spin–orbit coupling. *Journal of Physics: Condensed Matter* **25**, 505305 (2013).

[99] Gelabert, M., Serra, L., Sánchez, D. & López, R. Multichannel effects in Rashba quantum wires. *Phys. Rev. B* **81**, 165317 (2010).

[100] Saiz-Bretín, M., Munárriz, J., Malyshev, A. & Domínguez-Adame, F. Control of spin-polarised currents in graphene nanorings. *Physics Letters A* **379**, 2102–2105 (2015).

[101] de Sena, S. H. R., Pereira, J. M., Peeters, F. M. & Farias, G. A. Topological confinement in trilayer graphene. *Phys. Rev. B* **89**, 035420 (2014).

[102] Konschuh, S., Gmitra, M., Kochan, D. & Fabian, J. Theory of spin-orbit coupling in bilayer graphene. *Phys. Rev. B* **85**, 115423 (2012).

[103] Zhai, X. Layered opposite Rashba spin-orbit coupling in bilayer graphene: Loss of spin chirality, symmetry breaking, and topological transition. *Phys. Rev. B* **105**, 205429 (2022).

[104] Wilson, K. G. Confinement of quarks. *Phys. Rev. D* **10**, 2445–2459 (1974).

[105] Zarenia, M., Pereira, J. M., Chaves, A., Peeters, F. M. & Farias, G. A. Simplified model for the energy levels of quantum rings in single layer and bilayer graphene. *Phys. Rev. B* **81**, 045431 (2010).

[106] Ning, X., Hai, Z., Ming, Q. & Jian, D. Symmetry breaking effect on persistent current in graphene rings. *The European Physical Journal B* **90**, 159 (2017).